



**NANYANG
TECHNOLOGICAL
UNIVERSITY**



Universität für Bodenkultur Wien



REVERSIBLE PLASMONIC BIOSENSORS BASED ON APTAMERS AND HYDROGELS

Submitted by
KHULAN SERGELEN, MSc.

PhD thesis

Submitted in fulfilment of the requirements for the Doctor of Philosophy (PhD)

International Graduate School in Bionanotechnology, IGS BioNanoTech

University of Natural Resources and Life Sciences, BOKU, Vienna

Nanyang Technological University, NTU, Singapore

Austrian Institute of Technology, AIT, Vienna

Supervisor:

Prof. Dr. Wolfgang Knoll, Institute of Biophysics, BOKU

Co-Supervisors:

Prof. Dr. Bo Liedberg, Center for Biomimetic Sensor Science, NTU

Jakub Dostálek, PhD, BioSensor Technologies, AIT

Acknowledgements

I would like to convey my gratitude to Prof. Wolfgang Knoll for allowing me to take part in the PhD program IGS Nanobiotech and giving me the opportunity to carry out my research. Thank you for supervising my work throughout my PhD study, giving helpful comments and being very open with discussions.

Thank you Prof. Bo Liedberg for hosting my stay at NTU, Singapore, where I was warmly welcomed to the group and have received generous supports from everyone. My experience there had been cultivating and I am very fortunate to receive your supervision.

I am greatly indebted to Dr. Jakub Dostálek for his immense support in every step of the way and I have learned a lot from you. You are a wonderful supervisor, who is involved, having always been available for discussions and giving advice.

My sincere appreciation goes to my terrific colleagues at the Biosensors Technologies group at AIT, Dr Nityanand Sharma, Dr Ciril Rozman, Dr Christoph Steininger, Niko Leitner, Stefan Fossati, Daria Kotlarek, Nestor Quillis, Dr Priyamvada Venugopalan and Agnes Reiner.

My colleagues Dr Yi Wang, Dr Xiaohu Liu, Dr Wei Sheng Chai and Dr Chen Peng at CBSS, NTU, Singapore have been very helpful during my stay with navigating myself in the lab and around the campus. Dr. Shahrouz Amini, Dr Maryam Tadayon, Dr Shuhui Hiew and Dr Bram Cantaert, you guys gave me many fond memories of Singapore, we laughed, we sighed, we danced, we played UNO. I was never alone for the long nights of experiments thanks to you.

The support, love and care of my colleagues, amazing friends, my extended family, Imran Khan and Simone Hageneder have been a blessing. I wish you both tight resonance and high profile in your life and career.

Last but not least, it would not have been possible without the unconditional love and support of my whole family. Thank you mom, dad and Onoko for caring and helping me all these years. I am grateful for Martin, my wonderful fiancé, for his patience and understanding and help in proofreading my thesis. My little angel Gubi, you are the most wonderful son a mother could ask for, for waiting patiently while mommy was away or busy.

Khulan Sergelen

August, 2017

Vienna, Austria

Science and everyday life cannot and should not be separated,

Rosalind Franklin

I dedicate this work to my son Gunbilguun,

Хийх бүтээх бүр минь чинийхээ төлөө шүү хонгорхон үр минь,

Abstract

This thesis presents several interlinked projects aimed at sensitive detection of chemical and biological species by the use of surface plasmon resonance-based biosensors. This optical technique takes advantage of electromagnetic field confined at the nanoscale that is generated by the coupling light to the collective oscillation of charge density at the surface of metallic films and metallic nanoparticles. In particular, the thesis utilizes surface plasmon field-enhanced fluorescence spectroscopy (SPFS) and surface plasmon resonance (SPR) biosensors for sensitive readout of heterogeneous assays on gold sensor surface. It focuses on several important aspects that are essential to unlock the potential of optical biosensors in the emerging field of biomedical sciences that require detection of species serving as biomarkers or drugs, in close contact with the human body, outside of specialized laboratories. Specially, it aims at optical biosensor systems that hold potential for continuous monitoring of compounds in complex liquid samples and the following three projects have been pursued.

Firstly, fluorescence assay with weak affinity recognition elements that reversibly bind target analyte has been employed. In order to compensate for low fluorescence signal associated with the affinity binding of target analyte at the sensor surface, the SPFS was implemented. A fluorophore-labeled hairpin aptamer structure was designed for reversible real-time biosensor, which was demonstrated for a model analyte – adenosine triphosphate. The sensing concept relies on resonant fluorescence energy transfer between the fluorophore label and metal that occurs at short distances. The aptamer hairpin is opened and closed by the specific capture of target analyte which is translated to strong variations in fluorescence signal intensity amplified by the intense surface plasmon field. A fully reversible sensor was achieved with up to 23-fold increased fluorescence signal when target analyte was captured. In addition to the aptamer hairpin, split sequences were implemented in a sandwich-type assay for the same analyte. The lack of interaction of the aptamer split sequences in the absence of the analyte allowed for a highly reduced background interference. The sensor demonstrated full reversibility that allowed multiple rounds of detection on the same sensor chip, with time resolution of several minutes for ligands with equilibrium affinity binding constants at around mM concentration.

Secondly, hydrogel materials were employed for the construction of a biointerface that is resistant to fouling from blood serum. It was utilized in the form of thin surface-attached layers and free-standing membranes spanning above gold-coated surface plasmon resonance-based biosensors. The hydrophilic

nature of the used hydrogels provided efficient means to repel the unspecific sorption from serum, as demonstrated by optical waveguide spectroscopy method. In addition, the interaction of biomolecules with the poly-(*N*-isopropyl)acrylamide – based hydrogel used was thoroughly investigated by fluorescence correlation spectroscopy. These materials were tailored for filtering applications as the permeability of hydrogels can be efficiently controlled by tuning the pore size. A thermo-responsive hydrogel was used for dynamic switching of the membrane with about micrometer thickness between its closed and permeable states.

Thirdly, a thin hydrogel layer was employed as an efficient 3D affinity binding matrix that takes advantage of its large surface area. This material was employed in a fluorescence assay that relies on horse-radish peroxidase label and tyramide-based enzymatic fluorescence signal amplification. On 2D surface architectures, self-quenching occurs which limits the performance characteristics of this approach. The use of 3D hydrogel architecture offers means to overcome this limitation and is demonstrated to provide 2 orders of magnitude increase in the fluorescence signal intensity compared to conventional fluorophore-labeled detection scheme.

Zusammenfassung

Die vorliegende Arbeit umfasst mehrere Projekte für den sensitiven Nachweis von chemischen und biologischen Spezies unter Verwendung von Biosensoren basierend auf Oberflächenplasmonenresonanz. Diese optische Technik nutzt die Konzentrierung des elektromagnetischen Feldes auf Nanoebene, welches durch die Kopplung von Licht an die kollektive Oszillation der Ladungsdichte an der Oberfläche von metallischen Filmen und metallischen Nanopartikeln generiert wird. Insbesondere werden Plasmonenfeld-verstärkte Fluoreszenzspektroskopie (SPFS) und Oberflächenplasmonenresonanz (SPR) - Biosensoren für das empfindliche Auslesen von heterogenen Assays auf einer Goldsensoroberfläche genutzt. Die Arbeit konzentriert sich dabei auf mehrere wichtige Aspekte, die als essentiell erachtet werden, um das Potenzial von Biosensoren in dem aufstrebenden Feld der biomedizinischen Wissenschaften zu entfalten. Um dies zu erreichen ist die Detektion von Spezies im Kontakt mit dem menschlichen Körper und außerhalb von spezialisierten Labors erforderlich. Besonders wird dabei auf optische Biosensorsysteme eingegangen, welche das Potenzial für die kontinuierliche Überwachung von Stoffen in komplexen flüssigen Proben haben. Diesbezüglich wurden die drei folgenden Projekte verfolgt:

Im ersten Projekt wurde ein Fluoreszenzassay mit niedrig-affinen Erkennungselementen genutzt, um den Zielanalyten reversibel zu binden. Um das schwache Fluoreszenzsignal der Affinitätsbindung des Zielanalyten an der Sensoroberfläche zu kompensieren, wurde SPFS eingesetzt. Für den reversiblen Echtzeitbiosensor wurde eine Haarnadel („Hairpin“)- Aptamerstruktur, markiert mit einem Fluorophor, designet und mit dem Modellanalyten - Adenosintriphosphat- getestet. Das Sensorkonzept basiert auf einem, auf kurzen Distanzen auftretenden, resonanten Fluoreszenzenergietransfer zwischen der Fluorophormarkierung und dem Metall. Die Aptamerhaarnadel wird durch die spezifische Bindung des Zielanalyten geöffnet und geschlossen, wodurch die Fluoreszenzsignalintensität, verstärkt durch das Oberflächenplasmonenfeld, stark variiert. Ein voll reversibler Sensor wurde entwickelt, welcher ein 23-fach höheres Fluoreszenzsignal aufweist, wenn der Zielanalyt gebunden wird. Für den gleichen Analyten wurden, zusätzlich zu der Aptamerhaarnadelstruktur, auch Splitsequenzen in einem Sandwichassay getestet. Bei Abwesenheit des Analyten tritt keine Interaktion der Splitsequenzen auf, was zu einem stark reduzierten Hintergrundsignal führt. Der Sensor ist voll reversibel und erlaubt multiple Detektionsrunden am selben Chip. Die Zeitauflösung für Liganden mit Affinitätsbindungskonstanten im mM Bereich beträgt wenige Minuten.

Im zweiten Projekt wurden Hydrogelmaterialien zur Entwicklung eines Biointerfaces untersucht, welches resistent gegen das Fouling von Blutserum ist. Dazu wurden dünne oberflächenverankerte Schichten und freistehende Membranen über die goldbeschichteten Oberflächenplasmonenresonanz-Biosensoren gespannt. Optische Wellenleiterspektroskopie zeigt, dass die hydrophile Natur der verwendeten Hydrogele ausreicht, um unspezifische Bindung von Serum zu verhindern. Des Weiteren wurde Fluoreszenzkorrelationsspektroskopie genutzt, um die Interaktion von Biomolekülen mit dem benutztem poly-(N-isopropyl)acrylamid – basiertem Hydrogel zu untersuchen. Diese Materialien wurden eigens für Filteranwendungen optimiert, da die Permeabilität der Hydrogele durch Variation der Porengröße kontrolliert werden kann. Für die dynamische Schaltung zwischen geschlossenen und permeablen Zustand der 1 µm dicken Membran wurde ein wärmeempfindliches Hydrogel verwendet.

Im dritten Projekt wurde eine dünne Hydrogelschicht mit großer Oberfläche als effiziente 3D Affinitätsbindungs-Matrix genutzt. Das verwendete Material wurde in einem, auf Meerrettichperoxidase markierung und Tyramid-basierender enzymatischer Fluoreszenzsignalverstärkung beruhendem Assay verwendet. Während auf 2D Oberflächenarchitekturen Selbstquenching die Performancecharakteristik dieser Methode verschlechtert, bietet der Einsatz von 3D Hydrogelen Möglichkeiten, diese Limitation zu umgehen und eine um 2 Größenordnungen höhere Verstärkung der Fluoreszenzsignalintensität im Vergleich zu konventionellen fluorophormarkierten Detektionsschemata zu erzielen.

Publications

- **Khulan Sergelen**, Christian Petri, Ulrich Jonas and Jakub Dostálek, Free-standing hydrogel membrane with dynamically controlled permeability for lab-on-chip applications, *Biointerphases*, submitted.
- **Khulan Sergelen**, Bo Liedberg, Wolfgang Knoll, and Jakub Dostálek, Surface plasmon field-enhanced fluorescence reversible split aptamer biosensor, *Analyst*, 2017, 142, 2995-3001.
- **Khulan Sergelen**, Stefan Fossati, Aysegül Turupcu, Chris Oostenbrink, Bo Liedberg, Wolfgang Knoll, and Jakub Dostálek, Plasmon field-enhanced fluorescence energy transfer for hairpin aptamer assay readout, *ACS Sensors*, 2017, 2 (7), pp 916–923.
- A. Vagias, **K. Sergelen**, K. Koynov, P. Košovan, J. Dostalek, U. Jonas, W. Knoll, G. Fytas, Diffusion and permeation of labeled IgG in grafted hydrogels, *Macromolecules*, 2017, 50 (12), pp 4770–4779.
- **K. Sergelen**, S. Hageneder, J. Dostalek, Hydrogel optical waveguide fluorescence spectroscopy for efficient readout of enzymatically amplified assays, in preparation.
- J.A.Luna-Coronell, **K.Sergelen**, I.Gyurján, A.Weinhäusel. The immunome of colon cancer: Functional In silico analysis of proteins deduced from IgG microarray profiling, *Genomics, Proteomics and Bioinformatics*, under minor revision.
- Q. Zhang, Y. Wang, A., Mateescu, **K. Sergelen**, A. Kibrom, U. Jonas, T. Wei, J. Dostalek, Biosensor Based on Hydrogel Optical Waveguide Spectroscopy for the Detection of 17 β -Estradiol, *Talanta*, (2013), 104, 149-154.

Contents

1. Introduction	1
1.1. Biosensors	2
1.2. Surface plasmons and surface plasmon resonance	3
1.3. Fluorescence	5
1.4. Surface plasmon field-enhanced fluorescence	7
1.5. SPR biosensor surface architectures	9
1.5.1. Planar gold film	9
1.5.2. Hydrogel binding matrix	11
1.6. SPR-based biosensors	14
1.6.1. Biorecognition elements	14
1.6.2. Assay schemes	17
1.7. State-of-the-art in surface plasmon field-enhanced fluorescence biosensors	18
1.8. State-of-the-art in fluorescence aptamer sensors	22
2. Research aims	26
3. Methods	27
3.1. Spectroscopy instrumentation	27
3.1.1. Surface plasmon resonance and hydrogel optical waveguide spectroscopy	27
3.1.2. Surface plasmon and hydrogel optical waveguide field-enhanced fluorescence spectroscopy	28
3.2. Biosensor preparation	29
3.2.1. Sensor chip preparation	29
3.2.2. Surface functionalization	29
3.2.3. Data analysis	31
4. Plasmon field-enhanced fluorescence energy transfer for hairpin aptamer assay readout	32
5. Surface plasmon field-enhanced fluorescence reversible split aptamer biosensor	48
6. Free-standing hydrogel membrane with dynamically controlled permeability for lab-on-chip applications	60
7. Enzymatic amplification of fluorescence immunoassay in hydrogel binding matrix	90
8. Summary and outlook	102
References	104
List of tables	115
List of figures	116

Abbreviations..... 118

1. Introduction

Since the advent of the scientific era, we humans have discovered and realized many fascinating facts about ourselves. Diseases and ailments are treated, prevented, supply of food is being increasingly met to the current population size, the way of living has become something only fictional books have contained. Yet we have insurmountable room for improvement, where little by little everyone contributes.

In the field of clinical diagnostics, new techniques are being developed to meet the growing demands to accurately diagnose and more efficiently cure diseases [1, 2]. To date, the majority of analytical tools that have been developed allow to sensitively analyze species that serve as biomarkers in specialized laboratories. This approach is not suitable for the detection of concentration changes of biomarkers and drugs in narrow time windows. This particular aspect can be addressed by continuous monitoring devices for detecting biomarkers or drugs that are in close contact with a patient. The only commercial examples of such technology now are the glucose monitoring devices based on electrochemical sensing [3]. This technology utilizes enzymatic reactions specific to glucose which was tailored to operate long-term and eventually provide feedback for appropriate dosing of insulin [4]. In parallel to electrochemical biosensors, also various optical techniques [5] were developed for the detection of medically relevant species [6]. These efforts complement developments in the electrochemical domain and offer the advantage of remote readout that does not require applying electrical power to the device in contact with the sample [7]. For instance, wavelength windows in near infrared part of the spectrum can be harnessed at which the human skin is transparent [8]. In addition, optical affinity biosensors can take advantage of generic recognition elements such as antibodies, peptides, or aptamers which can arguably, specifically bind arbitrary analytes. This thesis addresses several challenges that need to be tackled in order to implement optical sensing techniques for continuous biosensors of chemical compounds such as drugs or biomarkers. It focuses on the utilization of weak affinity ligands that can reversibly bind target analyte at the sensor surface, on amplification of optical signal associated to this binding that is inherently lower than that for commonly used strong affinity binders, and at biosensor surface architectures that are stable long term and resistant to fouling from complex matrices such as blood.

1.1. Biosensors

Biosensors are devices that detect chemical or biological analytes in real-time using biochemical recognition elements through different transduction methods. The definition for electrochemical biosensor according to IUPAC is “a self-contained integrated device, which is capable of providing specific quantitative or semi-quantitative analytical information using a biological recognition element (biochemical receptor) which is retained in direct spatial contact with an electrochemical transduction element” [9]. The main three components of a biosensor [10] are (Figure 1):

- Biochemical recognition element (BRE)
- Signal transducer
- Sample with analytes

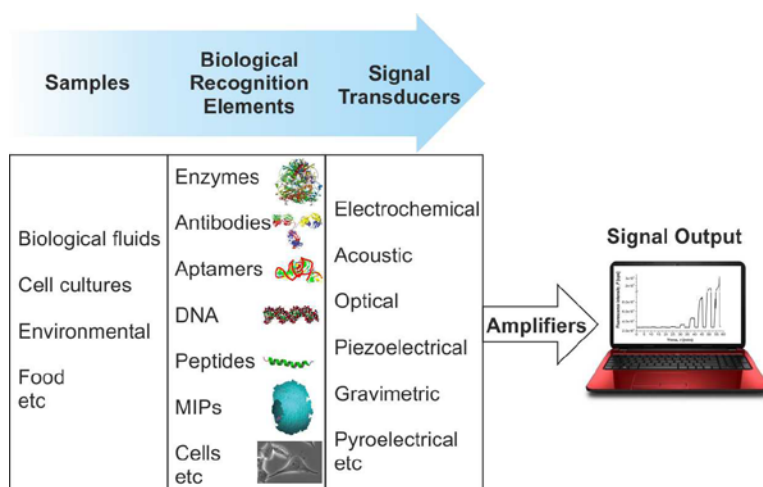


Figure 1. Schematic depiction of biosensor components.

A biochemical recognition element can be enzymes, proteins, antibodies, ribonucleic acid (RNA) or deoxyribonucleic acid (DNA), aptamers, molecularly imprinted polymers (MIPs), peptides, peptide nucleic acid (PNA), tissues or cell [11-14]. Interactions of the target analyte in the studied samples with the BRE are detected and transformed into measurable and quantifiable electrochemical [15], acoustic, optical, piezoelectrical, gravimetric or pyroelectric signals by the transducers [16]. Among the numerous biosensors developed, the most widely reported devices apply optical [17, 18] and electrochemical transducers [19, 20].

The key performance characteristics of biosensors are sensitivity and specificity [21], particularly in applications where analytes in mind have low molecular weight or are present in trace amounts [22, 23].

There is also a need to find strategies to eliminate the matrix effects [24] produced by the different types of samples (cell cultures [25], biological fluids [26], waste water [27] and food [28] etc.) analyzed. Optical biosensors have displayed remarkable performance in meeting the above requirements and holds great potential in further pushing the limits of analytical applications [29-33].

Optical biosensors utilize measurements of optical signal such as fluorescence, absorbance, reflectance, scattering and luminescence, and the most established methods are ellipsometry [34], Raman spectroscopy [35], fluorescence spectroscopy [36], optical waveguide spectroscopy [37, 38] and surface plasmon resonance (SPR) [39-41]. In terms of real-time and label-free monitoring of various analytes at low concentration, the SPR is developed to an extent of commercialization [42-45] and an extensive report of its application in biosensors can be found [26, 46] since the first report [47].

Within the frame of this thesis, the SPR is applied along with surface plasmon field-enhanced fluorescence (SPFS) and the optical waveguide phenomena to improve assays for the detection of molecules.

1.2. Surface plasmons and surface plasmon resonance

Stemming from the report of the existence of surface electromagnetic waves by Zenneck and Sommerfeld in 1907 [48] and the observation of the distribution of light diffraction by Wood in 1902 [49], the term “surface plasmons” (SP) excitation was coined to this phenomenon by Ritchie in 1957 [50]. Surface plasmons are collective charge oscillations at an interface between metal and a dielectric [51]. Depending on the geometry of the metal surface, commonly planar or spherical, results in what are called surface plasmon polaritons (SPP) or localized surface plasmons (LSP), respectively. Propagating waves in free space can have a p-polarized or transverse magnetic (TM) and s-polarized or transverse electric (TE) polarizations [52]. The dispersion relation (energy-momentum relation) of SPPs is expressed as:

$$k_{SP} = \frac{\omega}{c} \cdot \frac{n_m^2 n_d^2}{\sqrt{n_m^2 + n_d^2}}. \quad \text{Eq. 1}$$

The n_m and n_d represent the complex refractive indices of metal and dielectric, respectively, ω/c is the propagation constant of light in vacuum (where ω is the angular frequency, c is the speed of light in vacuum) and k_{SP} is the SPP wave vector or wave number. The SPPs propagate along the metal/dielectric interface with a field intensity exponentially decaying in the direction normal to the surface, with a characteristic depth of about 100 nm which makes SPR an ideal technique for surface studies.

The SPPs can be excited by phase matching using prism or grating structures to couple an incident light beam. SPPs will not be directly excited by incident light from free space as seen in Figure 2. **Left dashed line**, however, through the attenuated total internal reflection (ATR) of the light beam inside a high refractive index (RI) prism results in coupling at the metal/dielectric interface. Hence SPPs are excited (Figure 2. **Left. straight line**) where the dispersion curves intersect due to the increased momentum from prism coupling by ATR. From the two main prism geometries, Kretschmann [53] and Otto [54], the former is more widely applied due to its practicality. The Kretschmann configuration involves a thin film of metal on a glass prism, through which a laser beam at an incident angle θ higher than critical angle θ_c is coupled by ATR. The reflected beam at the prism base directly excites the SPPs at the outer metal/dielectric interface (Figure 2. **Center.**) as a result of the evanescent field penetrating through the thin metal film (~ 50 nm). Contrary to the Kretschmann configuration, in the Otto configuration the dielectric separates the prism and metal interface and an excitation of SPPs occur at dielectric/metal interface (Figure 2. **Right**). In the Otto configuration, the dielectric layer thickness is limited to around 200 nm and bringing the prism at such distances from the metal is difficult and unpractical to achieve.

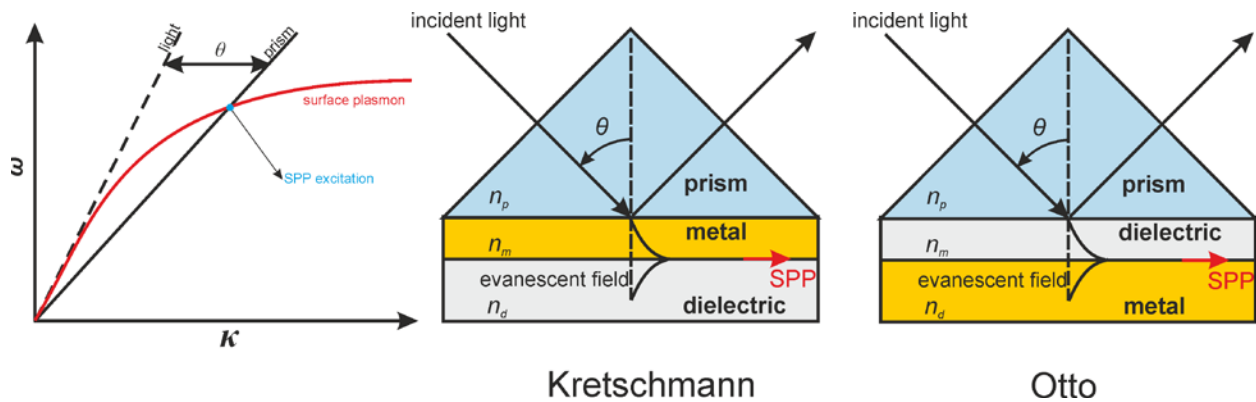


Figure 2. Left. Dispersion relation of SPP in the Kretschmann configuration. Center. The Kretschmann and Right. Otto configurations of prism coupling to SPP. Figure adapted from [55]

SPPs can also be excited through grating coupling of a light beam. Here, a metal surface with corrugations with the appropriate periodicity and depth that allows phase matching is exploited [56]. Since this architecture was not applied in this thesis, it will not be further detailed.

The occurrence of SPP excitation in the Kretschmann configuration of prism coupling is conveniently measured by the reflected light intensity. As the refractive index of the medium increases, the momentum of the SPPs increases and a higher angle of incidence is required for the SPP excitation. By monitoring the intensity of the reflected light as a function of light incidence angle θ , a reflectivity curve is established, see Figure 3. Deposition of additional layers (for example biomolecules) onto the metal surface leads to

changes in the refractive index and it is accompanied by a shift in the resonant angle of the reflectivity curve. The critical angle θ_c is not affected by changes occurring at the surface, only the overall refractive index of the dielectric medium n_d . The molecular binding-induced shift in reflectivity resonant angle is used to derive information about the thickness of adlayer formed at the surface of the metal film, like self-assembled monolayers, molecular adsorption etc. Additionally, by fixing the incidence angle θ , the reflectivity variations can be monitored as a function of time t where kinetic information about the molecular interaction with the surface can be deduced [55]. This is the principle of SPR based biosensors and will be detailed later in the methods sections.

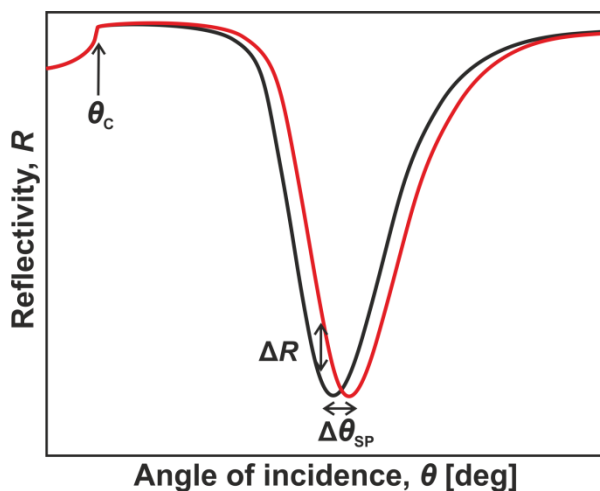


Figure 3. Angular reflectivity spectra and resulting shift in the SPR angle due to refractive index n_d increase at the surface.

1.3. Fluorescence

Fluorescence is the phenomenon of photon emission by a molecule (fluorophore) as result of excitation by light. When photon at a specific wavelength λ is absorbed by a fluorophore at its ground state S_0 , the orbital electron of the molecule is excited to a high singlet state with higher energy. The transition to the excited state occurs within $\sim 10^{-15}$ s. After the excitation, a rapid relaxation to the singlet state S_1 occurs, which is an event termed as the internal conversion and it takes place within $\sim 10^{-12}$ s. When the molecule relaxes and returns from the excited S_1 state to the ground state S_0 , which occurs within $\sim 10^{-8}$ s, fluorescence occurs as emitted photon. These transitions can be described by the Jablonski diagram presented in Figure 4. **Bottom.** Because of this multiple vibrational energy levels and the vibrational relaxation to the lowest vibrational level of the excited state occurring before emission takes place, along with emission occurring through the return to the higher vibrational levels of the ground state, one sees

that the emission spectrum is a mirror image of the absorption spectrum with lower intensity. From the Jablonski diagram one can observe that energy is lost as non-radiative decay for emission and this results in emission of light at a longer wavelength and respectively lower energy than the absorbed light, as manifested by the shift in the wavelength of the emission peak and absorption peak in the spectrum.

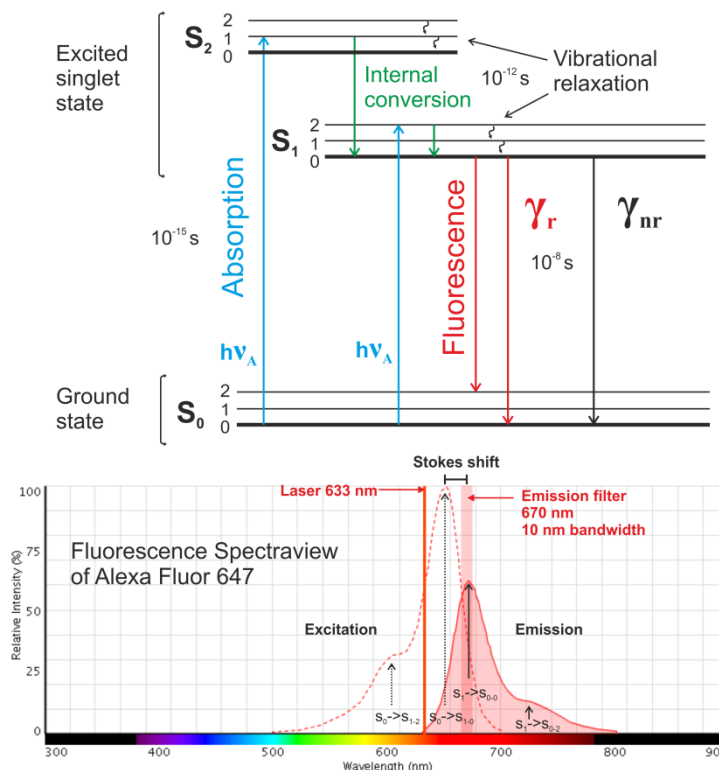


Figure 4. Top. Jablonski diagram that depicts the fluorophore electronic and excitation states. Bottom. Alexa Fluor 647 excitation and emission spectra. Image adapted from [57] and [58]

This effect is called the Stokes shift [59] and is highly dependent on the environment and the type of fluorophore. Due to additional non-radiative pathways k_{nr} that compete with the radiative decay k_r , the quantum yield Q or the ratio between absorbed photons and emitted photons is defined as below, which is lower than unity:

$$Q = \frac{k_r}{k_r + k_{nr}}. \quad \text{Eq. 2}$$

where, k_r is the radiative decay rate and k_{nr} is the non-radiative decay rate. The average time the fluorophore spends in the excited state before returning to the ground state is called the fluorescence lifetime, is expressed as $\tau = \frac{1}{k_r + k_{nr}}$ and typically ranges in the sub to hundreds of ns.

The emitted fluorescence intensity of a fluorophore can be hampered or quenched by certain conditions contributing to k_{nr} . Most prominently a molecule termed the quencher, when in close proximity (less than

2Å) to the fluorophore, can through a wide range of mechanisms, like collision, ground state or excited state complex formation and energy transfer, delay or cancel the emission of photons by the fluorophore [57]. The current thesis focuses on energy transfer related fluorescence quenching and will give details of resonance energy transfer (RET) mechanism in the following sections.

1.4. Surface plasmon field-enhanced fluorescence

Surface plasmons have several properties attractive for sensor applications. Specifically for the enhancement of fluorescence, the enhancement of the electric field intensity occurring at the metal surface is key [60]. A high enhancement of the field intensity is observed around the θ_{SPR} as was reported by Benner et al in 1979 [61]. The intensity of the SPPs decreases exponentially from the metal surface, with a characteristic decay length $L_{SP}/2$, which is around 100 nm (Figure 5).

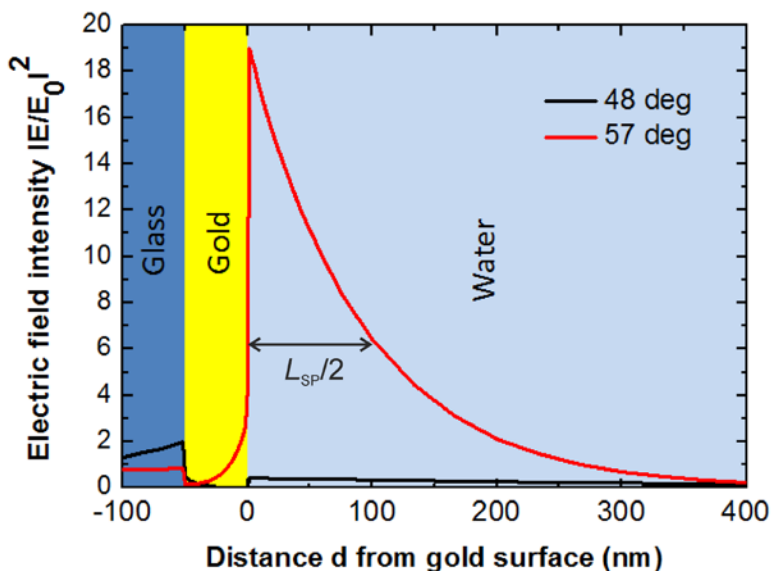


Figure 5. Distance dependent electric field intensity distribution on thin gold film (50 nm) in the direction normal to the surface into a water dielectric at critical angle ($\theta=48$ deg) and resonant angle ($\theta=57$ deg). Calculated for Kretschmann configuration at $\lambda=633$ nm with optical constants taken from literature [62]. Image adapted from [63]

This evanescent field at the metal interface can enhance fluorescence intensity from fluorophores placed in its proximity through the interplay of three effects: 1) the excitation rate of the fluorophore is enhanced [64], 2) the quantum yield is changed to favor radiative decay [65] and 3) the isotropic emission is altered and preferably directed to a certain angle [66]. By combining the SPR optical setup with simultaneous measurement of the emitted fluorescence light intensity from the metal surface side, the surface plasmon

field-enhanced fluorescence spectroscopy (SPFS) is possible and exploited for highly sensitive biosensors. Attridge et al [67] have reported the first application for immunoassay in 1991 and later Liebermann and Knoll [68] re-introduced this method. Angular measurement of the fluorescence intensity F (Figure 6) shows a peak of fluorescence intensity near the resonance angle θ_{SPR} . The peak angle of fluorescence is typically used for the time resolved measurements to monitor the assay kinetics. Additionally, SPFS discriminates fluorescence occurring in the bulk medium from the surface bound fluorophores, that allows for reduction in signal-to-noise ratio as compared to solution based homogenous fluorescence sensors [58].

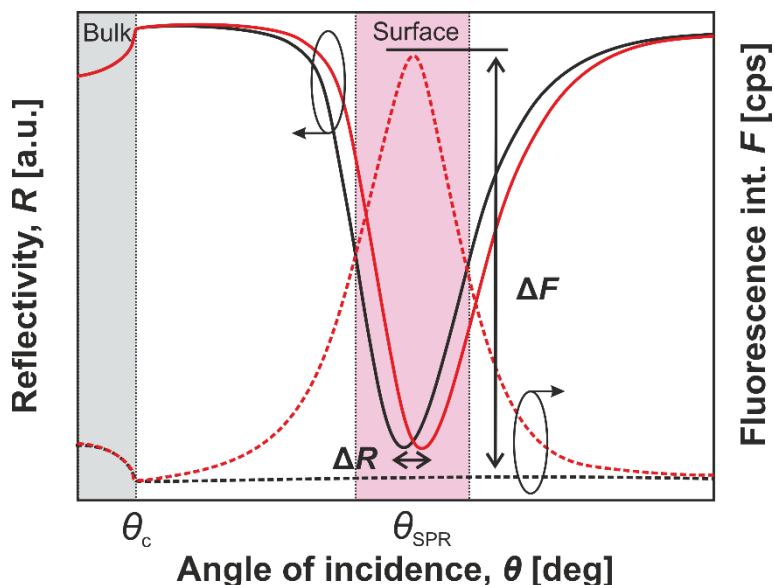


Figure 6. An angular reflectivity and fluorescence spectrum of SPFS measurement showing the reflectivity and fluorescence intensity changes around the critical angle (bulk) and resonance angle (surface).

An important factor to take into consideration is the dependence of fluorescence intensity on the distance to the metal, since fluorophore located in very close proximity are quenched [69]. It is caused by the process of fluorescence resonance energy transfer (FRET), where the fluorophore in the excited state acts as a donor and the metal as an acceptor. This process is highly distance dependent as seen from the energy transfer rate expressed as $k_{\text{nr}}(r) = \frac{1}{\tau_D} \left(\frac{R_0}{r}\right)^6$, where τ_D is the donor decay rate, R_0 is the Förster distance, and r is the distance between donor and acceptor [70]. The distance dependency is used as a ruler in biomolecular interaction studies and it will be elaborated in chapter 4.

1.5. SPR biosensor surface architectures

1.5.1. Planar gold film

The sensor chip commonly used for SPR sensing is composed of a planar thin gold film deposited onto a glass substrate. Gold is mainly used for surface plasmon excitation, as unlike the other metals like silver, aluminum, copper and indium that exhibit SPR as well, it is more chemically inert, has a narrow resonance dip and numerous procedures for chemical modifications have been developed. The thickness of gold for the ATR-based excitation in Kretschmann geometry should typically be around 50 nm thick for sensor applications. An example of the dependence of field intensity enhancement on the metal thickness is shown in Figure 7 [71].

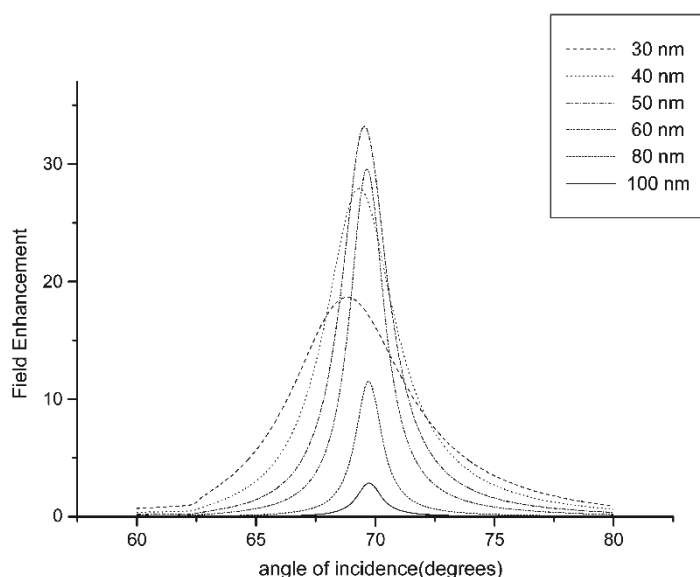


Figure 7. Angular field intensity enhancement spectra for different thicknesses of gold thin layer. The dielectric is water ($n= 1.33$) and incident light has $\lambda= 700\text{nm}$. Image from [71]

The glass substrates are coated with a very thin (1-2 nm) adhesion promoting layer, most commonly chromium, and the gold layer by thermal evaporation or sputtering technique. To attach the biorecognition elements (BREs) onto the gold surface, many different anchoring chemistries are used, from which the most prominent are those utilizing the strong and stable interaction of organosulfur (sulfur, disulfide, thioethers) groups with Au. These sulfur groups are conjugated to a variety of spacer chains (alkyl) with other functional moieties on the other end for the immobilization of biological recognition elements. The sulfur group and the spacer (van der Waals interaction ~ 1.5 Kcal/mol CH_2 group) usually aid the formation of a robust self-assembled monolayer (SAM) onto the Au film with a total

that of adsorption of ~ 45 Kcal/mol. They also should be inert towards the different proteins and other molecular species present in many complex samples analyzed in biosensors, for which alkyl chains with multiple polyethylene glycol (PEG) as terminal groups are famously applied. Ideally, the inert spacer should be hydrophilic and neutral in charge. Thickness of this layer mainly ranges from 2 to 10 nm and chains form a well-ordered SAM. The density of SAMs is around 10^{13} - 10^{14} molecules/cm² given ≈ 20 - 30 Å²/molecule and most commonly applied content of inert carpet layer [72] and immobilization of specific functional groups in the SAM mixtures is usually 4:1 or 9:1 molar ratio [73]. For the immobilization of biomolecules serving as BREs, chemistries targeted at the protein reactive groups like amine, carboxyl and sulfurs are exploited [74]. Similar approaches are also applied for peptides, oligonucleotides and other biomolecules chosen as the BRE. The commonly used BRE immobilization chemistries [74] are summarized in Table 1. The general concept of sensor chip functionalization SAM is illustrated in Figure 8. Importantly, the coupling technique should be optimized for each type of biomolecule that is immobilized to achieve sufficient coverage, retain the vital recognition properties and be accessible for the analyte binding. The linker and the spacer chain however should be stable and fully cover the sensor chip to prevent non-specific adsorption (fouling). Since alkanethiols on Au surface are tilted by 30 deg (see Figure 8), the area per molecule increases with the chain length. When PEGylated SAMs are exposed to aqueous media, the assembly changes from an *all-trans* to helical conformation, which provides water accessibility and stability by forming hydrogen bridges, further enhancing protein resistance through water hydration. Water hydration layer formed at the PEG SAM films is the sole mechanism of the anti-fouling, which improves with increasing layer thickness [72].

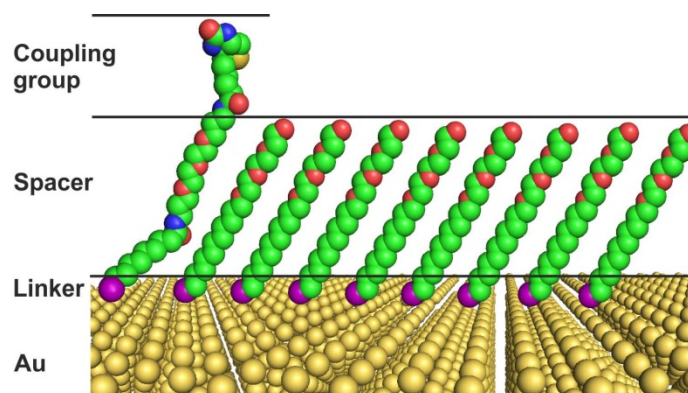


Figure 8. Idealized depiction of a mixed self-assembled monolayer (SAM) formed at a gold surface with functional coupling group for BRE immobilization and inert spacers for surface passivation.

<i>BRE immobilization techniques</i>	<i>Principle</i>	<i>Comment</i>
<i>Non-covalent</i>	Adsorption to metal without underlying linker	High loss of binding Low stability
<i>Covalent</i>	Amine coupling through reactive esters -carboxyl- groups on the sensor surface is activated to esters, by carbodiimides like EDC (1-Ethyl-3-(3-dimethylaminopropyl)carbodiimide), that readily reacts with primary amines and other nucleophiles. The short-lived intermediate <i>O</i> -acylisourea is stabilized through <i>N</i> -hydroxysuccinimide.	Coupling orientation not well defined N-terminal amines of proteins as a source of primary amines, through careful manipulation of pH to suit the <i>pI</i> of other amines in lysines. Carboxylate- and amine- containing buffers reduce reaction efficiency.
	Amine coupling through reductive amination -carbonyl groups on the sensor surface is reduced by sodium cyanoborohydride to form Schiff base with amine groups.	Reaction takes a long time Ideal for polysaccharide surfaces
	Disulfide exchange between reduced sulfhydryl and active disulfide	Orientation of immobilization defined Reversible by reduction
	Sulfhydryl coupling to maleimide through alkylation Maleimide has pH specific reaction to sulfhydryl and amines	Orientation of immobilization defined Irreversible Bifunctional organosulfur on gold surface difficult to prepare
	Hydrazines on the sensor surface couples to the aldehyde groups of the carbohydrate via sodium periodate oxidation	Ideal for glycoprotein immobilization
	Epoxy groups are a highly reactive group to many other groups	Orientation random
<i>Electrostatic</i>	Nitrilotriacetic acid (NTA) complex with Ni ²⁺ binds to poly-His tags (5-6 His) in proteins and peptides	Orientation of immobilization defined Reversible and relatively stable
<i>Specific</i>	Immobilization of avidin proteins (Streptavidin, Neutravidin) to biotinylated sensor surface or vice versa The biotin-avidin interaction is strong and highly stable.	Orientation of immobilization is defined
	Protein A can be easily immobilized onto the sensor surface and be used to capture IgG molecules	Directed orientation of immobilized IgG Reversible

Table 1. List of commonly applied BRE immobilization principles. Summarized from [74]

1.5.2. Hydrogel binding matrix

Although two-dimensional (2D) architecture mentioned above is used for studying different biomolecular interactions, with relatively simplistic models to describe analyte binding to immobilized BRE on the surface in terms of affinity studies, the coverage of BRE is limited to a monolayer. This can in turn limit the detection sensitivity of certain molecules that have low molecular weight or are present in trace amounts in real samples. To overcome the surface coverage limitation and make high density BRE sensor surfaces, polymer chains and networks known as polymer brushes or hydrogels can be utilized. Hydrogels are hydrophilic polymers forming a network by crosslinking through some structural units introduced during their synthesis. Many crosslinking chemistries exist, like benzophenone (BP) units through UV light irradiation, as well as other intrinsic property based crosslinking mechanisms like chain entanglement, electrostatic, hydrophobic and dipole-dipole interactions [75]. The formed polymer network is easily

hydrated by water, hence forming a hydrogel, which has a solid/liquid hybrid property. Hydrogels are composed of chemical monomeric subunit polymers called homopolymer if they are the same subunits or copolymer if there are different subunits. There are naturally occurring polymers that form hydrogels, mostly polysaccharides or polypeptides, and synthetic ones like vinyl derivatives (poly(meth)acrylic acid, poly(vinyl alcohol), etc.). The subunits forming the polymers ideally contain sufficient hydrophilic groups to maintain the hydrogel characteristic.

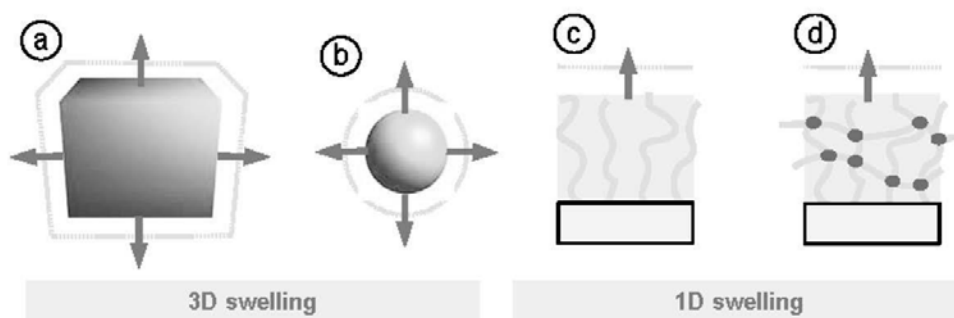


Figure 9. Depiction of 3D swelling of bulk hydrogels and 1D swelling of surface attached hydrogel films. A. 3D hydrogel, B. microgel, C. polymer brushes and D. surface attached hydrogel film. Image from [75]

The main morphologies of hydrogels as shown in Figure 9 are categorized as 3D hydrogels, microgels, polymer brushes and thin surface attached hydrogel films [75]. Through synthesis and conjugation of the polymer units with the above mentioned BRE immobilization chemistries (Table 1), these 3D structures can be used for biosensing as a high capacity binding matrix. Within the frame of this thesis, hydrogels as thin films will be further discussed in detail, focusing on their applications in biosensing and separation. For thin-film hydrogels on biosensor surfaces, naturally occurring dextran-based and synthetic *N*-isopropylacrylamide based hydrogels are prominently used [75], with the relevant crosslinker and surface attachment chemistries introduced into the polymeric monomer subunit through synthesis. The same crosslinkers can be used to attach hydrogels to gold in combination with the 2D chemistries. Other adhesion layers can also be used that allows stable attachment of hydrogel polymer chains to gold surface, such as thin layers of epoxy. To attach the polymer to the surface in the form of brushes, processes termed “grafting to” or polymer chains formed from precursors on the surface, termed “grafting from” can be used. To deposit the polymers on the sensor surface to form a hydrogel coating, several techniques can be applied such as spraying, casting and spin coating the polymer solution. Spin coating is used most prominently [75].

By carefully designing the lengths and spacings of the crosslinking units of the polymer chains, the mesh size of the hydrogel can be optimized [76]. This affects the overall morphology it takes when swollen and can be used to study molecular diffusion through this network [77]. The swelling can be influenced by the density of crosslinking, either through increased content of the crosslinking units in the polymer chains or post-synthesis crosslinking. Higher degrees of crosslinking reduces the polymer volume fraction in the swollen state, resulting in a compact hydrogel [78]. Density of the hydrogel is described by the swelling ratio, which is defined as the ratio between the thicknesses of swollen and dry hydrogel layer. Fluorescence correlation spectroscopy (FCS) is one of the methods to study the hydrogel mesh size and homogeneity of the network, by tracking the movement of fluorescent dyes and labeled macromolecules through the hydrogel matrix [79]. Several other techniques are used to study the structural properties of hydrogels on a surface such as dynamic light scattering (DLS) [80], X-ray scattering [81], atomic force microscopy (AFM) [82], ellipsometry [83] and SPR optical waveguide spectroscopy [84, 85].

Hydrogels can be responsive to external stimuli (light, heat and solutes) through incorporating chemical units that changes the polymer chain network morphology. These changes result in their collapse or swelling, and this aspect has found applications as actuators, pumps and valves, tissue and cell culture scaffolds, in biosensors and filters [75]. For the purpose of applying hydrogels as a high capacity binding matrix for biosensors, the diffusion characteristics of molecules through the network is fundamental [77]. In the design of hydrogels, parameters like polymer chain stiffness, amount of charged groups and crosslinking density are vital to obtain high interaction between hydrogel and water for efficient swelling and larger mesh sizes for the ease of solute and water diffusion. By controlling the diffusion of different sized solutes through the hydrogel matrix, filtration and separation can be performed [86, 87]. Hydrogels serving as selective filtration membrane can be prepared with the aid of other robust materials (nylon, polycarbonate and etc) as mechanical support [88].

Solid nanoparticles were introduced into the hydrogel matrix to improve certain properties such as mechanical strength. These nanoparticles can serve as the crosslinking unit or structural template and be grown within the matrix [89, 90]. Benzophenone functionalized silica nanoparticles were crosslinked with benzophenone modified poly-*N*-isopropylacrylamide (pNIPAAm) copolymers to form a composite film with enhanced robustness through reduced swelling, yet retaining the hydrogel polymeric thermoresponsive behavior [91].

1.6. SPR-based biosensors

1.6.1. Biorecognition elements

There are numerous reports on biosensors that take advantage of a variety of different BREs, including antibodies, peptides, oligonucleotides, aptamers, low molecular weight compounds and molecularly imprinted polymers (MIPs) [92]. The most prominently applied type of BREs are antibodies and the type of assay utilizing them for biosensors is called immunoassays. Antibodies are the product of the body's defense mechanism against external threats, for instance bacteria, virus, fungi and toxins, to name a few. From early on in the exposure, the body recognizes external species and recruits other defense mechanisms to recognize, destroy and eliminate, through different antibody and chemokine productions. From decades of immunological studies, several classes of antibodies were identified and understanding their exact mechanism is progressively improving. The main class of antibodies that are produced as a component of the humoral immunity is Immunoglobulin G (IgG) (Figure 10). Antibodies bind to the foreign body through the recognition of antigens and this interaction comprises the basis of immunoassay development.

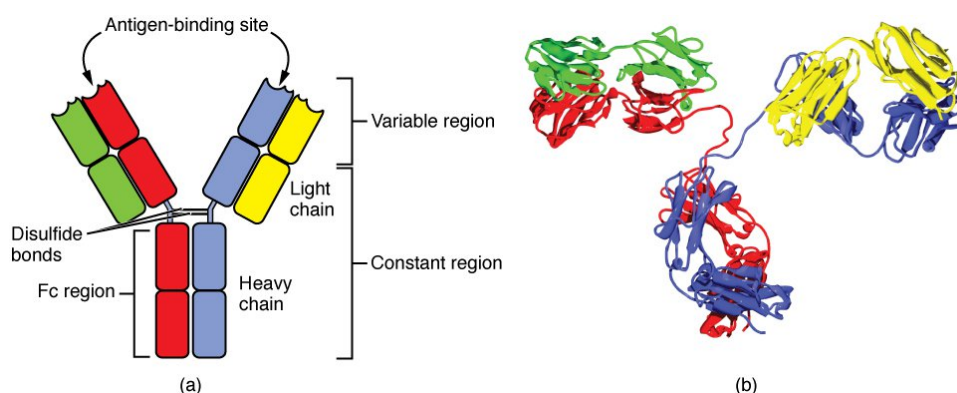


Figure 10. A. Graphical representation of the structural units and B. crystal structure of IgG molecule. Image from [93].

Antibodies, or the antigens they specifically bind to, can be immobilized onto solid surfaces in order to capture their affinity counterparts. Such interactions can be monitored by using biosensors. The types of immunoassays are classified and detailed in later sections. Antibodies or antigens serving as BREs can be immobilized through their signature moieties, like carboxyl, primary amine, sulfides and heavy regions by amine coupling, sulfide bonders and protein A, respectively. A summary of the coupling chemistries is mentioned previously in section 1.5.1 immobilization techniques. Antibodies are produced in polyclonal or monoclonal manner, depending on the different sources of production cells. Initially antigens are

prepared via conjugation to an immunogen carrier and either injected to laboratory animals to produce polyclonal antibodies, or produced by monoclonal hybridoma cell lines in a cell culture medium. The resulting pool of antibodies can be precipitated to obtain total immunoglobulins, affinity purified according the antibody classes or affinity purified for the specific antigen it was produced for [94]. As the antibodies recognize a certain structure or sequence of protein antigens called epitopes, that region can be independently used for biosensors [95-97]. The antigen binding variable region of the antibody can also be defined by sequencing methods. These short sequences of amino acids are called peptides and when their sequence is elucidated, they are easily mass synthesized.

MIPs are an emerging class of recognition elements that mimic the biological species. A 3-dimensional structural target binding pocket is imprinted into a polymer network forming a film or particles [98, 99] to specifically capture target analytes.

Another class of BREs appearing in spotlight is aptamers. They are oligonucleotide strands with sequences that bind to the target analyte through the specific conformations. RNAs were studied extensively for their intrinsic, self-sufficiency functionalities as early as 1980s in the context of ribozymes [100] that eventually lead to engineering of functional RNA introns [101]. To fully grasp the extent of RNA functions, a random library of sequences was ideal to establish and screen for possible functions. The production of such libraries was established and RNA sequences that interact with a given analyte were isolated. The term “aptamers” was first reported by Ellington and Szostak in 1990 [102] and the process through which aptamers are selected is termed Systematic Evolution of Ligands by Exponential enrichment (SELEX) reported by Tuerck and Gold also in 1990 [103]. The sequence space possible for oligonucleotides with a given length is vast (10^{43}) and the largest possible library produced had 10^{16} different sequences. First step in the SELEX procedure (Figure 11) is generating a random sequence library by mutation prone transcription, yielding sequences that are outside the common occurrence sequences. From the produced library of RNA or DNA sequences, ones with highest specificity and affinity are chosen and undergone binding and sequencing studies. It is possible for both RNA and DNA aptamers to bind to the same analyte, however their sequences can be unrelated (as shown for the DNA version of the RNA aptamer that binds adenosine triphosphate (ATP) [104]). Shortly following the initial upcoming of the selections, aptamers to various molecules were reviewed [105]. Further insights into the aptamer and analyte binding conditions revealed a significant requirement for metal ions for stabilization [106]. In order to further stabilize the oligonucleotides in environments where nucleases are present, sugar modification like 2'-O-Me, 2'-F or 2'-NH₂ can be introduced to protect ribozymes from degradation [107]. According to studies considering

the appropriate length of functional sequences, it is preferred to keep shorter sequences with maximum length around 70-80 bases [108] and even a minimalistic design was also possible with aptamers consisting of only 2 different bases [109]. The chosen aptamer sequences to different analytes may have similar secondary structure, yet completely different tertiary structure or vice versa [110]. The complexity in the secondary structure usually is an indicator of the affinity of the aptamer to its target, as illustrated by Carothers in 2004 [111]. It is associated with the likelihood of sequences yielding complex structures to exist in the random selection library being low. Engineering already existing conserved binding regions of an aptamer and adopting them during further selections with complex secondary structure yielding low probability sequences can help find higher affinity sequences. However, higher affinity aptamers do not always translate to high specificity [112]. Aptamers can adopt different conformations in the absence of the target binding, some having defined secondary structures whereas others are flexible and unstructured. Aptamer *in vitro* selection and isolation are simpler than that of antibodies, as they can interact directly with the target analyte without the complications of eliciting an immune response and the selection does not require recruitment of haptens or any other conjugations, especially small molecule ligands [113]. *In vitro* selection techniques are continually being improved from the initial reports to the recently developed technologies [114-118].

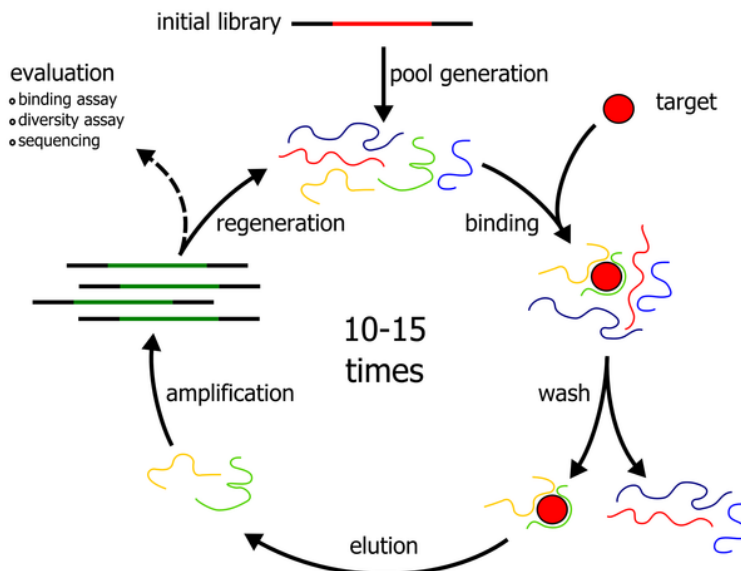


Figure 11. General scheme of a SELEX process. Image from [119]

The wide varieties of identified aptamers are applied to biosensors with different modes of readout principles. One prominent feature of aptamers is the possibility to design molecular beacons [120-122]. Aptamers are not only extensively used for diagnostic [123] and environmental monitoring biosensors

[27, 124], they have also been proven vital for therapeutics [125]. Recent progress in aptamer-based biosensors for monitoring of drugs in realistic samples [126-128] and integration into plasmonic nanoruler [129] have been reported.

1.6.2. Assay schemes

The most common assays applied for SPR-based biosensing can be categorized into several schemes depending on the nature of the interaction of the analyte with the BRE. These assay schemes are not only applied to immunoassays, but is translatable for any other assays with a different BRE. Direct immunoassay represents an assay where the capture antibody is immobilized onto the sensor surface, the antigen/analyte to be detected is in solution, and the binding event leads directly to a measurable signal. Components of the assay can be inverted to detect binding of antibodies to surface immobilized antigens. The analyte here can be non-labeled for direct SPR measurement [130] or labeled with fluorophores for SPFS detection [131]. Besides immunoassays, direct assays have been reported for numerous biosensors with MIP [132], peptide [133] and aptamer [134].

When the analyte exhibits molecular weight, that is insufficient to cause a detectable SPR signal change, signal enhancement methods such as conjugation to high refractive index label [135] is applied for competition assay [136]. The free analyte is spiked with conjugated analyte and introduced to the sensor surface where they compete in binding to immobilized antibody. The signal due to the conjugated analyte binding decreases with increasing concentration of free target analyte. Competition assays are suitable for detecting low molecular weight analytes like drugs and toxins with biosensors utilizing aptamers [137] and MIPs [138]. A similar scheme is employed in inhibition assay, which involves free analyte binding to the sites of the antibody spiked into the sample solution. The free analyte binding to the antibody inhibits its binding to surface immobilized conjugate of target analyte.

Alternatively, if the analyte is large enough to accommodate the binding of two antibodies, a sandwich assay is performed. Here, one antibody is immobilized onto the surface and allowed to capture the analyte, preferably with high affinity. Then, the detection antibody, responsible for causing a maximum detectable change in the biosensor signal is introduced to bind to a different site on the analyte. The detection antibody can either be unlabeled or labeled with gold nanoparticles (AuNPs) or fluorophores for signal enhancement. Aptamer based sandwich assays have been reported for the detection of various proteins [139-141] and other analytes [142, 143]. Also, a full length aptamer sequence was split in two or

more sections that bind into a complex in the presence of the analyte, but otherwise no interaction occurs between them [144].

1.7. State-of-the-art in surface plasmon field-enhanced fluorescence biosensors

The principle of surface plasmon field-enhanced fluorescence, which will be applied throughout this thesis, is also associated with names like metal-enhanced fluorescence (MEF) [145], surface plasmon coupled emission (SPCE) [146] and plasmon enhanced fluorescence (PEF) [58]. Since initial reports of applications of such types of optics for highly sensitive biosensors [67, 68], continuous improvements and exploitation to different aspects of biosensors are reported [147]. This section describes the recent progress on the enhancement of fluorescence with different plasmonic structures and their performances with regards to sensitivity.

Enhancement of fluorescence can be achieved through the different forms of SPs, namely the LSP, SPP and long-range surface plasmons (LRSP) [147]. As mentioned earlier, the decay length of SPPs is in the range of about 100 nm, which limits the probing depth. In order to probe longer distances or large analytes, LRSP with a strong evanescent field enhancement that can probe up to a micrometer into the adjacent medium was implemented. Here, the detection of the bacterial pathogen *E.coli* O157:H7 was demonstrated by using LRSP to probe the fluorescence signal from the fluorophore labeled detection antibody in a sandwich assay, with a detection limit of below 10 cfu/mL [148]. A similar approach was also applied to detect low molecular weight analyte aflatoxin M1 in real sample (milk) with a detection limit of 0.6 pg/mL using an inhibition immunoassay [149].

In order to further increase the sensitivity of similar biosensors, a hydrogel binding matrix was utilized to increase the surface density of BRE on the biosensor surfaces. Hence, LRSP fluorescence spectroscopy was applied to the detection of the cancer biomarker prostate specific antigen (PSA) in highly sensitive manner with the aid of a dextran based hydrogel binding matrix. Limit of detection (LOD) in the low femtomolar level (34 fM) in buffer and 0.33 pM in serum was reported [150].

Highly sensitive detection of PSA levels is important for the diagnosis of breast cancer [151] and prostate cancer [152], therefore much effort is put into the developments of sensitive PSA detection biosensors [153]. The LOD for PSA was further challenged by metallic nanoparticle-enhanced fluorescence

immunoassay and a lower detection limit of 12 fM in buffer and 52 fM in serum was achieved [154]. Recently, a plastic sensor chip was developed for a highly sensitive detection of PSA through surface plasmon field-enhanced fluorescence immunoassay. Two approaches of immunoassays were applied here, firstly a sandwich immunoassay comprising surface immobilized capture antibody and fluorophore labeled detection antibody to detect free PSA. Second, a two-step immunoassay with surface immobilized of anti-PSA antibody and fluorophore labeled *wisteria floribunda* agglutinin to detect GalNAc β 1–4GlcNAc-linked PSA, LacdiNAc-PSA in order to discriminate prostate cancer and benign prostate hyperplasia in patient sera. LOD of 0.04 pg/mL free PSA and 20 pg/mL for LacdiNAc-PSA was reported. The LacdiNAc-PSA determination with this system showed efficient discrimination of prostate cancer and benign hyperplasia with an area under the ROC curve of 0.851 compared to 0.559 for total PSA. The plastic sensor chip gave stable signal with both SPR and SPFS measurements [155].

The PEF concept was reported for application in microscopy to study live human epithelial kidney cells HEK 293 behavior upon stimulation with angiotensin-II, in terms of cellular contraction and actin structural changes. It has proven to be a powerful tool to elucidate the cellular footprints on the sensor surface [156].

Besides continuous gold films, sensor surfaces used to enhance fluorescence can be structured that allow PEF and SPCE. The amplification of fluorescence signal was achieved by using a crossed grating gold structure as the sensor surface by an epi-fluorescence readout as compared with continuous gold films. Such structures allow the near field coupling of SPs and fluorophores with a fluorescence signal intensity enhancement factor of two orders of magnitude as was predicted by simulations, which was in agreement with a sandwich immunoassay to detect a pro-inflammatory cytokine, Interleukin-6 (IL-6) [157]. In contrast, a similar sandwich immunoassay to detect IL-6 utilizing SPFS was reported to exhibit detection limit of 100 fM, with the advantage of direct immobilization of capture antibody to an unstructured sensor surface through dopamine coating [158]. A metal diffraction grating structure was applied to excite SPs that would then couple to concentric grating structures near a flat metal sensing area for an efficient focusing of the SPCE, where a fluorescence intensity enhancement more than 10-fold was achieved. A model immunoassay was used to demonstrate the sensing concept and a low detection limit of 11 pM was reported [159].

A very high field intensity enhancement was explored by the concept of LSP and SPPs to co-excite fluorescence on a gold nanohole array. A 50 nm thick gold layer with 140 nm diameter nanoholes were used to perform a fluorescence sandwich immunoassay for the detection of PSA, and in comparison to

singular LSP excitation of the fluorescence, co-excitation presented > 4-fold higher fluorescence signal intensity. The LOD for the co-excited fluorescence immunoassay (140 fM) was ~7-fold higher as compared to LSP excitation alone (0.9 pM) [160].

In addition to the different plasmonic structures implemented for the enhancement of fluorescence, utilization of a variety of fluorophores were reported. Yuan et al., recently reported the application of silicon substrates with around 200 nm silver islands (Ag@Si) for metal enhanced fluorescence microscopy for the detection of proteins and living cells. The fluorescence signal intensity when detecting proteins labeled with dyes with different emission wavelengths were studied, presenting strong wavelength dependency in the signal enhancement and the highest was observed for IR800 dye of 57.3-fold compared to bare Si surface. For fluorescence imaging of cells, IR800 dye labeling exhibited 4.1-fold increased fluorescence signal compared to reference Si substrate. This difference in the degree of enhancement between cells and proteins is possibly due to the probing height of fluorescence from the sensing surface, as protein detection assay would be much closer to the probing depth than cells [161].

A sandwich immunoassay with a detection limit of 0.01 ng/mL norovirus virus-like particles was reported with SPR-assisted fluorescence readout for quantum dot labeled detection antibody. Quantum dots (QD) are applied here for their large Stokes shift observed compared to typically applied fluorophore dyes, with the intent of reducing the sensor noise. The appropriate excitation wavelength 390 nm was chosen for the quantum dot label Qdot 705, according to the electric field intensity desirable for the Al film ($|E/E_0|^2=16.7$) and to minimize background noise. For the sensing area applied in this study, with a V-trench shape, the actual number of particles detectable was calculated as 100 virus-like particles [162]. Quantum dots were also applied for AuNP mediated FRET assay to detect influenza virus surface antigen hemagglutinins (HAs). An anti-HA antibody conjugated AuNPs and glycan modified quantum dots that form a complex in the presence of HA antigens, resulting in quenching of the QD fluorescence. Detection limit of 60 nM and 190 pM for H1N1-HA and H5N1-HA were reported, respectively. In sera, the LOD for both antigens were 0.96 nM [163]. Another scheme of utilizing QDs was reported for the detection for influenza virus H3N2. Here, a plasmon-assisted fluoro-immunoassay was constructed with anti-HA antibody immobilized carbon nanotubes (CNTs) with AuNPs (AuCNTs) that binds influenza viruses and an anti-NA conjugated CdTe QDs was used to complete the sandwich assay. The synergistic effect of both the CNT and AuNPs increased the plasmonic QD fluorescence intensity that was used to enhance the assay sensitivity. The detection system exhibited an 8-fold increase in signal intensity upon analyte binding

compared to no analyte blank and a detection limit of 50 PFU/mL H3N2 influenza virus, a value that is 100-fold higher than the commercial diagnostic kit counterpart [164].

Other plasmonic nanostructures have also been applied for PEF based biosensors. Based on the strong near infrared (NIR) field enhancement of noble metal nanoclusters and their low cytotoxicity and stability, gold nanoclusters were applied for live imaging. Gold nanoclusters functionalized with folic acid were used to detect and image in live mice Hela tumors via their expressed folate receptors (FR), through NIR fluorescence imaging system. The probe was proven to be highly specific and a sensitive imaging of cancers was possible [165]. Gold nanorods (AuNR) were applied to plasmonically enhance the NIR fluorescence signal from meso-tetra(4-carboxyphenyl)porphyrin (TCPP) and using SiO₂ layer as the spacer to fine tune their distance that favors the desired field intensity. When Cu²⁺ is added to this architecture, the fluorescence from TCPP is quenched and this formed the basis of the detection of pyrophosphate (PPi) in a fluorescence turn-on sensor, as Cu²⁺ and PPi forms a complex that dissociates from the sensor surface leading to fluorescence recovery of TCPP. With this method, detection limit of 0.82 pM PPi was achieved and also PPi detection in living cells was demonstrated [166]. Another approach for the detection of PPi upon quenching and recovering by Cu²⁺ was reported using NIR dye Cy7 in combination with gold nanobipyramids (AuNBPs) to enhance the fluorescence better than Au NRs. The LOD for PPi for this method was 80 nM and was successfully applied for the imaging of HeLa cells. Additionally, microRNA detection was performed with the approach through rolling circle amplification (RCA) technology based on the release of PPi from dNTPs during RCA process in the presence of the microRNA and polymerase, resulting in fluorescence recovery. The detection limit for the microRNA let-7d was 8.4 pM [167].

Many reports of fluorescence signal turn-on or turn-off approaches applying different homogenous assays and plasmonic nanoparticles or structures are reported [168-173]. A surface bound and quenched fluorophore labeled molecular beacon (MB) was used to detect a 24 bases oligonucleotide through their hybridization, resulting in the opening of the MB to an extended helix that brings the fluorophore at a distance that allows for PEF. This method allowed for efficient discrimination of single mismatch oligonucleotides to fully complementary targets. By simply washing the used sensor surface with water completely dehybridized the oligonucleotides, that allowed for the sensor to be reused more than 10 times [174]. A similar but modified approach that used sandwich-like assay to detect oligonucleotides based on the hybridization of Au surface bound capture probe with a target sequence and the fluorophore labeled detection probe was developed. The resulting PEF signal provided a detection limit of 50 pM for both targets comprising 40 and 60 Ts [175].

A recent work reports on a MB detection scheme concerning gold nanorod array sensor chips to enhance fluorescence signal. A fluorophore labeled MB was immobilized onto the hotspot region of arrayed AuNRs to obtain maximum enhancement of fluorescence. Initially the folded hairpin MB would be quenched through close proximity of the fluorophore to the surface and in the presence of complementary target sequence, the MB opens and hybridizes to a helical structure bringing the fluorophore away from the surface. This method allowed enhancement of fluorescence signal up to 0.8 and 10 pM LOD for a 45 nucleotide long target [176].

Excellent reviews on the enhancement of fluorescence through plasmonic structures are found, that give further insight into their progress and applications in biosensing [147, 177, 178]. It is observed that all reported PEF-based biosensors involve target analyte and BRE with high affinity binding or are homogenous assays with end-point measurements.

1.8. State-of-the-art in fluorescence aptamer sensors

Out of the different BREs typically applied to biosensors as discussed in section 1.6.1, aptamers are chosen for this thesis due to the flexibility of design and manipulation possible for this class of BREs. This choice stems from the intention of developing assays for reversible sensing of target analytes. Such reversible sensors can be achieved by employing BREs with low affinity interaction with the target analyte [179], avoiding regeneration and hence make continuous monitoring sensors possible. Since the initial report of aptamers [102, 103], an upsurge in their application in biosensors is seen with around 2000 hits in ISI webofknowledge by June 2017, and terminologies like “Aptasensor” are coined [180]. Their implementations range all types of biosensor transduction methods, however within the scope of this thesis, aptamer-based fluorescence sensors will be discussed in terms of current trends. Most prominent uses of aptamers for fluorescence biosensors are based on the single stranded and conformational switching properties of these oligonucleotides (mostly molecular beacon designs) and the high fluorescence quenching ability of graphene and carbon nanostructures as well as noble metal nanoparticles and films [181-183].

Graphene is a material that shows great potential for a wide variety of applications including sensing [184, 185]. Recent reports of graphene based “signal-on” or “signal-off” fluorescence aptamer sensors show detection of various target analytes. For example, a fluorescence turn-on aptamer sensor for the detection of epithelial cell adhesion molecule, EpCAM protein based on graphene quantum dots (GQDs)

as donor and molybdenum disulfide (MoS_2) as acceptors for FRET was reported [186]. In this report, a QGD labeled aptamer that binds EpCAM was adsorbed onto the MoS_2 causing fluorescence quenching through FRET and the fluorescence was recovered in the presence of analyte protein EpCAM as a result of aptamer QGD dissociation from the MoS_2 sheet. A LOD of 450 pM and a detection range from 3 – 54 nM was achieved, and this approach was additionally applied for the detection of breast cancer cell MCF-7 that expresses EpCAM. Joo et al., recently reported an aptasensor for aflatoxin B₁ (AFB₁) detection based on graphene oxide sheet fluorescence quencher and FAM dye labeled aptamer. Interestingly, the fluorophore-labeled aptamer in the absence of AFB₁ would have no interaction with the GO and hence give fluorescence signal, whereas in the presence of the analyte, the aptamer conformational change allows it to interact with graphene oxide (GO) and result in fluorescence signal intensity to be reduced (quenched). This method allowed to reach 4.5 ppb LOD [187]. The sensor specificity suffers slightly from interfering aflatoxins, a drawback that could be overcome by a different aptamer sequence. Alternatively, aptamers can easily adsorb onto GO surfaces in the absence of the analyte leading to the fluorescence dye label to be quenched, or in one case the fluorophore labeled complementary signal probe [188]. An ATP binding aptamer with an extra sequence that is complementary to the fluorophore labeled complementary sequence was adsorbed onto GO surface in the absence of the analyte, due to π -stacking, causing the fluorescence to be quenched. In the presence of the analyte-ATP, the probe and aptamer desorb from the surface that enables recovery of the fluorescence signal. In this report, a deoxyribonuclease (DNase) enzyme was used to recycle the target and enhance the fluorescence signal. When aptamer/probe is adsorbed onto GO, it is protected from the enzymatic cleavage and when in complex with the analyte, it is prone to cleavage allowing for target recycling as well as large amounts of fluorescent probes to be cleaved for amplified signal. This sensor allows the detection of ATP in 10 to 400 nM range, with 0.2 nM LOD.

Well-known hazardous compound bisphenol A detection with the use of “signal-on” aptamer sensor was reported [189]. Here, a fluorescein-labeled bisphenol A binding aptamer was adsorbed onto the surface of magnetic oxidation graphene (MGO) in the absence of the analyte, causing fluorescence quenching. Upon exposure to bisphenol A, the aptamer/analyte complex is formed and detaches from the MGO to yield recovery of the fluorescence signal. The composite of GO and magnetic Fe_3O_4 additionally permits efficient separation of MGO from the fluorescent probe, allowing for increased signal intensity and the recycling of MGO. The analytical performance was relatively good with a low detection limit of 0.071 ng/mL. An approach to covalently attach aptamers onto GO to study the stability of the probe to avoid nonspecific desorption from the surface was reported [190]. An aptamer specific for ATP labeled with a

fluorophore was immobilized onto GO through amine coupling and was applied for ATP detection in buffer and cells, and demonstrated improved performance and stability compared to physisorbed aptamer. Concentration of ATP from 0.125-2 mM in buffer was detectable and 31.8% fluorescence signal enhancement was achieved in comparison to physisorbed aptamer probe. This work highlights the importance of probe immobilization onto surfaces for increased stability and sensitivity of fluorescent sensors. Numerous other reports of graphene oxide based aptamer sensors for a wide range analytes are reported and a detailed review by Goa et al., on GO-DNA based sensors give a thorough update [191].

Besides application of graphene oxide as fluorescence quencher for aptamer based sensors, metallic nanoparticles are equally popular. Here, the fluorescence signal enhancement resulting from the localized surface plasmon or the fluorophore quenching by FRET from the metal surface is of interest and will be highlighted. It should be noted that reports on observation of these effects on immobilized aptamers is the main focus of this section. A mercury detection sensor applying fluorophore labeled aptamer immobilized onto AuNPs through sulfur groups was demonstrated. Due to the opening of aptamer structure in the absence of the analyte, fluorescence signal is generated by the fluorophore label located at an extended distance from the metal. In the presence of the analyte, the analyte/aptamer complex formation causes the fluorophore to move closer to the metal within the Förster radii and fluorescence quenching is observed as a function of the Hg^{2+} concentration. The sensor demonstrated LOD of 16 nM. and high specificity to mercury when tested against other metal cations [192].

In order to control the distance of the fluorophore from a metal surface for optimal fluorescence enhancement, Lu et al., [193] introduced 80 nm silica shell around the 50 nm silver nanoparticles (AgNPs) and applied Cy5-labeled aptamer probe to detect ATP. A complementary cDNA sequence to the aptamer probe was immobilized onto the silica coated AgNPs and in the absence of the analyte ATP, the two strands hybridized to give enhanced fluorescence from the surface plasmons. In the presence of the analyte however, aptamer sequence melts from the hybridized state which results in decrease in fluorescence. With this scheme, ATP was detected with LOD of 8 μM within a linear range of 0.008 to 0.5 mM.

A metal enhanced fluorescence readout of a bivalent aptasensor for Lactoferrin detection in milk was reported by Chen et al., [194]. The aptamer is split in two sequences that bind to different sites of the protein lactoferrin (Lac) and by modifying them separately with AgNP and fluorescein FITC, an enhanced fluorescence signal yield is made possible. In the absence of the analyte, the AgNP immobilized split sequence does not interact with the FITC labeled aptamer split segment, resulting in very low fluorescence

intensity. When the analyte Lac is present, both aptamers bind to the respective sites and FITC label coming in proximity to the metal nanoparticles emits high fluorescence signal. Consequently, 1.25 pM Lac detection limit was achieved and efficient detection was possible in 100-fold diluted milk spiked with the analyte.

QDs are also popularly utilized for fluorescence sensors aside from fluorescein or fluorophore dyes. Their high quantum yield, photostability, wide absorption spectra and tunable emission spectra by varying sizes make them preferable. Various applications of QDs in combination with metal structures for enhanced or quenched fluorescence for aptamer based sensors are reported, for instance surface plasmon field-enhancement from gold nanoholes [195], quenching by AuNPs in the absence of the analyte [196] and in presence [197].

This overview represents a number of possibilities to exploit aptamers and in order to achieve reversible sensors, it is evident that planar surface-based methods would need to be employed. By combining the structural switching properties of aptamers and the distance dependent effect of metal on fluorophores, the above reviewed (section 1.7) SPFS readout can be realized for aptamer-based fluorescence sensors. Additionally, the possibility of splitting aptamer full sequence to construct a sandwich-type assay [144] can be exploited for the same purpose. Interestingly, surface plasmon field-enhanced fluorescence or surface plasmon-coupled directional emission on metal films is reported in relatively lower numbers for aptamer biosensors thus far [198-200].

2. Research aims

This thesis aims at establishing sensor concepts that allow for the development of a new class of biosensors capable of continuous monitoring of target analytes. Such continuous monitoring sensors represent attractive tools for therapeutic drug monitoring (TDM), as demanded for instance for drugs with a narrow therapeutic range. Examples of such drugs are vancomycin, theophylline and digoxin, most of which cause toxicity at doses higher than its therapeutic range whereas lower doses lead to therapeutic inefficiency and patient suffering [201]. In current practice, therapeutic drug monitoring is carried out on samples collected at certain intervals and analytical methods requiring minutes to hours are applied to obtain quantitative results [202, 203]. Significant efforts at improving the real-time measurement aspect of TDM [204, 205] are reported for electrochemical [5, 127, 206] and optical detection methods [207, 208]. To realize such type of sensors, three main functionalities need to be implemented: assay to reversibly capture detect target analyte, biointerface design to allow long-term sensing in complex samples, and a sensitive detection method of analyte capture. The aims of the thesis address these challenges and the work is organized in the following three blocks:

1. The use of weak-affinity ligand [179] to establish a continuous and reversible biosensor, namely by choosing aptamers for their flexibility in design. The developed low-affinity aptamer-based reversible sensors are presented in Chapters 4 and 5.
2. Use hydrogel materials to serve as binding matrix and switchable filters. Low fouling, robust filter membranes are vital to the unperturbed performance of biosensors in biofluids for TDM. The means of constructing a stable, semi-permeable and free-standing membrane over a sensor area to apply for analysis in crude samples is presented in Chapter 6. Application of hydrogel material as binding matrix for immunoassay with enzymatic signal amplification method is presented in Chapter 7.
3. Implement optical readout method with increased signal-to-noise ratio. When applying low-affinity ligands for assays, the sensor would suffer from low sensitivity. In order to compensate for the loss of sensitivity, plasmonic amplification of optical signal can be implemented to increase signal-to-noise ratio. Chapters 4 and 5 describe the SPFS detection method applied to amplify the fluorescence signal for the reversible aptamer sensors.

3. Methods

The current section describes the general methods used in the following chapters of the thesis.

3.1. Spectroscopy instrumentation

3.1.1. Surface plasmon resonance and hydrogel optical waveguide spectroscopy

The SPR instrument (Figure 13) used in all measurements throughout the thesis was custom-built and employed the Kretschmann configuration. A Helium-Neon (HeNe) laser beam ($\lambda_{\text{ex}} = 632.8 \text{ nm}$) first passed through a polarizer (Glan-Thompson, Thorlabs, Germany) and then travelled through a chopper (frequency = 1331 Hz) connected to a lock-in amplifier (EG&G, Model 5210, Germany). The incident laser beam was coupled to LASFN9 prism (Schott, $n = 1.85$), where the sensor chip was optically matched using an index matching immersion oil ($n = 1.700$, Cargille Laboratories Inc, USA). The reflected beam is focused by a lens ($f = 30 \text{ mm}$, $\text{NA} = 0.2$) and detected by a photo-diode lock-in amplifier. Prism and sensor chip assembly was rotated by a stage to control the laser beam incident angle θ .

A dielectric medium placed between metal and low refractive index material can function as a waveguide. Dielectric waveguide modes can be guided within such geometry with a hydrogel film (waveguide) attached to gold surface. The propagation constant β of hydrogel guided waves can be defined from:

$$\tan(\kappa d_h) = \frac{\gamma_d n_h^2 / \kappa n_d^2 + \gamma_m n_h^2 / \kappa n_m^2}{1 - (\gamma_d n_h^2 / \kappa n_d^2)(\gamma_m n_h^2 / \kappa n_m^2)}. \quad \text{Eq. 3 [209]}$$

where n_d , n_h and n_m are the refractive indices of the aqueous dielectric, hydrogel and metal, respectively and d_h is the thickness of the hydrogel. The transverse propagation constants of dielectric, hydrogel and the metal are $\gamma_d^2 = \beta^2 - k_0^2 n_d^2$, $\kappa^2 = k_0^2 n_h^2 - \beta^2$ and $\gamma_m^2 = \beta^2 - k_0^2 n_m^2$, respectively. The resonant excitation of waveguide modes in the Kretschmann configuration is achieved by phase-matching, $k_0 \sin(\theta) = \text{Re}\{\beta\}$. Contrary to SPPs excited by the p-polarized light, transverse magnetic (TM) modes of the waveguide are detectable as well as the transverse electric (TE) mode. Through SPR spectroscopy with the Kretschmann configuration using p-polarized laser beam, an angular reflectivity spectrum $R(\theta)$ of the hydrogel layer structure can be performed and the corresponding waveguide modes are manifested as sharp resonant dips, numbered accordingly from the order of occurrence with increasing angle of θ (Figure 12). Observation of the field intensity profile of hydrogel waveguide modes revealed confinement within the hydrogel matrix. In comparison to SPR spectroscopy based biosensors, hydrogel optical waveguide

spectroscopy (HOWS) is highly sensitive to refractive index changes due to its high field intensity, a quality useful for biosensor applications. The thickness and RI information of the hydrogel matrix in different conditions can be determined using the Fresnel box model.

For HOWS measurements, the previously mentioned SPR setup was applied with the angular reflectivity spectra $R(\theta)$ measurements ranging from $45^\circ - 62^\circ$, with $0.01^\circ - 0.2^\circ$ steps. Angular ranges where waveguide modes occur required finer steps. All spectroscopy measurements were performed and recorded by the software WasPlas (Max Planck Institute of Polymer Research, Mainz, Germany).

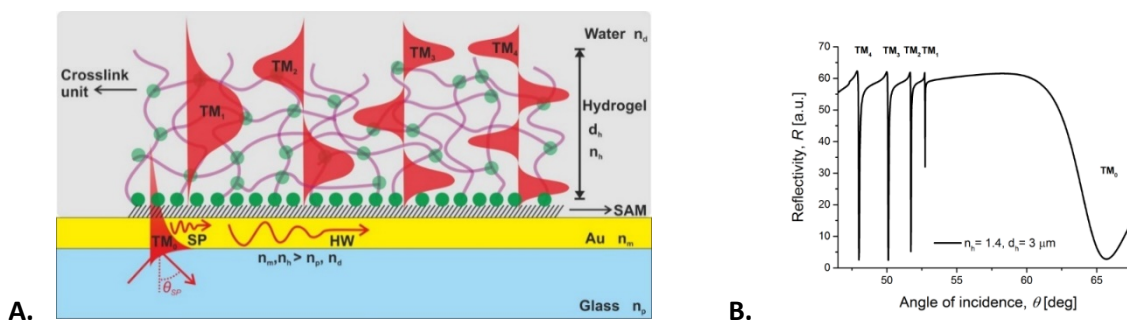


Figure 12. Left. A. Schematic depiction of the surface attached hydrogel sensor architecture for hydrogel optical waveguide spectroscopy and B. the corresponding angular reflectivity spectrum showing the TM modes.

3.1.2. Surface plasmon and hydrogel optical waveguide field-enhanced fluorescence spectroscopy

Surface plasmon-enhanced fluorescence spectroscopy (SPFS) and hydrogel optical waveguide fluorescence spectroscopy (HOW-FS) measurements were performed using the same optical setup as used for SPR, with the addition of fluorescence intensity measurement components. The fluorescence light emitted normal to the surface at a wavelength around $\lambda_{em} = 670$ nm was collected by an objective lens and then passed through two bandpass filters (transmission wavelength $\lambda = 670$ nm, 670FS10-25, Andover Corporation Optical Filter, USA) and a notch filter (central stop-band wavelength $\lambda = 632.8$ nm, XNF-632.8-25.0M, CVI Melles Griot, USA). Afterwards, it was coupled to a multimode optical fiber (FT400EMT, Thorlabs, UK) connected to an avalanche photodiode photon counter (Count-200-FC, Laser Components, Germany). The intensity of fluorescence light (F) was measured by a counter (53131A, Agilent, USA) in counts per second (cps). Where deemed necessary to reduce the emission intensity and avoid fluorescence dye bleaching, a neutral-density filter with an optical density of 2 ($OD = 2$, Linos Plano Optics) was applied.

As the same with SPFS (Figure 13), HOWS can be combined with fluorescence spectroscopy to observe the high field intensity aided fluorescence signal intensity from fluorophore labeled biomolecule interaction to the BRE present within the hydrogel matrix.

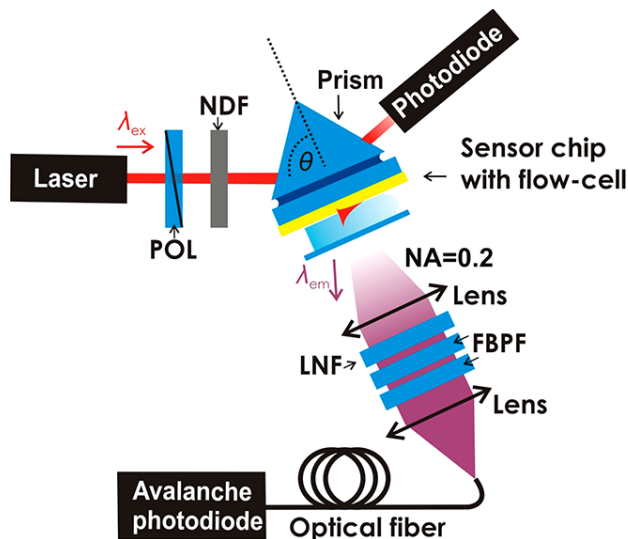


Figure 13. Schematic representation of the optical instrumentation setup applied for SPR, HOWS and fluorescence measurements performed throughout the thesis.

3.2. Biosensor preparation

3.2.1. Sensor chip preparation

The 2 x 2.5 cm BK7 glass substrates were washed with 1% Hellmanex (Hellma Optics, USA) solution for 25 minutes in sonicating water bath. Afterwards, the detergent was briefly rinsed with water and the substrates were washed for 25 minutes in MilliQ water (Arium Pro, Sartorius Stedim, Germany) with sonication. Lastly, glass substrates were rinsed and washed with absolute ethanol for 25 minutes while sonicating. All substrates were dried under stream of air before thermal evaporation of 2 nm chromium and 50 nm gold thin films using thermal vacuum evaporation instrument (HHV Auto306 Lab Coater, UK). After gold deposition, all sensor chips were rinsed with absolute ethanol, dried and stored under Ar atmosphere until further surface functionalizations.

3.2.2. Surface functionalization

All sensor chips used throughout the thesis were functionalized with silylthiols (henceforth referred to as thiols) or disulfide terminal groups.

Aptamer functionalization of sensor chips

For direct thiolated aptamer functionalization of sensor chip surface as depicted in Figure 14, 1 μM of aptamer buffer solution was reacted with gold in situ for 2 hours. The thiol modified aptamer sequences were reduced by 100-fold molar excess of Tris(2-carboxyethyl)phosphine hydrochloride (TCEP) for 4 hours in the Tris buffer (pH= 7,4, 10 mM Tris, 5 mM MgCl_2), to ensure that each aptamer contains monothiol. All liquid delivery to sensor surface was carried out through fluidic tubing (Tygon LMT-55) with the aid of a peristaltic pump (Ismatec, IDEX Health & Science SA, Switzerland).

In order to immobilize biotinylated aptamers, initially the sensor chips were immersed overnight in 1 mM ethanol solution of mixed biotinylated and pegylated thiols dissolved at a ratio of 1:9, under inert atmosphere by purging with Ar. After rinsing and drying, the biotin functionalized sensor chip was mounted onto the prism and a flow cell assembly with a thin polydimethylsiloxane (PDMS) gasket (thickness $\sim 130 \mu\text{m}$) was attached. Sensor surface was washed and allowed to stabilize in HEPES buffer (pH= 7.4, 20 mM HEPES, 150 mM NaCl, 5 mM MgCl_2 , 0.05 % Tween 20). Neutravidin solution with 50 $\mu\text{g}/\text{mL}$ concentration was flowed over the sensor surface for 1 hour to obtain a monolayer coverage followed by 5 minutes washing with buffer. Subsequently, 1 μM biotinylated aptamer in HEPES buffer was injected for 30 minutes and washed with buffer for 5 minutes.

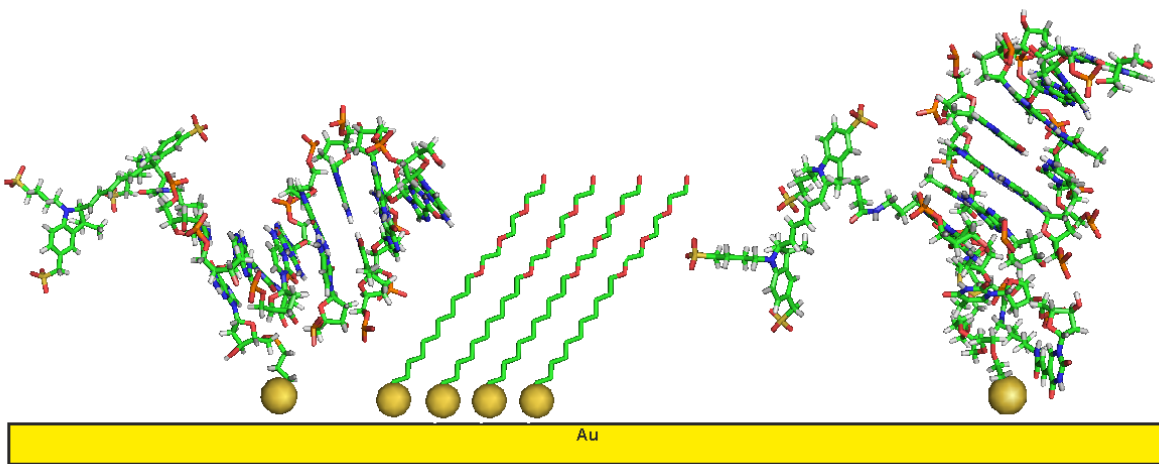


Figure 14. Direct immobilization of thiolated aptamer sequences onto gold sensor chips and thiolated PEG molecules for surface passivation.

Hydrogel film deposition

Sensor chips were immersed overnight in 1 mM solution of benzophenone disulfide (BP-diS, 4-AMBP University of Siegen, Germany [210]) dissolved in DMSO. After rinsing the benzophenone functionalized sensor chips with copious amounts of ethanol and drying under a stream of air, ethanolic solutions of pNIPAAm polymer was spin coated onto the surface at 2000 rpm for 60 seconds. The deposited polymer film was dried at 50 °C under vacuum overnight and subsequently attached to the gold surface by UV crosslinking the benzophenone groups with 365 nm UV light at irradiation dose of 4 J/cm². Uncrosslinked polymer chains were removed by washing with ethanol and the polymer coated sensors were dried and stored in the dark until use.

3.2.3. Data analysis

Determination of sensor surface properties

The surface mass density of the immobilized molecules and hydrogel can be calculated from the shift in the SPR angle seen from the angular reflectivity spectra. Obtained spectra are fitted using the transfer matrix-based model described elsewhere [211] implemented in the software Winspall (MPI for Polymer Research, Germany) and the RI n is determined, which then helps in determining the thickness d of layers formed above the sensor surface. When the RI and thickness values are available, the surface mass density Γ of immobilized layer is calculated as:

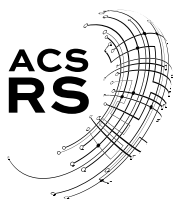
$$\Gamma = (n_h - n_b) \times d_h \times \frac{\partial c}{\partial n_h}. \quad \text{Eq. 4}$$

where n_h and n_b are the RI of hydrogel and buffer, respectively and d_h is the thickness of the surface immobilized layer. The RI change associated with the concentration of proteins is assumed as $\frac{\partial n_h}{\partial c} = 0.2 \mu\text{L}/\text{mg}$.

4. Plasmon field-enhanced fluorescence energy transfer for hairpin aptamer assay readout

Khulan Sergelen, Stefan Fossati, Aysegül Turupcu, Chris Oostenbrink , Bo Liedberg , Wolfgang Knoll, and Jakub Dostálek, *ACS Sensors*, 2017, 2 (7), pp 916–923.

DOI: [10.1021/acssensors.7b00131](https://doi.org/10.1021/acssensors.7b00131)



Plasmon Field-Enhanced Fluorescence Energy Transfer for Hairpin Aptamer Assay Readout

Khulan Sergelen,^{†,‡,§} Stefan Fossati,[†] Aysegül Turupcu,^{||} Chris Oostenbrink,^{||} Bo Liedberg,[‡] Wolfgang Knoll,[†] and Jakub Dostálek^{*,†}

[†]BioSensor Technologies, AIT-Austrian Institute of Technology, Muthgasse 11, 1190 Vienna, Austria

[‡]Nanyang Technological University, Centre for Biomimetic Sensor Science, School of Materials Science and Engineering, 50 Nanyang Drive, Singapore 637553

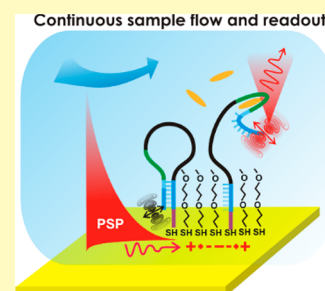
[§]International Graduate School on Bionanotechnology, University of Natural Resources and Life Sciences, Austrian Institute of Technology, and Nanyang Technological University, 1190 Vienna, Austria

^{||}University of Natural Resources and Life Sciences, Institute of Molecular Modeling and Simulation, Muthgasse 18, 1190 Vienna, Austria

Supporting Information

ABSTRACT: Surface plasmon field-enhanced fluorescence energy transfer is employed for sensitive optical readout of a reversible hairpin aptamer assay that is suitable for continuous monitoring of low-molecular-weight chemical analytes. A hairpin aptamer specific to adenosine and adenosine triphosphate with Alexa Fluor 647 fluorophore attached to its 5' end was anchored via 3' end thiol to a gold thin film. Molecular spacers were used to control the distance of the fluorophore from the surface in the aptamer "off" and "on" states. The specific binding of the target analyte changes the aptamer conformation, which alters the distance of the fluorophore from the gold surface and translates to variations in the detected fluorescence intensity. The plasmonically mediated fluorescence signal increases the measured signal-to-noise ratio and allows for real-time observation of the analyte binding. Theoretical as well as experimental study of the optical signal dependence on fluorophore orientation, design of spacers, and angular distribution of collected light is presented for rational design of the assay. The detected sensor signal increased by a factor as large as 23 upon switching the aptamer from the "off" to "on" state due to the hairpin opening associated with the specific capture of target analyte.

KEYWORDS: aptamer, surface plasmon field-enhanced fluorescence, plasmonic amplification, quenching, adenosine triphosphate, fluorescence energy transfer



The coupling of fluorophores with the confined field of surface plasmons originating from collective oscillations of the electron density at metallic surfaces offers powerful means for the amplification of emitted fluorescence light intensity.^{1,2} The plasmonic confinement is associated with the enhanced intensity of the electromagnetic field and the local density of optical states which has been exploited in fluorescence studies of single molecules³ as well as in the measurement on ensembles of fluorophore-labeled biomolecules.^{4,5} The interaction of fluorophore labels with the plasmonically enhanced electromagnetic field allows an increase of excitation rate and improvement of the collection yield of emitted fluorescence photons. The combined coupling of fluorophores at their absorption and emission wavelengths with propagating surface plasmons (PSPs) on metallic films or localized surface plasmons (LSPs) at metallic nanoparticles can be engineered to enhance detected fluorescence intensity by a factor exceeding 3 orders of magnitude.⁶

In plasmonically amplified fluorescence assays, biomolecules that are labeled with fluorophores are affinity captured on a metallic sensor surface at distances in the range of 15–20 nm at

which the plasmonic fluorescence enhancement typically reaches its maximum.^{7–9} At shorter distances the quenching becomes dominant and the emitted fluorescence signal is attenuated rather than enhanced while at longer distances the binding events occur outside the evanescent surface plasmon field. Aptamers become increasingly popular in analytical technologies for specific capture and sensitive detection of low-molecular-weight analytes^{10,11} for which more commonly used antibody immunoassays are not possible. These versatile building blocks can be employed in numerous detection formats that take advantage of the measurement of fluorescence quenching,¹² plasmonic fluorescence enhancement,¹³ or plasmonic near-field coupling between metallic nanoparticles.¹⁴ Such variety of readout modality is possible through the flexibility in aptamer design that can be tailored for assays relying on conformation changes,¹⁴ displacement,¹⁵ or formation of sandwich¹⁶ which are architectures not possible

Received: March 3, 2017

Accepted: June 21, 2017

Published: June 21, 2017

to realize with conventionally used antibodies against low-molecular-weight analytes. A particularly interesting aspect of the aptamer flexibility in design is the possibility of their implementation to molecular beacon-based biosensors. In short, single-stranded nucleic acids are modified at their opposite ends with a fluorophore and a quencher and specific analyte binding is detected by changes in the fluorescence intensity. Fluorescence intensity is mediated by the aptamer analyte complex formation that leads to structural changes or most commonly displacement of complementary stem region of a hairpin aptamer, rendering the quencher and fluorophore pair to separate to a distance farther than energy transfer or quenching to occur.¹⁷

The majority of plasmon field-enhanced fluorescence assays that has been pursued with aptamers carrying a fluorophore attached to their DNA or RNA strand relied on chemically synthesized metallic nanoparticles that support LSPs. These modes typically confine electromagnetic energy at distances of few tens of nanometers and they have been used in fluorescence displacement assays that employ the distance-modulated plasmonic enhancement¹⁸ of fluorescence signal or quenching.¹⁹ In these works, the difference in the fluorescence signal from the aptamer with and without analyte captured was typically <6-fold. An aptamer fluorescence assay that is mediated by PSPs on metallic films has been reported to offer higher, 18-fold change, of fluorescence intensity upon analyte binding²⁰ when probed with less confined PSP field reaching about 100 nm from the metal surface.

This paper reports on the reversible direct detection of a small molecule analyte by conformational changes of a hairpin aptamer which is labeled with a fluorophore and attached to a metallic film supporting PSP modes. Plasmonic amplification of the fluorescence signal enabled in situ continuous monitoring of variations in concentration of low-molecular-weight analytes—adenosine and adenosine triphosphate. By using simulations and experiments, the rational design of the aptamer molecular spacers and optical readout is investigated based on the emitted fluorescence intensity dependence on distance, orientation of the emitter, and angular range used for the collection of the fluorescence light.

EXPERIMENTAL SECTION

Materials. Sodium chloride, tris hydrochloride, 4-(2-hydroxyethyl)-piperazine-1-ethanesulfonic acid (HEPES), polyethylene glycol sorbitan monolaurate (Tween 20), magnesium chloride hexahydrate, adenosine, guanosine, adenosine 5'-triphosphate (ATP) disodium salt hydrate, and tris(2-carboxyethyl)phosphine hydrochloride solution (TCEP) were purchased from Sigma-Aldrich (Austria). (11-Mercaptoundecyl)triethylene glycol (PEG-thiol, SPT-0011) was obtained from SensoPath Technologies (USA). Two DNA aptamers were synthesized by Integrated DNA Technologies (IDT-DNA, Leuven, Belgium). The ATP hairpin aptamer with the short loop sequence (SLA) consisted of Alexa Fluor 647N 5'-CA CCT GGG GGA GTA TTG CGG AGG AAG GTT PEG6 CCA GGT G-SH 3' and the long loop ATP hairpin aptamer (LLA) sequence was Alexa Fluor 647N 5'-CA CCT GGG GGA GTA TTG CGG AGG AAG GTT TTT CCA GGT G TT PEG6 -SH 3'. All reagents were used as received and buffer solutions were prepared using ultrapure water (Arium Pro, Sartorius Stedim).

Preparation of the Sensor Chips. A BK7 glass substrate was coated with 2 nm Cr and 50 nm Au films by thermal vacuum evaporation (Model HHV FL400, HHV Ltd., UK). The Au surface was rinsed with ethanol, dried under a stream of air, and stored under argon atmosphere until use. LLA or SLA aptamer was dissolved at

concentration of 1 μM in 200 μL of 10 mM Tris buffer (pH = 7.4) containing 6 mM MgCl_2 . Afterward, the aptamer was reacted with 100-fold excess TCEP (100 μM). After 4 h of incubation, the reduced ATP hairpin aptamer solution was spiked with PEG-thiol at concentration of 10 μM and the mixture was flowed over the Au surface in a closed loop system for 2 h in order to form a self-assembled monolayer (SAM).

Optical Setup. A schematic of the optical setup can be seen in Figure 1. The sensor chip with the aptamer biointerface on top was

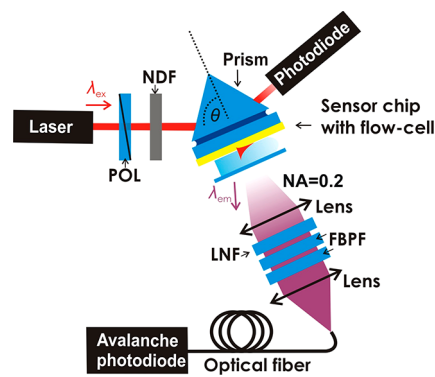


Figure 1. Schematics of the optical configuration used in the surface plasmon field-enhanced fluorescence measurements.

optically matched to an LASFN9 glass prism by using refractive index matching oil (from Cargille Inc., USA). The HeNe laser ($\lambda_{\text{ex}} = 632.8$ nm, ~ 2 mW) beam was transverse magnetically (TM) polarized by passing through a polarizer (POL) and was coupled to the prism to resonantly excite the PSPs by the Kretschmann configuration of the attenuated total reflection (ATR) method. The prism and sensor chip assembly was mounted on a rotation stage to control the angle of incidence θ and the angular reflectivity spectra $R(\theta)$ were measured by a photodiode detector connected to a lock-in amplifier (EG&G, USA). The enhanced field intensity occurring upon the coupling to PSPs at a resonant angle θ_{SPR} were used to excite Alexa Fluor-647 molecules at the sensor surface. The fluorescence light emitted at a wavelength around $\lambda_{\text{em}} = 670$ nm to the direction normal to the surface was collected by a lens (focal length 30 mm, numerical aperture of $\text{NA} = 0.2$), passed through two bandpass filters (FBF, transmission wavelength $\lambda = 670$ nm, 670FS10-25, Andover Corporation Optical Filter, USA) and a notch filter (LNF, central stop-band wavelength $\lambda = 632.8$ nm, XNF-632.8-25.0M, CVI Melles Griot, USA). Then the fluorescence light was coupled to a multimode optical fiber (FT400EMT, Thorlabs, UK) that was connected to an avalanche photodiode photon counter (Count-200-FC, Laser Components, Germany). Its intensity (F) was measured by a counter (53131A, Agilent, USA) in counts per second (cps) and recorded by the software Wasplas (Max Planck Institute for Polymer Research, Mainz, Germany). During the fluorescence measurements, the intensity of the laser beam illuminating an area of about 1 mm^2 was decreased by using a neutral-density filter (NDF, optical density $\text{OD} = 2$, Linos Plano Optics) in order to reduce the effect of fluorophore bleaching. The measurement of reflectivity R and fluorescence intensity F as a function of time t was performed at an incidence angle θ that was fixed close to the resonance.

Aptamer Assay. A flow-cell with a volume of 10 μL was clamped to the sensor surface to contain liquid samples transported via fluidic tubing (Tygon LMT-55) with 0.25 mm inner diameter at a flow rate of 15 $\mu\text{L}/\text{min}$. The flow-cell consisted of a PDMS gasket (thickness of ~ 130 μm) and a transparent glass substrate with drilled inlet and outlet ports. Throughout the assay measurements, 10 mM Tris buffer (pH = 7.4) containing 6 mM MgCl_2 was used (further referred to as hairpin aptamer assay buffer—HAB), which was similar to the buffer condition used during the aptamer selection process with minor modifications.²¹ Following the aptamer immobilization, the sensor surface was washed for 15 min with HAB to establish a stable baseline

target analyte. Visualizations of possible conformations of the studied aptamers were created in the Molecular Operating Environment (MOE, 2013.08, Chemical Computing Group Inc., Canada).

RESULTS AND DISCUSSION

As seen in Figure 2a, the gold sensor surface carried a DNA hairpin aptamer anchored via a thiol group at its 3' end. The thiol-PEG SAM was used to dilute the surface density of the aptamer to reduce steric hindrance during analyte binding and aptamer unfolding, as well as to serve as an antifouling carpet. The aptamers specific to adenosine and adenosine triphosphate (ATP) were derived from the structure which was reported to exhibit dissociation constant in the bulk solution of $K_d \sim 6 \mu\text{M}$ for adenosine.²¹ In order to utilize a readout strategy based on surface plasmon field-enhanced fluorescence energy transfer, the 5' end of the aptamer strand was labeled with Alexa Fluor 647N dye. Seven bases of the aptamer at two locations close to the 5' and 3' ends were designed to be complementary (marked blue in Figure 2a) to form the stem. By using these sequences, the aptamer forms a hairpin structure with the fluorophore present close to the metal surface at a distance of f_{off} . The sequence of the stem region close to the 5' end partially overlaps with the sequence of 22 bases that is specific to the target analytes adenosine and ATP (analyte specific segment marked green in Figure 2a). Therefore, the affinity binding of ATP disrupts the hairpin structure and switches the aptamer to its open conformation state with a fluorophore present at longer distance f_{on} from the gold surface. By using molecular spacers between the thiol anchor and the stem sequence (spacer 1) and between the stem sequence and the analyte specific sequence (spacer 2), the distance between Au and Alexa Fluor 647 dyes in the "off" state f_{off} and in the "on" state f_{on} can be tuned in order to achieve a maximum difference in the detected optical signals.

Distance of the Fluorophore from the Surface. Two designs of ATP aptamers with different molecular spacers 1 and 2 were used. The long loop aptamer—LLA—carried spacer 1 with 6 PEG groups and two T bases between the anchor group and the 3' stem sequence. In addition, spacer 2 composed of 32 T bases was inserted between the ATP specific sequence and the stem sequence. The second hairpin aptamer with short loop sequence—SLA—had no spacer 1 and a shorter spacer 2 (two T bases and 6 PEG groups). To estimate the distance between the fluorophore and gold surface in the "off" and "on" states, possible conformations of the SLA and LLA were analyzed. Two examples of conformations of the stem region with the fluorophore in the closed hairpin SLA and LLA can be seen in Figure 2b. The distances of the fluorophore from the metal surface in the absence f_{off} and the presence f_{on} of the analyte were estimated based on random-coil model for polymers. For LLA with longer molecular spacers, the average distance in the closed hairpin conformation was estimated as $f_{\text{off}} \sim 1.6$ nm and in the open hairpin conformation as $f_{\text{on}} \sim 6.6$ nm. In the closed hairpin conformation, the spacer 1 (6 PEG groups and two T bases) and linker between the fluorophore and the aptamer were assumed to be flexible. Similarly, for the SLA the average distances were estimated as $f_{\text{off}} \sim 0.9$ nm and $f_{\text{on}} \sim 5.2$ nm (see summary in Table S1). The range of rotational freedom of the fluorophore dye attached to SLA and LLA in the f_{off} state is visualized in Figure S1. The Alexa Fluor 647N dye in SLA appears less flexible as compared to LLA where it possesses a broader range of possible conformational states (rotational freedom). As in the readout of the assay, the fluorescence signal

$F(t)$ is collected with about 1 s integration time, the orientation of the fluorophore is expected to be averaged and the mean polar angle is $\Xi \sim 60^\circ$ for both "off" and "on" states when the fluorophore is free to rotate. For SLA in the closed hairpin, the fluorophore is in close proximity to the gold surface which may sterically hinder its rotation and thus a parallel orientation is likely preferred, $\Xi > 60^\circ$ (note that a parallel orientation of the dipole corresponds to $\Xi = 90^\circ$ and the perpendicular orientation to $\Xi = 0^\circ$).

Simulations of Competing Plasmonic Enhancement and Quenching. The optical response of Alexa Fluor 647N to conformation changes of the investigated SLA and LLA aptamers between the closed and open hairpin states were numerically simulated by FDTD. As Figure 3a shows, PSPs

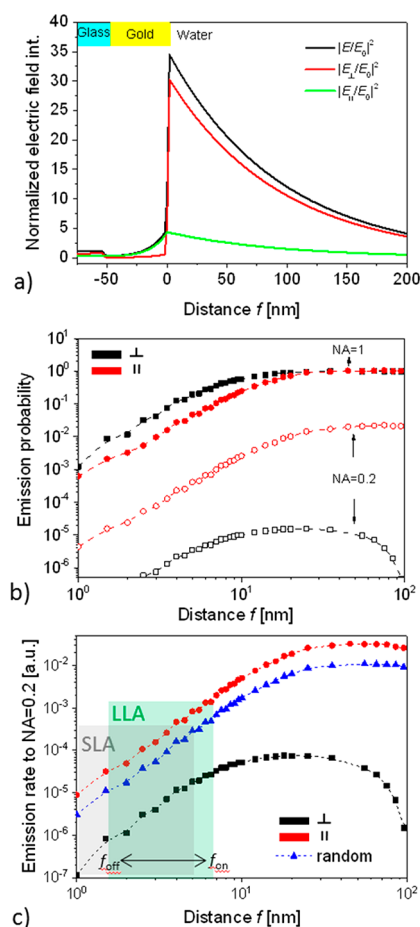


Figure 3. (a) Simulated parallel and perpendicular component of electric field intensity upon the resonant excitation of PSP at $\lambda_{\text{ex}} = 633$ nm depending on distance from the surface f . (b) Emission probability for a dipole representing the fluorophore emitting at $\lambda_{\text{em}} = 670$ nm to a cone above the gold surface with NA = 0.2 and NA = 1 as a function of distance f and dipole orientation. (c) Emission rate of a fluorophore emitting to NA = 0.2 at $\lambda_{\text{em}} = 670$ nm that is excited via PSPs at $\lambda_{\text{ex}} = 633$ nm for its parallel and perpendicular orientation and varied distance f .

probe the gold–water interface with a characteristic profile of the electromagnetic field that evanescently decays away from the gold surface with a penetration depth of about $L_p = 190$ nm (defined as the distance from the surface at which the field amplitude $|E|$ decreases by a factor of e). In addition, it shows that the field component $|E_{\perp}|^2$ that is perpendicular to the

surface is enhanced by a factor of about 35 with respect to that of the incident field component. The intensity of the parallel component $|E_{\parallel}|^2$ is approximately 5 times lower than that of the perpendicular one $|E_{\perp}|^2$.

In general, the radiation of fluorescence emitter placed above the plane interface between gold and water can be quenched, coupled via the near field to PSPs traveling along the gold surface, or it can be emitted to the far field. The total emission probability to the far field (represented by numerical aperture $NA = 1$) from a radiating dipole above the gold surface is close to 1 at long distances and it rapidly drops when decreasing the distance f below 15 nm, see Figure 3b. These data also reveal that the emitter oriented parallel (\parallel) to the gold emits to the far field with smaller probability than that with perpendicular orientation (\perp). Interestingly, this behavior is opposite if light is only collected to a narrow cone of angles close to the normal direction. The reason for the stronger emission probability from the parallel dipole (that is more quenched) into the normal direction is that emission occurs dominantly in the direction normal to dipole oscillation. Let us note that for the in situ measurement of fluorescence signal through a flow-cell, the numerical aperture NA of lens used for the collecting of fluorescence light is limited as it cannot approach close to the sensor surface. The value used herein of $NA = 0.2$ holds for typically used configurations in diffraction as well as ATR-based plasmon field-enhanced fluorescence biosensors.²⁵

Figure 3c presents the emission rate of fluorophore that is coupled by the resonantly excited PSPs waves at wavelength λ_{ex} which occurs in a narrow angular range within $NA = 0.2$. It shows that the difference between the emission probability from parallel (\parallel) and perpendicularly (\perp) oriented emitter is partially compensated by the stronger excitation of perpendicular dipoles (see $|E_{\perp}|^2$ in Figure 3a) than parallel dipoles (see $|E_{\parallel}|^2$ in Figure 3a). For short distances ($1 < f < 15$ nm), the emission rate rapidly increases with increasing distance similar to the emission probability as the PSP field decays slowly. However, when increasing the distance f toward the PSP penetration depth, the emission rate decreases with the distance as the excitation field gets substantially weaker. In summary, simulations predict that fluorescence intensity detected from a fluorophore that is placed at the distance $f < 15$ nm and excited with enhanced PSP field is more than an order of magnitude stronger for the parallel dipole orientation (\parallel) than for the perpendicular orientation (\perp). The emitted fluorescence intensity rapidly increases with the distance f . For the estimated changes in the distance of randomly oriented emitter attached to LLA, the simulated intensity increase for the distance switch from $f_{\text{off}} = 1.6$ nm to $f_{\text{on}} = 6.6$ nm is a factor of about 45. For the SLA aptamer with preferably parallel oriented dye in the closed hairpin conformation, slightly lower fluorescence signal change of about 40 is predicted when the distance changes from $f_{\text{off}} = 0.9$ nm to $f_{\text{on}} = 5.2$ nm.

Measurement of Plasmon Field-Enhanced Fluorescence Energy Transfer Aptamer Assay. As seen in Figure 4a, the resonant excitation of PSPs at λ_{ex} manifests itself as a narrow resonant dip in the reflectivity spectrum $R(\theta)$. Interestingly, the measured reflectivity spectra did not show significant shift of the SPR dip located at θ_{SPR} upon the binding of ATP which increases refractive index on the surface and also leads to its redistribution due to the conformation change of the aptamer. The lack of SPR signal to such variations can be ascribed to two effects. First, ATP exhibits low molecular weight (507.2 Da) which translates to weak increase in

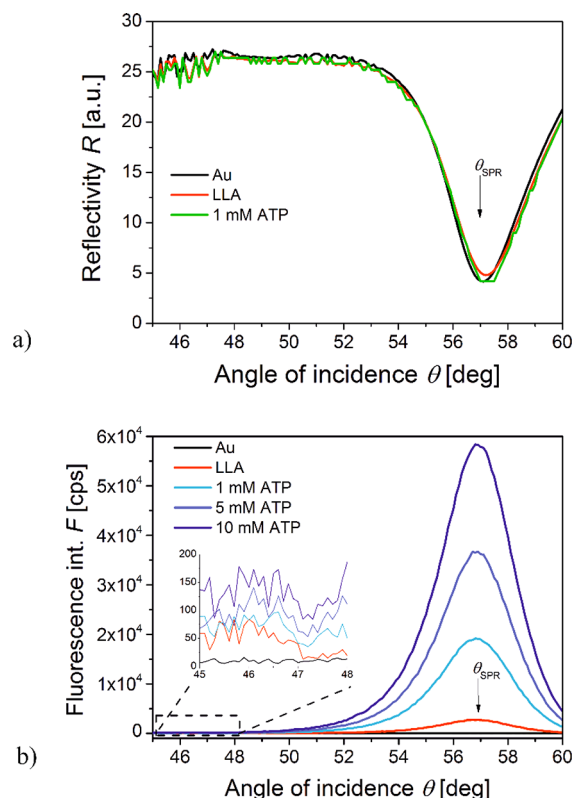


Figure 4. (a) Angular SPR reflectivity spectra $R(\theta)$ and (b) respective fluorescence intensity spectra $F(\theta)$ measured for a sensor surface in contact with HAB buffer spiked with the concentration of ATP of 0, 1, 5, and 10 mM. The gold sensor surface was functionalized with LLA.

refractive index that is proportional to $\delta\theta_{\text{SPR}}$. Second, the switching of the aptamer from its closed to open loop conformation by the capture of ATP should lead to counteracting small decrease in θ_{SPR} . Decrease of SPR angle by about $\delta\theta_{\text{SPR}} = 0.01\text{--}0.02^\circ$ was reported for swelling of polymer brushes with molecular weight 50–3000 kDa²⁶ which was attributed to increase in their thickness and accompanied decrease in refractive index. The switching of the aptamer structure should lead to similar effects, but as its molecular weight of 22.6 kDa is lower, the respective SPR changes are expected to be weaker.

In the surface plasmon field-enhanced fluorescence regime, the resonant coupling to PSPs leads to the excitation of attached Alexa Fluor 647 dyes which can be seen as a strong peak in the fluorescence intensity F centered at an angle θ slightly lower than that where SPR occurs (see Figure 4b). Interestingly, the maximum fluorescence intensity occurs at angle θ that is slightly lower than that where the minimum reflectivity occurs. Such small angular shift can be attributed to the interference between the laser beam, that directly reflects from the gold layer and undergoes a phase shift and the resonantly excited surface plasmon waves that are leaky to the substrate. When incubating the sensor surface with the ATP target analyte, an increase in the fluorescence signal F is observed. This is caused by a change in the aptamer conformation that leads to an increase in the distance of the emitter from the surface f and reduced effect of quenching. Experimental measurements with SLA show 10.3-fold increase in fluorescence intensity for 12 mM ATP in comparison to the measurement taken in the absence of analyte, while for LLA, a

stronger 23.3-fold increased fluorescence intensity was observed. For the SLA, this value is about 4-fold lower than predicted and for the LLA aptamer, the measured value is about 2-fold lower than predicted. These discrepancies can be attributed to inaccuracy of the model, particularly to the simplified means of determining the distances in the open and closed hairpin conformation and approximations used in the FDTD simulations where the size of the real emitter (of about 2 nm) was replaced by an infinitely small dipole.

Real-Time Detection of the Reversible Aptamer Interaction with Target Analyte. For the experimental observation of affinity interaction with tethered aptamers, the angle of incidence was set close to $\theta_{\text{SPR}} = 57^\circ$ (where the strongest fluorescence signal amplification occurs) and the fluorescence intensity was measured as a function of time $F(t)$. As can be seen from Figure 5, the injection of the HAB spiked

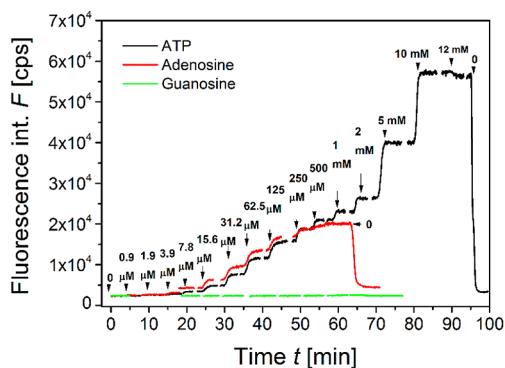


Figure 5. Example of the fluorescence signal $F(t)$ measured at a fixed angle $\theta = 57^\circ$ during titration of ATP, adenosine, and guanosine at concentration increments up to 12 mM in HAB buffer. Gold sensor surface was functionalized with LLA.

with ATP leads to a rapid increase in the fluorescence signal F . Increasing the ATP concentration from 0.9 μM to 12 mM leads to a gradual increase in equilibrium signal F . Exposure to the highest concentration followed by rinsing in buffer (without the analyte) resulted in a rapid dissociation of the ATP-aptamer complex that manifests itself as a drop of the fluorescence signal to the original baseline value F_0 . This observation confirms a fully reversible aptamer interaction for repeated measurements without regeneration. Moreover, virtually no bleaching of attached dyes was observed over the time course of the experiment. The aptamer assay showed a comparable reversible response for the detection of adenosine, but no observable response was recorded for the negative control—guanosine—which is a structural analogue of adenosine. The data for the long LLA ligand shown in Figure 5 were similar for the SLA (Figure S2).

Calibration Curves. From the data of the titration measurements, the equilibrium response F was obtained for each analyte concentration. The limit of detection (LOD) was determined as the concentration at which the calibration curve intersects with the value of the background signal F_0 plus 3 times the standard deviation, $3\sigma(F_0)$.

For SLA, the determined LOD for ATP was 108 μM and 24 μM for adenosine. This was greatly improved by the LLA where LOD values were $\sim 1\text{--}2$ μM for both ATP and adenosine. The obtained detection limits of the sensor is within the reported values in the literature, that ranges over several orders of magnitude (ATP detection limits from 0.5

μM ²⁷ up to 0.65 mM²⁸) for a plethora of fluorescence detection schemes.^{29,30} Although our reported sensor may fall in the low sensitivity range, it is comparable to surface supported real-time detection sensors^{31,32} and has the added value of effortless reversible detection. As can be seen in Figure 6a, the baseline

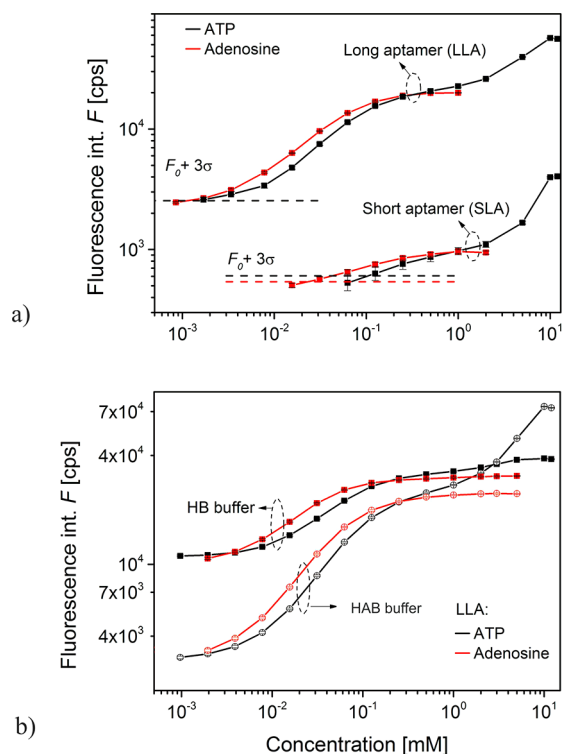


Figure 6. Calibration curves measured with SPFS detection principle for ATP and adenosine analytes. Each data points (ΔF) derived from triplicate titration measurements (an example shown in Figure 4). (a) Comparison of the response for LLA and SLA aptamers and analyte dissolved in HAB buffer. (b) Comparison of the response for LLA aptamer and analytes dissolved in HAB and HB buffers.

fluorescence intensity is higher for the interface with LLA compared to that for SLA. This can be attributed to its longer distance in the “off” aptamer state— f_{off} —(see Table S1) which is accompanied by higher emission rate (see Figure 3c). In addition, K_d values were determined from the calibration curves fitted with Langmuir isotherm model (presented in the Supporting Information) and the K_d for adenosine was of 90 μM for SLA and of 50 μM for LLA (Figures S3a,b). The calibration curves for ATP in both aptamers deviated from the Langmuir isotherm (Figure 6a). However, fitting the calibration curve for ATP concentrations up to 2 mM, where initial slight saturation was seen (Figure 5a), yields K_d values of 300 μM and 120 μM for SLA and LLA (Figure S3c,d), respectively. These values are probably increased by either the interaction of the strongly negatively charged molecule ATP with the surface-anchored aptamer that carries also negatively charged fluorophore, possibly affecting its orientation. It is worth of noting that the overall reduced affinity of fluorophore labeled aptamers with respect to the unmodified one was reported previously.^{33,34} Besides the molecular charge mentioned above, surface and label induced reduction in affinity of the aptamer, the competition of target-induced conformational change from the initial closed hairpin state is a likely contributor.

It was reported that the ATP binding aptamer can be described using a “conformational selection” recognition of ATP where the analyte-free state is more stable in high salt concentration, which leads to a deteriorated distinction of conformational changes when ATP is bound.³⁵ Therefore, the assay buffer (HAB) used in this study did not contain NaCl, in order to increase the contrast between aptamer conformations in analyte-free/hybridized and analyte bound states. However, it is important to observe the performance of the assay in buffers with compositions similar to samples relevant to applications in the field of medical diagnostics. For this purpose, HEPES buffer (HB) with salt concentration close to physiological conditions was used to evaluate LLA. Fluorescence intensity changes resulting from increasing analyte concentrations, in both HAB and HB, for both ATP and adenosine analytes can be seen in Figure 6b. The baseline fluorescence intensity F_0 of the sensor with HB is around 4-fold higher ($F_{0\text{ HB}} \approx 11 \times 10^3$ cps and $F_{0\text{ HAB}} \approx 3 \times 10^3$ cps); nevertheless the assay can be seen to perform similarly in terms of dynamic range for the detection of adenosine in both buffers. However, for ATP detection, saturation of sensor response is reached earlier in HB at 2 mM ATP, which is in contrast to 12 mM ATP for HAB and the peak intensity in HB is lower than for HAB. This decreased signal to background ratio and higher F_0 can be attributed to the influence of high salt concentration in HB, that leads to an analyte-free folded aptamer conformation and consequently lower structural change in the ATP bound state.

CONCLUSIONS

A DNA aptamer sequence specific to ATP was utilized in a plasmon field-enhanced reversible assay based on fluorescence energy transfer. The presented work demonstrates that the reversible interaction of a fluorophore-labeled aptamer with low-molecular-weight target analytes—adenosine and ATP—can be sensitively monitored in real time by plasmon field-enhanced fluorescence light intensity. The optical simulations qualitatively agree with the measured dependence of fluorescence light intensity on conformational changes of the used aptamers and they allowed ascribing the observed effects to variations in the fluorophore orientation and distance from the surface controlled by the molecular spacers. The plasmon field-enhanced fluorescence is shown to offer the advantage of continuous probing of aptamer capturing the target analyte for more than 1 h without bleaching of the dye, with a limit of detection of 1 μM . The observed design rules may provide leads to prepare more sensitive and robust assays that take advantage of versatile aptamer recognition elements and coupling with the confined field of surface plasmons in various optical configurations.

ASSOCIATED CONTENT

Supporting Information

The Supporting Information is available free of charge on the ACS Publications website at DOI: 10.1021/acssensors.7b00131.

Summary of estimated distances between fluorophore and metallic surface for open and closed aptamer conformations, figures depicting the dihedral angle scan for SLA and LLA, fluorescence signal kinetics upon SLA interaction with ATP and adenosine, and fitting of calibration curves with Langmuir isotherm model in

order to determine equilibrium dissociation constant (PDF)

AUTHOR INFORMATION

Corresponding Author

*E-mail: jakub.dostalek@ait.ac.at.

ORCID

Chris Oostenbrink: 0000-0002-4232-2556

Bo Liedberg: 0000-0003-2883-6953

Jakub Dostálek: 0000-0002-0431-2170

Notes

The authors declare no competing financial interest.

ACKNOWLEDGMENTS

K.S. acknowledges financial support from the Austrian Federal Ministry for Transport, Innovation and Technology (GZ BMVIT-612.166/0001-III/11/2010). J.D. received support from the Tan Chin Tuan foundation, College of Engineering, Nanyang Technological University. A.T. acknowledges the Ph.D. program “BioTop - Biomolecular Technology of Proteins” (Austrian Science Fund, FWF Project W1224).

REFERENCES

- (1) Bauch, M.; Toma, K.; Toma, M.; Zhang, Q.; Dostalek, J. Plasmon-Enhanced Fluorescence Biosensors: a Review. *Plasmonics* **2014**, *9* (4), 781–799.
- (2) Lakowicz, J. R.; Ray, K.; Chowdhury, M.; Szmajcinski, H.; Fu, Y.; Zhang, J.; Nowaczyk, K. Plasmon-Controlled Fluorescence: A New Paradigm in Fluorescence Spectroscopy. *Analyst* **2008**, *133* (10), 1308–1346.
- (3) Khatua, S.; Paulo, P. M. R.; Yuan, H.; Gupta, A.; Zijlstra, P.; Orrit, M. Resonant Plasmonic Enhancement of Single-Molecule Fluorescence by Individual Gold Nanorods. *ACS Nano* **2014**, *8* (5), 4440–4449.
- (4) Attridge, J. W.; Daniels, P. B.; Deacon, J. K.; Robinson, G. A.; Davidson, G. P. Sensitivity Enhancement of Optical Immunosensors by the Use of a Surface Plasmon Resonance Fluoroimmunoassay. *Biosens. Bioelectron.* **1991**, *6* (3), 201–214.
- (5) Liebermann, T.; Knoll, W. Surface-Plasmon Field-Enhanced Fluorescence Spectroscopy. *Colloids Surf., A* **2000**, *171* (1–3), 115–130.
- (6) Kinkhabwala, A.; Yu, Z.; Fan, S.; Avlasevich, Y.; Mullen, K.; Moerner, W. E. Large Single-Molecule Fluorescence Enhancements Produced by a Bowtie Nanoantenna. *Nat. Photonics* **2009**, *3* (11), 654–657.
- (7) Anger, P.; Bharadwaj, P.; Novotny, L. Enhancement and Quenching of Single-Molecule Fluorescence. *Phys. Rev. Lett.* **2006**, *96* (11), 4.
- (8) Bharadwaj, P.; Novotny, L. Spectral Dependence of Single Molecule Fluorescence Enhancement. *Opt. Express* **2007**, *15* (21), 14266–14274.
- (9) Vasilev, K.; Knoll, W.; Kreiter, M. Fluorescence Intensities of Chromophores in Front of a Thin Metal Film. *J. Chem. Phys.* **2004**, *120* (7), 3439–3445.
- (10) Wang, R. E.; Zhang, Y.; Cai, J.; Cai, W.; Gao, T. Aptamer-Based Fluorescent Biosensors. *Curr. Med. Chem.* **2011**, *18* (27), 4175–4184.
- (11) Zhou, W.; Jimmy Huang, P.-J.; Ding, J.; Liu, J. Aptamer-Based Biosensors for Biomedical Diagnostics. *Analyst* **2014**, *139* (11), 2627–2640.
- (12) Zhang, J.; Wang, L.; Zhang, H.; Boey, F.; Song, S.; Fan, C. Aptamer-Based Multicolor Fluorescent Gold Nanoparticles for Multiplex Detection in Homogeneous Solution. *Small* **2010**, *6* (2), 201–204.
- (13) Wood, A. J.; Basuray, S.; Bok, S.; Gangopadhyay, K.; Gangopadhyay, S.; Grant, S. A. Enhanced DNA Detection Through

the Incorporation of Nanocones and Cavities Into a Plasmonic Grating Sensor Platform. *IEEE Sens. J.* **2016**, *16* (10), 3403–3408.

(14) Lee, S. E.; Chen, Q.; Bhat, R.; Petkiewicz, S.; Smith, J. M.; Ferry, V. E.; Correia, A. L.; Alivisatos, A. P.; Bissell, M. J. Reversible Aptamer-Au Plasmon Rulers for Secreted Single Molecules. *Nano Lett.* **2015**, *15* (7), 4564–4570.

(15) Wang, W.; Chen, C.; Qian, M.; Zhao, X. S. Aptamer biosensor for protein detection using gold nanoparticles. *Anal. Biochem.* **2008**, *373* (2), 213–219.

(16) Melaine, F.; Roupioz, Y.; Buhot, A. Gold Nanoparticles Surface Plasmon Resonance Enhanced Signal for the Detection of Small Molecules on Split-Aptamer Microarrays (Small Molecules Detection from Split-Aptamers). *Microarrays* **2015**, *4* (1), 41.

(17) Wu, C.; Yang, C. J.; Tan, W. Molecular Aptamer Beacons. In *Molecular Beacons*, Yang, C. J.; Tan, W., Eds.; Springer: Berlin, Heidelberg, 2013; pp 175–194.

(18) Sui, N.; Wang, L. N.; Xie, F. X.; Liu, F. Y.; Xiao, H. L.; Liu, M. H.; Yu, W. W. Ultrasensitive Aptamer-Based Thrombin Assay Based on Metal Enhanced Fluorescence Resonance Energy Transfer. *Microchim. Acta* **2016**, *183* (5), 1563–1570.

(19) Meng, C.; Dai, Z.; Guo, W. J.; Chu, Y. Y.; Chen, G. P. Selective and Sensitive Fluorescence Aptamer Biosensors of Adenosine Triphosphate. *Nanomater. Nanotechnol.* **2016**, *6*, 33.

(20) Xie, T. T.; Liu, Q.; Cai, W. P.; Chen, Z.; Li, Y. Q. Surface Plasmon-Coupled Directional Emission Based on a Conformational-Switching Signaling Aptamer. *Chem. Commun.* **2009**, *22*, 3190–3192.

(21) Huizenga, D. E.; Szostak, J. W. A DNA Aptamer That Binds Adenosine and ATP. *Biochemistry* **1995**, *34* (2), 656–665.

(22) Williams, M. L. CRC Handbook of Chemistry and Physics. *Occup. Environ. Med.* **1996**, *53* (7), 504.

(23) Flory, P. J.; Volkenstein, M. Statistical Mechanics of Chain Molecules. *Biopolymers* **1969**, *8* (5), 699–700.

(24) Murphy, M. C.; Rasnik, I.; Cheng, W.; Lohman, T. M.; Ha, T. Probing Single-Stranded DNA Conformational Flexibility Using Fluorescence Spectroscopy. *Biophys. J.* **2004**, *86* (4), 2530–2537.

(25) Hageneder, S.; Bauch, M.; Dostalek, J. Plasmonically Amplified Bioassay – Total Internal Reflection Fluorescence vs. Epifluorescence Geometry. *Talanta* **2016**, *156–157*, 225–231.

(26) Sarkar, D.; Somasundaran, P. Conformational Dynamics of Poly(acrylic acid). A Study Using Surface Plasmon Resonance Spectroscopy. *Langmuir* **2004**, *20* (11), 4657–4664.

(27) Xue, Q.; Wang, L.; Jiang, W. A Novel Label-Free Cascade Amplification Strategy based on Dumbbell Probe-Mediated Rolling Circle Amplification-Responsive G-Quadruplex Formation for Highly Sensitive and Selective Detection of NAD⁺ or ATP. *Chem. Commun.* **2013**, *49* (26), 2640–2642.

(28) Xu, J.; Wei, C. The Aptamer DNA-Templated Fluorescence Silver Nanoclusters: ATP Detection and Preliminary Mechanism Investigation. *Biosens. Bioelectron.* **2017**, *87*, 422–427.

(29) Ma, C.; Lin, C.; Wang, Y.; Chen, X. DNA-based ATP sensing. *TrAC, Trends Anal. Chem.* **2016**, *77*, 226–241.

(30) Perrier, S.; Bouilloud, P.; De Oliveira Coelho, G.; Henry, M.; Peyrin, E. Small Molecule Aptamer Assays based on Fluorescence Anisotropy Signal-Enhancer Oligonucleotides. *Biosens. Bioelectron.* **2016**, *82*, 155–161.

(31) Bogomolova, A.; Aldissi, M. Real-Time Aptamer Quantum Dot Fluorescent Flow Sensor. *Biosens. Bioelectron.* **2011**, *26* (10), 4099–4103.

(32) Liu, Z.; Chen, S.; Liu, B.; Wu, J.; Zhou, Y.; He, L.; Ding, J.; Liu, J. Intracellular Detection of ATP Using an Aptamer Beacon Covalently Linked to Graphene Oxide Resisting Nonspecific Probe Displacement. *Anal. Chem.* **2014**, *86* (24), 12229–12235.

(33) Cho, E. J.; Lee, J.-W.; Ellington, A. D. Applications of Aptamers as Sensors. *Annu. Rev. Anal. Chem.* **2009**, *2* (1), 241–264.

(34) Nielsen, L. J.; Olsen, L. F.; Ozalp, V. C. Aptamers Embedded in Polyacrylamide Nanoparticles: A Tool for in Vivo Metabolite Sensing. *ACS Nano* **2010**, *4* (8), 4361–4370.

(35) Xia, T.; Yuan, J.; Fang, X. Conformational Dynamics of an ATP-Binding DNA Aptamer: A Single-Molecule Study. *J. Phys. Chem. B* **2013**, *117* (48), 14994–15003.

Plasmon field-enhanced fluorescence energy transfer for hairpin aptamer assay readout

*Khulan Sergelen^{†, ‡}, Stefan Fossati[†], Aysegül Turupcu[‡], Chris Oostenbrink[‡], Bo Liedberg[‡],
Wolfgang Knoll,[†] and Jakub Dostálek^{†,*}*

[†] BioSensor Technologies, AIT-Austrian Institute of Technology, Muthgasse 11, 1190 Vienna, Austria

[‡] Nanyang Technological University, Centre for Biomimetic Sensor Science, School of Materials Science and Engineering, 50 Nanyang Drive, Singapore 637553

[‡] University of Natural Resources and Life Sciences, Institute of Molecular Modeling and Simulation, Muthgasse 18, 1190 Vienna, Austria

Table of Contents:

Table S1. Calculated possible lengths of aptamer linkers between metallic surface and Alexa Fluor 647 dye

Figure S1. Dihedral angle scan of f_{off} states for SLA and LLA

Figure S2. Fluorescence signal kinetics of SLA binding with ATP and Adenosine

Figure S3. Dissociation constants K_d of adenosine and ATP for SLA and LLA aptamers

Calculated possible lengths of aptamer linkers between metallic surface and Alexa Fluor 647 dye

		min, nm	random, nm	max, nm
SLA	f_{off}	0	0.9	4.7
	f_{on}		3.8	15.3
LLA	f_{off}	0	1.6	9.6
	f_{on}		5.7	35.5

Table S1. Summary of distance values determined for the length of aptamer linkers separating Alexa Fluor 547 dye from metallic surface in both SLA and LLA aptamers in their off f_{off} and on f_{on} states. The minimum in f_{off} set at 0 is due to the possible collapsing of the dye on the metallic surface, resulting in complete quenching. The values for random (freely rotating polymer-ssDNA stretch) was determined using the random coil model with the function $\sqrt{N} \cdot a$, where N is the polymer units and a the length between each unit. Values of a for ssDNA subunits was 0.63 nm^1 and all other bonds 0.15 nm. The value maximum is defined as $N \cdot a$, of a maximum extended polymer.

Dihedral angle scan of f_{off} states for SLA and LLA

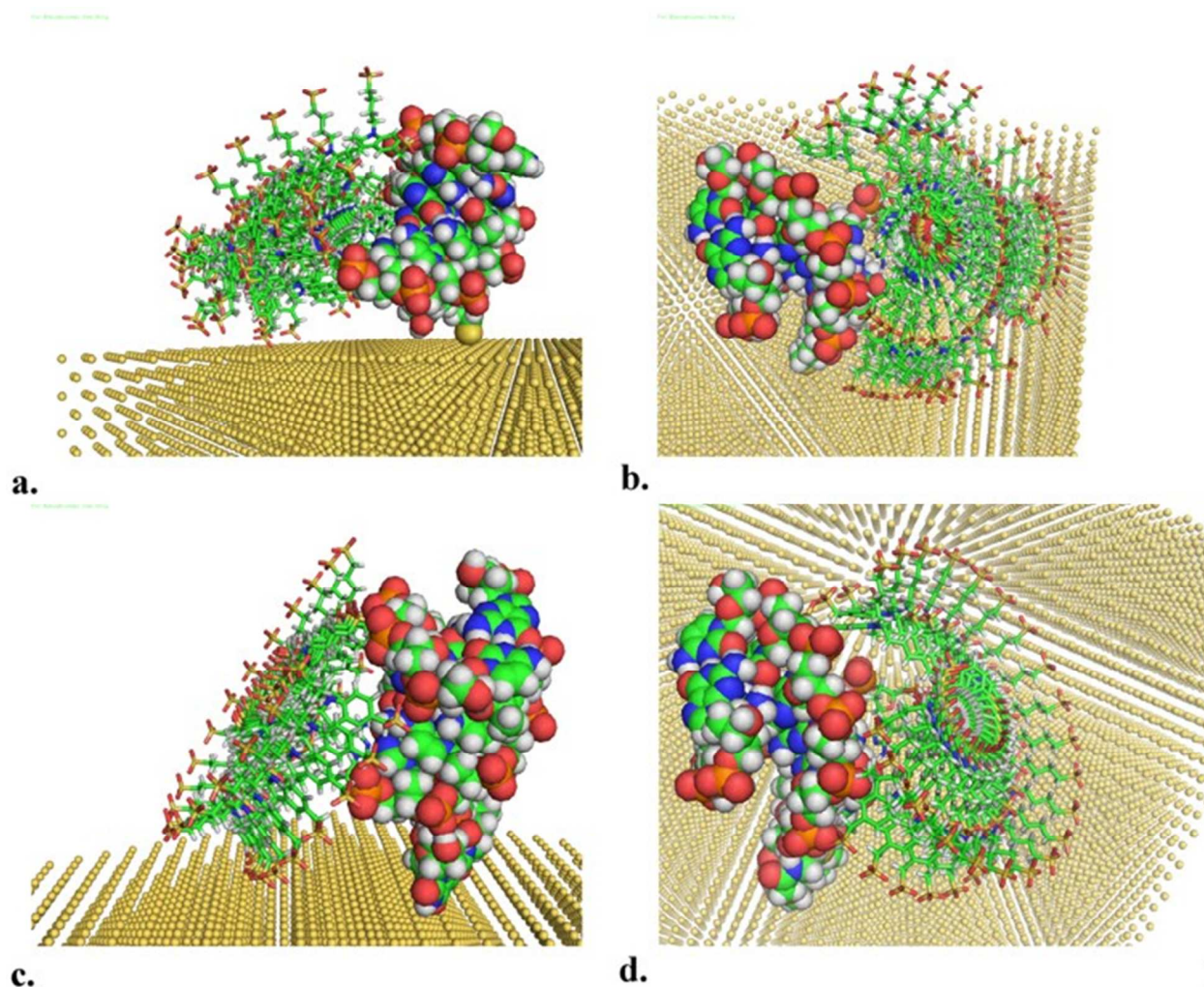


Figure S1. Dihedral scans of SLA (a. and b.) and LLA (c. and d.) aptamers in the f_{off} state. The rotational freedom of the Alexa Fluor 647 dye (sticks) attached to 5' end of complementary 14 base linker DNA (colored spheres) anchored onto a gold film (yellow spheres), is demonstrated. The Alexa Fluor 647 dye in the SLA linker shows more restricted rotational freedom, as seen in a. side view and b. top view, compared to the LLA attached dye as seen in c. side view and d. top view.

Fluorescence signal kinetics of SLA binding with ATP and Adenosine

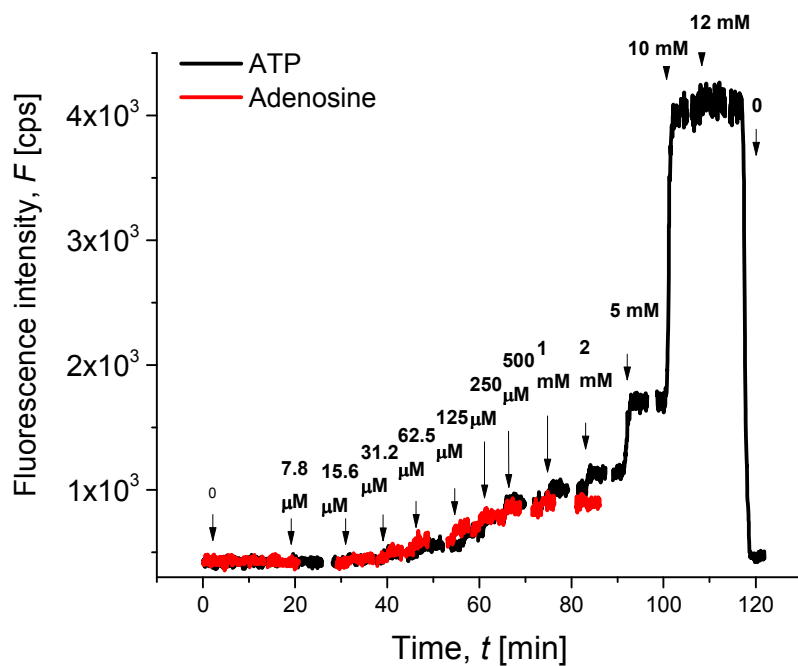
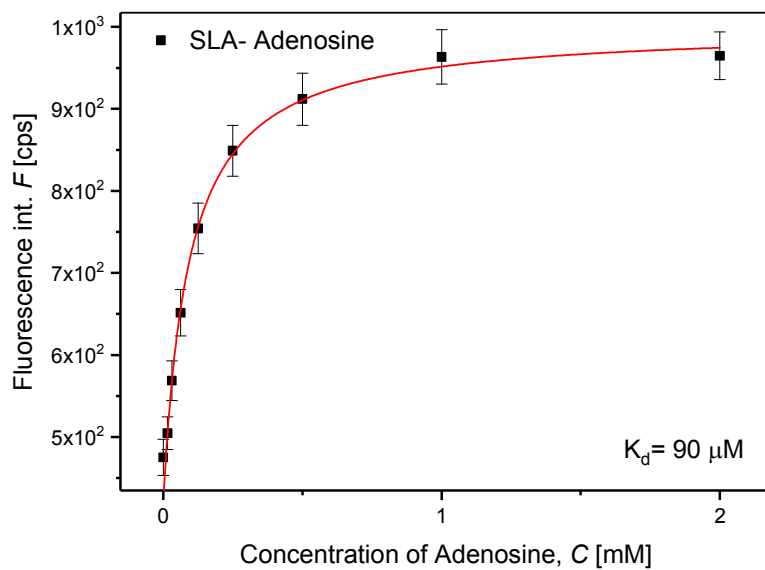
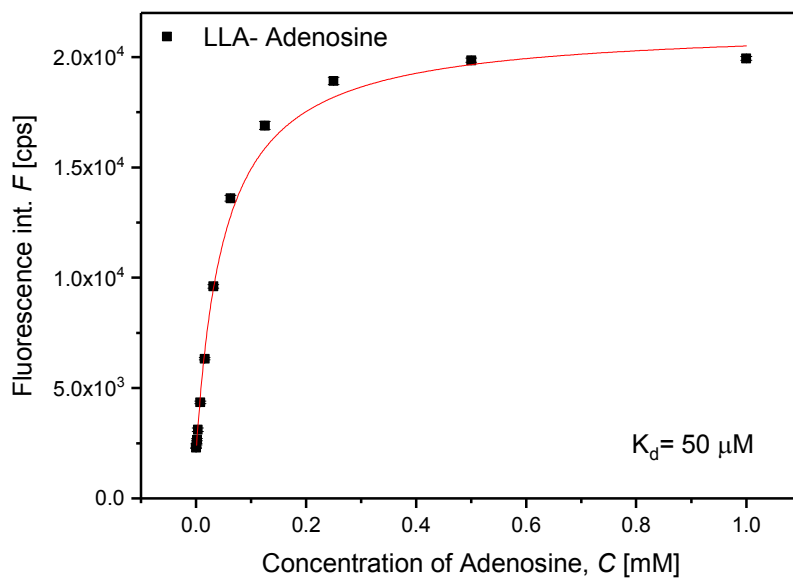


Figure S2. Real-time fluorescence signal $F(t)$ measured at a fixed angle $\theta=57$ deg upon sequential injection of ATP and adenosine at concentrations 0-12 mM in HAB buffer for gold sensor surface functionalized with SLA.

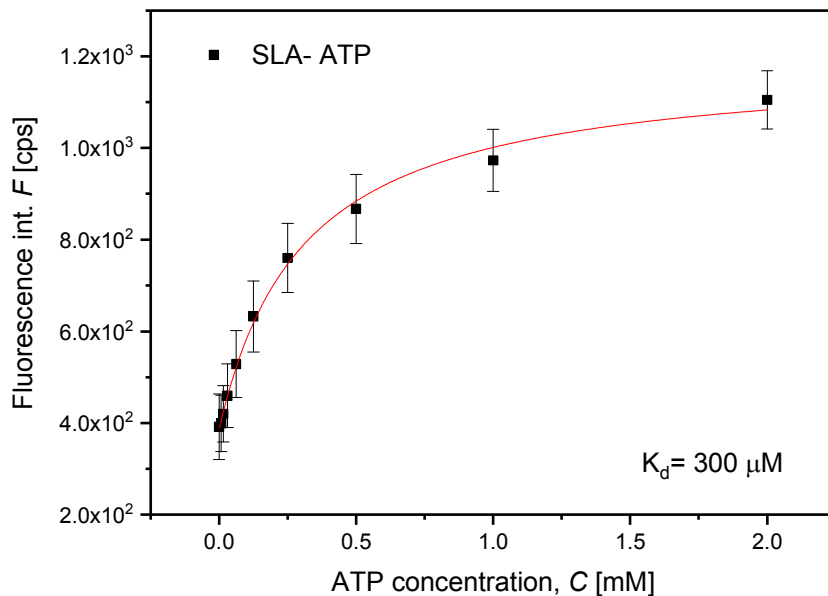
Dissociation constants K_d of adenosine and ATP for SLA and LLA aptamers



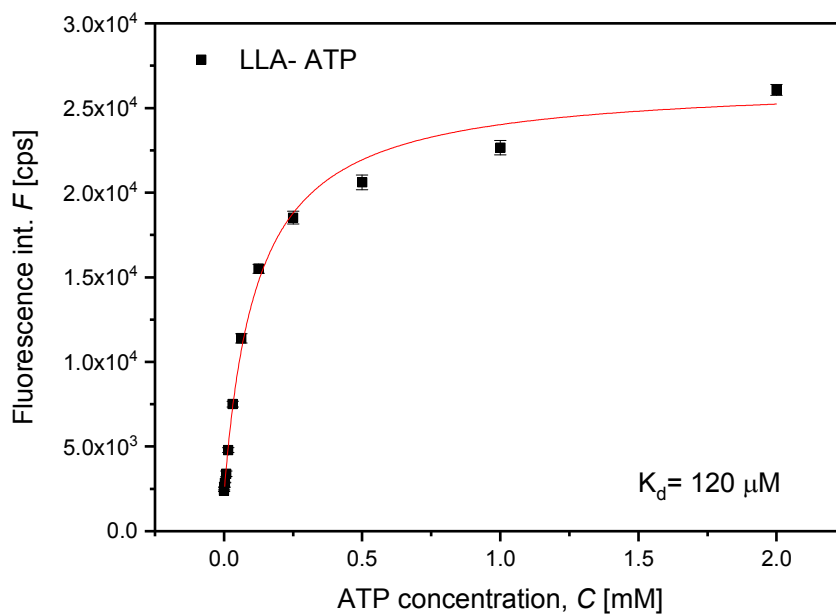
a.



b.



c.



d.

Figure S3. Calibration curves established from changes in fluorescence intensity F as a result of increasing concentrations of analytes adenosine (a. and b.) and ATP (c. and d.). Dissociation constants (K_d) are determined by fitting with Langmuir isotherm model.

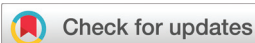
REFERENCES

1. Murphy, M. C.; Rasnik, I.; Cheng, W.; Lohman, T. M.; Ha, T. Probing Single-Stranded DNA Conformational Flexibility Using Fluorescence Spectroscopy. *Biophysical Journal* **2004**, *86* (4), 2530-2537.

5. Surface plasmon field-enhanced fluorescence reversible split aptamer biosensor

Khulan Sergelen, Bo Liedberg, Wolfgang Knoll, and Jakub Dostálek, *Analyst*, 2017, 142, 2995-3001.

DOI: 10.1039/c7an00970d



Cite this: *Analyst*, 2017, **142**, 2995

A surface plasmon field-enhanced fluorescence reversible split aptamer biosensor†

K. Sergelen,^{a,b,c} B. Liedberg,^b W. Knoll^a and J. Dostálek^{b,*a}

Surface plasmon field-enhanced fluorescence is reported for the readout of a heterogeneous assay that utilizes low affinity split aptamer ligands. Weak affinity ligands that reversibly interact with target analytes hold potential for facile implementation in continuous monitoring biosensor systems. This functionality is not possible without the regeneration of more commonly used assays relying on high affinity ligands and end-point measurement. In fluorescence-based sensors, the use of low affinity ligands allows avoiding this step but it imposes a challenge associated with the weak optical response to the specific capture of the target analyte which is also often masked by a strong background. The coupling of fluorophore labels with a confined field of surface plasmons is reported for strong amplification of the fluorescence signal emitted from the sensor surface and its efficient discrimination from the background. This optical scheme is demonstrated for time-resolved analysis of chosen model analytes – adenoside and adenosine triphosphate – with a split aptamer that exhibits an equilibrium affinity binding constant between 0.73 and 1.35 mM. The developed biosensor enables rapid and specific discrimination of target analyte concentration changes from low μM to mM in buffer as well as in 10% serum.

Received 10th June 2017,
Accepted 6th July 2017

DOI: 10.1039/c7an00970d

rs.c.li/analyst

Introduction

In recent years, a rapidly increasing number of analytical technologies have taken advantage of cost-effective production and flexibility in the design of oligonucleic acid aptamer ligands.^{1–3} Among others, aptamer biosensors found their applications in sensitive analysis of species that serve as biomarkers of cancer,^{4–6} cardiovascular diseases,^{7,8} and inflammation^{9–11} as well as for the detection of pathogens.^{3,12,13} The optical readout of the specific interaction of an aptamer ligand with a target analyte mostly utilizes fluorescence.^{14–16} The majority of fluorescence-based aptamer biosensors rely on distance-dependent fluorescence resonance energy transfer (FRET)^{17,18} or quenching of the fluorescence signal in the vicinity of graphene^{13,19,20} and other quenchers.^{21,22} The performance of fluorescence-based biosensors is

often limited by the background signal and bleaching of fluorophore labels. This problem may be overcome by the use of surface plasmon resonance (SPR) biosensors which provide a facile platform for the direct detection of a target analyte that does not require labels.^{23–25} SPR aptamer biosensors exploiting localized surface plasmons supported by metallic nanoparticles^{12,26,27} and propagating surface plasmons travelling along thin metallic films¹¹ were reported. Moreover, surface plasmon optics can be employed for the amplification of the fluorescence assay readout by probing of aptamer binding with plasmonically enhanced intensity of the electromagnetic field. This phenomenon was exploited with the use of propagating surface plasmons on metallic surfaces^{28–31} as well as with localized surface plasmons supported by metallic nanoparticles spiked to the analyzed liquid sample.^{32,33} Besides the plasmon-enhanced fluorescence (PEF) intensity, this detection scheme typically decreases the lifetime of the used fluorophore labels which reduces the effect of bleaching.^{34,35}

The sandwich format is routinely used in immunoassays for the detection of medium and large molecular weight analytes. In this method, one antibody is attached to a sensor surface to capture the target analyte from the analyzed sample. Subsequently, the surface is reacted with the second antibody that is labeled with a reporter (e.g. fluorophore or nanoparticle).³⁶ These two antibodies are designed so that they bind to different epitopes of the target analyte without steric hindrance. This approach is generally not possible for low

^aBioSensor Technologies, AIT-Austrian Institute of Technology, Muthgasse 11, 1190 Vienna, Austria. E-mail: jakub.dostalek@ait.ac.at; Fax: +43 50550-4450; Tel: +43 50550 4470

^bNanyang Technological University, Centre for Biomimetic Sensor Science, School of Materials Science and Engineering, 50 Nanyang Drive, Singapore 637553

^cInternational Graduate School on Bionanotechnology, University of Natural Resources and Life Sciences, Austrian Institute of Technology (Austria) and Nanyang Technological University (Singapore)

† Electronic supplementary information (ESI) available: Surface mass density values of the functionalized sensor chip and fitted calibration curves of each of the target analytes with determined dissociation constants. See DOI: 10.1039/c7an00970d

molecular weight analytes. Aptamers on the other hand provide an interesting alternative to established immunoassays and they are particularly attractive for rapid detection of low molecular-weight analytes.^{10,17,18,26} Single strand oligonucleotide aptamers were also implemented in biosensors utilizing a sandwich assay.^{37–39} In contrast to immunoassays, they offer means to design sandwich-type assays even for low molecular weight analytes^{40–44} by using an aptamer sequence divided into two separate strands in a way that allows maintaining the binding activity.

The sandwich aptamer assay was utilized for continuous sensing of biologically active analytes⁴⁵ which was reported for time-resolved measurements of species secreted by cells to their local environment. Indeed, the vast majority of biosensors rely on high affinity ligands. Then regeneration protocols need to be applied to strip the captured analyte from the ligand for their repeated use.^{46,47} However, such regeneration complicates the operation in emerging applications such as cell-on-chip⁴⁸ or therapeutic drug monitoring.⁴⁹ In principle, more facile monitoring of time dependent analyte concentration variations can be utilized by low affinity ligands.^{50–53} In sandwich aptamer assays that utilize SPR metallic nanoparticles as reporters, usually multiple aptamer (oligonucleotide) strands are attached which often leads to avidity-enhanced irreversible interactions with the analyte. This can be overcome by tedious purification steps⁴⁵ or with the use of fluorophore tags that do not increase affinity.⁵⁴

The use of weak affinity ligands for reversible fluorescence-based sandwich assaying is challenging due to the high fluorescence background and weak specific signals associated with the analyte capture. We report herein the implementation of PEF as a sensitive readout method for reversible split aptamer-based fluorescence biosensing. A split DNA aptamer^{55,56} that binds to ATP and adenosine was chosen for a proof of concept demonstration of real-time continuous monitoring of concentration changes without the need of regeneration.

Experimental

Materials

Adenosine 5'-triphosphate disodium salt hydrate (ATP), adenosine, guanosine, sodium chloride, magnesium chloride hexahydrate, tris hydrochloride, 4-(2-hydroxyethyl)piperazine-1-ethanesulfonic acid (HEPES) and polyethylene glycol sorbitan monolaurate (TWEEN 20) were obtained from Sigma-Aldrich (Austria). Neutravidin protein was purchased from ThermoFisher (Austria). Biotinylated alkane PEG thiol (BA thiol, SPT-0012D) and (11-mercaptoundecyl) triethyleneglycol (PEG thiol, SPT-0011) were purchased from SensoPath Technologies Inc. (USA). Buffer solutions were prepared using ultrapure water (arium pro, Sartorius Stedim) with all reagents used as received. The ATP and adenosine binding split DNA aptamer⁵⁵ sequences Biotin 5'-TTTTTTTTTTTGA GAA CCT GGG GGA GTA T-3' (segment S1-Biotin) and AlexaFluor647N 5'-TTTTTTGC GGA GGA AGG TAG AG-3' (segment S2-AF647) were synthesized by Integrated DNA Technologies (Belgium). The

serum sample was collected from a healthy donor using a Vacuette Z Serum Clot Activator (Freiner Bio One, Germany), centrifuged for 10 minutes at 1800g and stored at -20°C until analysis.

Sensor chip preparation

Sensor chips were prepared on BK7 glass substrates which were subsequently coated with 2 nm chromium and 50 nm gold films by thermal vacuum evaporation (HHV Auto306 Lab Coater). The thickness of gold was chosen to maximize the coupling strength to propagating surface plasmons based on previous work reported in the literature.⁵⁷ The gold surfaces were rinsed with ethanol, dried under a stream of air and immersed in 1 mM ethanolic solution with BA and PEG thiols dissolved at a 1:9 ratio. This ratio was reported as optimum for the immobilization of oligonucleotide strands by streptavidin-biotin interactions.⁵⁸ After 48 hours of incubation under an argon atmosphere, a mixed self-assembled monolayer (SAM) was formed on the gold surface which was subsequently rinsed with ethanol and dried under a stream of air. A 10 mM HEPES buffer (pH = 7.4) containing 150 mM NaCl, 5 mM MgCl₂ and 0.005% Tween 20 was used throughout the immobilization of the ligand. Initially, 0.5 mL of 50 $\mu\text{g mL}^{-1}$ neutravidin solution was flowed over the mixed thiol SAM for 25 minutes to form a monolayer.⁵⁷ Then, 0.5 mL of 1 μM solution of biotinylated split aptamer segment 1 (S1-Biotin) was reacted with the surface for 25 minutes in which the saturation was reached. After each incubation step, the sensor surface was rinsed for 10 minutes with buffer.

Optical measurements

For the optical measurements, an instrument that combines surface plasmon resonance (SPR) and surface plasmon field-enhanced fluorescence (PEF) was used as described previously.⁵⁹ Briefly, the sensor chip with the mixed thiol SAM was optically matched to an LASFN9 glass prism with refractive index matching oil (Cargille Inc., USA) and a flow-cell was clamped onto its top. The volume of the flow-cell was 10 μL and it consisted of a PDMS gasket (thickness of $\sim 130\ \mu\text{m}$) and a transparent glass substrate with drilled inlet and outlet ports. Liquid samples were transported *via* a tubing (Tygon LMT-55) with a 0.25 mm inner diameter at a flow rate of 15 $\mu\text{L min}^{-1}$. This assembly was mounted onto a rotating stage and a monochromatic transverse magnetically (TM) polarized HeNe laser ($\lambda_{\text{ex}} = 632.8\ \text{nm}$) beam was coupled to the prism. The angle of incidence θ was controlled to resonantly excite the propagating surface plasmons (PSPs) on the gold surface by the Kretschmann configuration of the attenuated total reflection method. The reflected light intensity R was measured by using a photodiode detector connected to a lock-in amplifier (EG&G, USA). In addition, the fluorescence intensity F emitted at wavelength $\lambda_{\text{em}} = 670\ \text{nm}$ through the flow-cell in the direction normal to the gold surface was collected with a lens (focal length 30 mm, numerical aperture NA = 0.2). Two bandpass filters (transmission wavelength $\lambda_{\text{em}} = 670\ \text{nm}$, 670FS10-25, Andover Corporation Optical Filter, USA) and a notch filter

(central stop-band wavelength $\lambda_{\text{ex}} = 632.8$ nm, XNF-632.8-25.0 M, CVI Melles Griot, USA) were used to block the excitation light at λ_{ex} . Afterwards, the beam at λ_{em} was coupled to a multi-mode optical fiber (FT400EMT, Thorlabs, UK) and detected with an avalanche photodiode (Count-200-FC, Laser Components, Germany). The fluorescence light intensity F was measured using a counter (53131A, Agilent, USA) in counts per second (cps). Both the reflectivity and fluorescence signals were recorded using the software Wasplas (Max Planck Institute for Polymer Research, Mainz, Germany). Time resolved measurements of reflectivity R and fluorescence intensity F were performed at a fixed incidence angle θ .

Split aptamer assay

In the split aptamer assay, the HEPES buffer solution with 100 nM S2-AF647 aptamer (concentration derived from data shown in Fig. S2†) was continuously flowed over the sensor surface with immobilized aptamer S1-Biotin. After establishing a stable baseline in the acquired fluorescence signal F_0 in about 15 minutes, sequential analysis of samples with the target (ATP, adenosine) and reference (guanosine) analytes was performed. These analytes were spiked into the buffer with 100 nM S2-AF647 and each sample was allowed to react with the surface for 5–8 minutes until a steady level of fluorescence signal $F(t)$ was reached.

Results and discussion

Surface plasmon field-enhanced fluorescence split aptamer assay

As can be seen in Fig. 1, the used split aptamer ligand is composed of two segments. The segment S1-Biotin was immobi-

lized on the sensor surface by using the biotin tag, while the second segment S2-AF647 carrying Alexa Fluor 647 label was contained in a solution above the surface. Split aptamer sequences that specifically bind to adenosine and ATP were adopted from studies reported in the literature.^{55,56} In the presence of the target analyte, the segment S2-AF647 forms a complex with tethered S1-Biotin, whereas in the absence of the target analyte the segments do not interact. The S2-AF647 binding events triggered by the presence of the target analyte were monitored by probing of the gold sensor surface with resonantly excited surface plasmons – PSPs. The excitation of PSPs generates an increased intensity of electromagnetic field at a wavelength of $\lambda_{\text{ex}} = 633$ nm which coincides with the absorption band of the used fluorophore. Due to its confined field profile, the PSP-enhanced excitation of fluorophores occurs only in the close proximity of the sensor surface (below <100 nm). The fluorescence light intensity F that was emitted perpendicularly to the surface at a wavelength of $\lambda_{\text{em}} = 670$ nm was collected and detected in time.

The intensity of the emitted fluorescence signal is strongly dependent on the distance of the fluorophore from the gold surface.²⁹ In order to prevent quenching occurring at short distances of <10 nm, surface architecture with a neutravidin spacer layer was used for the immobilization of the S1-Biotin segment. Then the affinity binding occurs further away from the gold and the effect of quenching is substantially reduced as reported previously for the surface plasmon-enhanced fluorescence detection of DNA hybridization.⁶⁰

Aqueous samples with varying concentrations of ATP were prepared. Each sample was spiked with the same concentration of aptamer segment S2-AF647 of 100 nM and flowed over the sensor surface for 5–8 min. Upon the flow of samples, a series of fluorescence intensity scans $F(\theta)$ were measured for different angles of incidence θ of the excitation laser beam at λ_{ex} . As shown in Fig. 2, strong fluorescence intensity F was

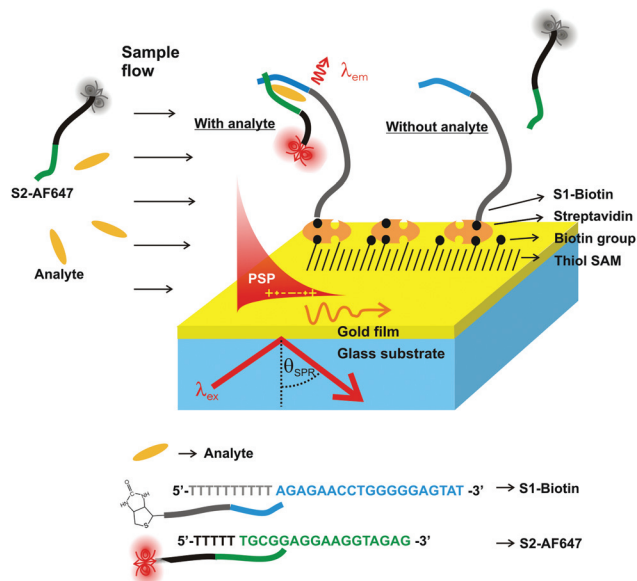


Fig. 1 Schematics of the split aptamer sandwich assay and surface architecture.

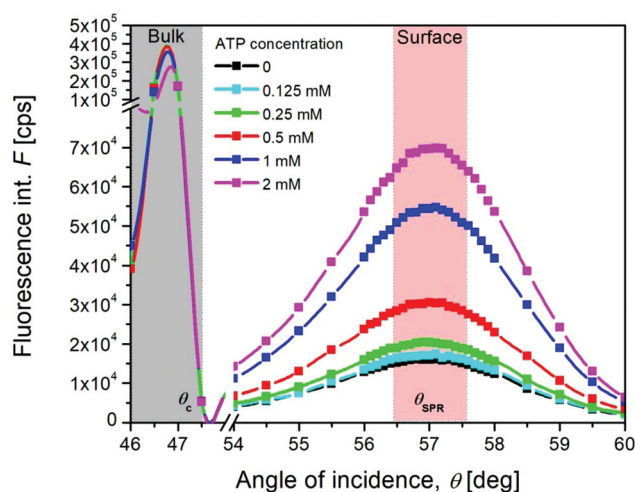


Fig. 2 Angular fluorescence intensity spectra $F(\theta)$ measured upon the affinity binding of ATP to the sensor surface from samples with ATP concentration from 0.125 to 2 mM.

observed at angles θ below the critical angle ($\theta_c = 47.3$ deg). This fluorescence signal originates from fluorophores dispersed in the bulk solution that are excited with a laser beam partially transmitted through the gold layer. When increasing the angle θ above the critical angle θ_c , the fluorescence signal F drops and an additional fluorescence peak is observed at a higher angle $\theta_{\text{SPR}} \sim 57$ deg. This peak is ascribed to the fluorescence signal emitted from the surface when PSPs are resonantly excited at λ_{ex} . Interestingly, when increasing the concentration of ATP in the solution, the fluorescence signal below the critical angle θ_c does not significantly change. In contrast, probing of the sensor surface with the confined field of PSPs at angle θ_{SPR} is accompanied by fluorescence intensity that increases with ATP concentration. The reason is that below the critical angle θ_c the measured fluorescence signal F mostly originates from the fluorophore labeled segment of the aptamer S2-AF647 that is contained in the bulk solution. This signal apparently masks the response due to the affinity binding on the sensor surface. However, above the critical angle θ_c the fluorescence excitation *via* the enhanced intensity of the evanescent PSP field occurs. Such optical enhancement is selective for the surface and efficiently makes the affinity binding of the target analyte distinguishable from the bulk. The simultaneously measured angular reflectivity spectra $R(\theta)$ (Fig. S3†) reveal no measurable shift in the SPR angle (represented as a minimum of the respective reflectivity dip) as the local refractive index variations associated with low molecular weight analyte binding are too weak.

Time-resolved fluorescence readout

In order to measure the fluorescence response upon the affinity binding of the target analyte in time, the angle of incidence was fixed at $\theta = 57$ deg where the strongest fluorescence enhancement was observed. Firstly, a steady baseline in the fluorescence signal F_0 was established for a flow of a blank sample with 100 nM S2-AF647. Then, a series of samples

spiked with the target analytes (ATP or adenosine) and the reference analyte (guanosine) were sequentially injected. Increasing the concentration of adenosine leads to a gradual increase of the fluorescence signal F which saturates in about 5–8 min (see Fig. 3, left). For the highest injected ATP concentration of 2 mM, the equilibrium fluorescence signal F increased by a factor of ~ 4 with respect to the baseline F_0 . For the ATP concentrations above 2 mM, the fluorescence signal reached saturation. Compared to ATP, the binding of adenosine showed a stronger response and for the concentration of 5 mM the fluorescence signal increased by a factor of ~ 22 with respect to F_0 , reaching saturation. This observation can be ascribed to differences in the interaction of ATP and adenosine with the split DNA aptamer. Possibly the weaker association of ATP with the aptamer complex than that of adenosine can be attributed to the strong negative charges of both ATP and the fluorophore AF647 conjugated split aptamer segment S2-AF647. The reference analyte guanosine did not interact with the selected aptamer.

Importantly, the interaction of the split aptamer with the target analytes is fully reversible. When switching the flow of samples to a blank buffer sample with the same concentration of S2-AF647, but without the target analyte, the fluorescence signal quickly drops to the original baseline F_0 in 1 minute. The right panel in Fig. 3 confirms the full reversibility of the assay and demonstrates the potential for real-time continuous sensing by running several cycles of injection of the sample series with increasing ATP concentration. In the context of applying such a sensor for therapeutic drug monitoring, there would be a need to reach time resolution that is comparable to the drug half-life (mostly hours to days) or time to reach the peak concentration of the drug (30 min to >hours).^{61–64} The presented assay offers a much faster response as the sensor signal reaches equilibrium in several minutes after a change of the target analyte concentration. Indeed, it should be mentioned that the response time is probably dictated by diffusion

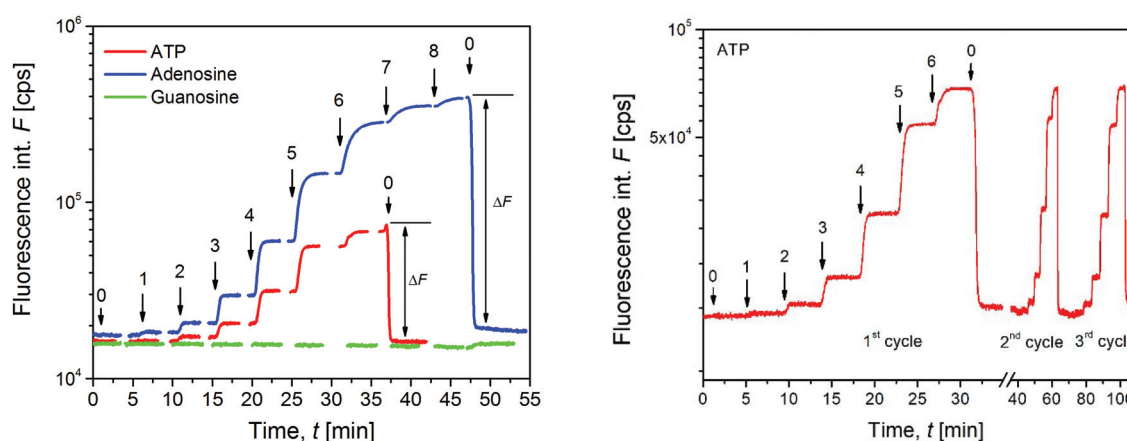


Fig. 3 The titration measurements illustrating the reversibility of the split aptamer based assay. Left. The red and blue lines indicate the specific analytes ATP and adenosine, respectively, and guanosine as the negative control (green line). Right. Demonstration of the reversible and reproducible detection of the assay for 3 rounds of ATP detection. Concentrations of analytes are indicated in sequential numbers: 0 – 0; 1 – 0.062 mM; 2 – 0.125 mM; 3 – 0.25 mM; 4 – 0.5 mM; 5 – 1 mM; 6 – 2 mM; 7 – 3 mM; 8 – 5 mM, respectively.

of the analyte to the surface and mixing of solutions in the used flow injection.

Calibration curves

From the titration experiments presented in Fig. 3, the equilibrium response was determined for each concentration as the difference of equilibrium signals $\Delta F = F - F_0$. The established calibration curves for ATP and adenosine are presented in Fig. 4 together with a fit using the Langmuir isotherm. From these data, the equilibrium dissociation constant K_d for the affinity interaction of ATP and adenosine with the split aptamer was determined. This parameter was obtained as the half saturation concentration and it yields a K_d of 0.35 mM and 1.35 mM for ATP and adenosine, respectively (Fig. S4†). It is worth noting that these values are in the range proposed for reversible continuous sensing, $K_d > \mu\text{M}$.⁵⁰ In addition, they are about two orders of magnitude higher than those for the affinity interaction with the native (not split) aptamer in the bulk solution, $K_d \sim 6 \mu\text{M}$.⁵⁶ The weaker affinity with respect to the reported heterogeneous assay can be partially attributed to the labeling of aptamer strands with fluorophores which was observed before ($K_d = 273 \mu\text{M}$ ⁵⁴).

The limit of detection for the assay was determined for each calibration curve as the concentration at which the value of 3 times the standard deviation of the background signal F_0 ($3\sigma = 2.5\%$ of F_0 for ATP and $3\sigma = 2\%$ of F_0 for adenosine) intersects with the fitted calibration curve. The LOD values of $78 \mu\text{M}$ and $42 \mu\text{M}$ were determined for ATP and adenosine, respectively. Such a detection limit is not sufficient for the analysis of ATP or adenosine as a biomarker in clinical samples such as plasma⁶⁵ or extracellular space⁶⁶ where they are present at concentrations in the low nM range. However, it may be feasible to apply a similar split aptamer for the sensing

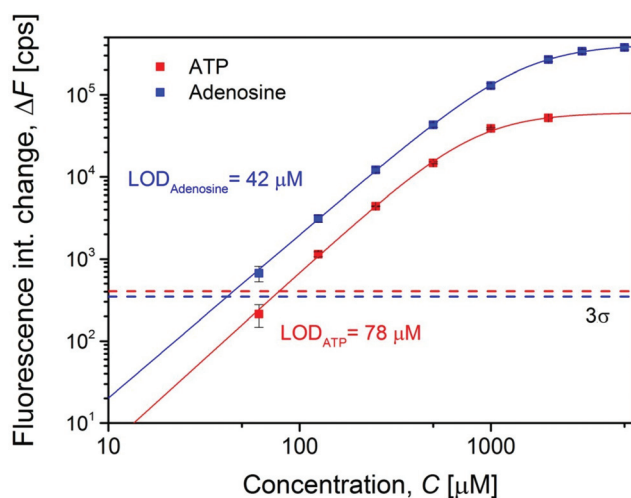


Fig. 4 Calibration curves of the detection of ATP and adenosine analytes. Each data point (ΔF) is derived from triplicate titration measurements as in Fig. 3. Calibration curves were fitted with the Langmuir isotherm model.

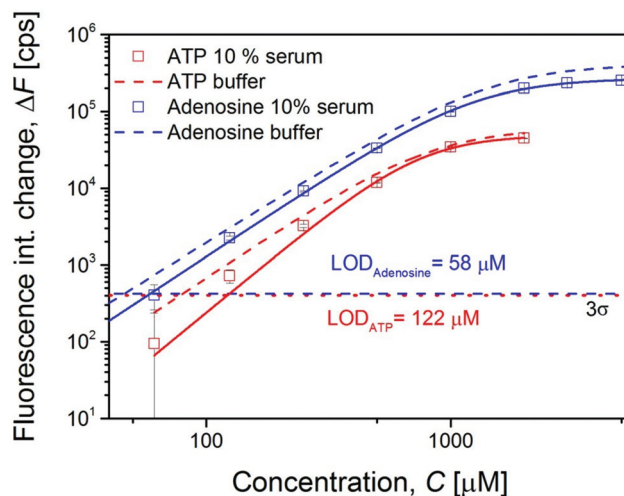


Fig. 5 Comparison of the calibration curves of ATP and adenosine detection measurements in buffer and 10% serum.

of the cellular sub mM levels of ATP⁶⁷ in cell-on-chip systems that are combined with fluorescence microscopy.⁶⁸ Plasmonic amplification of the fluorescence signal in such a detection scheme can be implemented with the use of an epifluorescence readout as reported before by our group.²⁸ In addition, the limit of detection can be improved by using more powerful plasmonic amplification schemes⁶⁹ and by using biointerfaces that accommodate higher amounts of ligands such as those relying on 3D hydrogel matrices.⁷⁰ Moreover, depending on the needed time resolution in the monitoring of target analyte concentration changes, the implementation of ligands with higher affinity would directly translate to an improved LOD.

Assay performance in real samples

Finally, the performed split aptamer assay was tested for the analyte spiked into 10% serum with the same concentration ranges as used for sensing in buffer. Detection was performed in triplicate and from the obtained calibration curves, the LOD of the sensor in 10% serum is slightly increased to $122 \mu\text{M}$ for ATP and $58 \mu\text{M}$ for adenosine (Fig. 5). Although there is slight loss in the LOD of the reported assay in diluted serum, the reversible detection of analytes is retained (Fig. S5†) and the overall biosensor performance is comparable to that in buffer.

Conclusions

A DNA split aptamer assay with a surface plasmon field-enhanced fluorescence sensor was demonstrated to allow for reversible and label-free detection of small molecular weight analytes, ATP and adenosine. Real-time probing of the analyte/aptamer specific interaction with the spatially confined surface plasmon field enabled the efficient suppression of the effect of the fluorescence background. A fully reversible

aptamer biosensor with a detection limit in the low micromolar range was established. The applicability of the sensor scheme was proven for 10-fold diluted serum and the reversible detection of concentration changes of the analytes was possible in the time range of minutes. The reported reversible sensing scheme can pave a way for the future development of continuous optical sensors for the many medically relevant markers that require close monitoring, which is vital to the improved evaluation and treatment of patient states⁷¹ or it may find its application in lab-on-chip systems for the rapid monitoring of cellular constituents and metabolites over time.⁴⁸

Acknowledgements

K. S. acknowledges financial support from the Austrian Federal Ministry for Transport, Innovation and Technology (GZ BMVIT-612.166/0001-III/11/2010). J. D. received support from the Tan Chin Tuan foundation, College of Engineering, Nanyang Technological University.

References

- 1 S. Amaya-González, N. de-los-Santos-Álvarez, A. Miranda-Ordieres and M. Lobo-Castañón, *Sensors*, 2013, **13**, 16292.
- 2 K. L. Hong and L. J. Sooter, *BioMed Res. Int.*, 2015, **2015**, 31.
- 3 E. Torres-Chavolla and E. C. Alocilja, *Biosens. Bioelectron.*, 2009, **24**, 3175–3182.
- 4 M. Jarczewska, L. Kekedy-Nagy, J. S. Nielsen, R. Campos, J. Kjems, E. Malinowska and E. E. Ferapontova, *Analyst*, 2015, **140**, 3794–3802.
- 5 X. Wu, J. Chen, M. Wu and J. X. J. Zhao, *Theranostics*, 2015, **5**, 322–344.
- 6 H. Yoochan, L. Eugene, K. Minhee, S. Jin-Suck, Y. Dae Sung and Y. Jaemoon, *Nanotechnology*, 2016, **27**, 185103.
- 7 B. Deng, Y. Lin, C. Wang, F. Li, Z. Wang, H. Zhang, X.-F. Li and X. C. Le, *Anal. Chim. Acta*, 2014, **837**, 1–15.
- 8 Q. Wang, W. Liu, Y. Xing, X. Yang, K. Wang, R. Jiang, P. Wang and Q. Zhao, *Anal. Chem.*, 2014, **86**, 6572–6579.
- 9 J. Hwang, Y. Seo, Y. Jo, J. Son and J. Choi, *Sci. Rep.*, 2016, **6**, 34778.
- 10 M. McKeague, A. Foster, Y. Miguel, A. Giamberardino, C. Verdin, J. Y. S. Chan and M. C. DeRosa, *RSC Adv.*, 2013, **3**, 24415–24422.
- 11 X. Yang, Y. Wang, K. Wang, Q. Wang, P. Wang, M. Lin, N. Chen and Y. Tan, *RSC Adv.*, 2014, **4**, 30934–30937.
- 12 H.-J. Zhang, Y.-H. Lu, Y.-J. Long, Q.-L. Wang, X.-X. Huang, R. Zhu, X.-L. Wang, L.-P. Liang, P. Teng and H.-Z. Zheng, *Anal. Methods*, 2014, **6**, 2982–2987.
- 13 P. Zuo, X. Li, D. C. Dominguez and B.-C. Ye, *Lab Chip*, 2013, **13**, 3921–3928.
- 14 B. Jin, S. Wang, M. Lin, Y. Jin, S. Zhang, X. Cui, Y. Gong, A. Li, F. Xu and T. J. Lu, *Biosens. Bioelectron.*, 2017, **90**, 525–533.
- 15 D. Lu, L. He, G. Zhang, A. Lv, R. Wang, X. Zhang and W. Tan, *Nanophotonics*, 2017, **6**(1), 109–121.
- 16 R. E. Wang, Y. Zhang, J. Cai, W. Cai and T. Gao, *Curr. Med. Chem.*, 2011, **18**, 4175–4184.
- 17 N. Duan, H. Zhang, Y. Nie, S. Wu, T. Miao, J. Chen and Z. Wang, *Anal. Methods*, 2015, **7**, 5186–5192.
- 18 C. Meng, Z. Dai, W. Guo, Y. Chu and G. Chen, *Nanomater. Nanotechnol.*, 2016, **6**, 33.
- 19 B. Esteban-Fernández de Ávila, M. A. Lopez-Ramirez, D. F. Báez, A. Jodra, V. V. Singh, K. Kaufmann and J. Wang, *ACS Sens.*, 2016, **1**, 217–221.
- 20 L. Gao, Q. Li, R. Li, L. Yan, Y. Zhou, K. Chen and H. Shi, *Nanoscale*, 2015, **7**, 10903–10907.
- 21 N. Duan, W. Gong, Z. Wang and S. Wu, *Anal. Methods*, 2016, **8**, 1390–1395.
- 22 P. Singh, R. Gupta, M. Sinha, R. Kumar and V. Bhalla, *Microchim. Acta*, 2016, **183**, 1501–1506.
- 23 F. Melaine, C. Coilhac, Y. Roupioz and A. Buhot, *Nanoscale*, 2016, **8**, 16947–16954.
- 24 Q. Wang, J. Huang, X. Yang, K. Wang, L. He, X. Li and C. Xue, *Sens. Actuators, B*, 2011, **156**, 893–898.
- 25 E. Zeidan, R. Shivaji, V. C. Henrich and M. G. Sandros, *Sci. Rep.*, 2016, **6**, 26714.
- 26 O. A. Alsager, S. Kumar, B. Zhu, J. Travas-Sejdic, K. P. McNatty and J. M. Hodgkiss, *Anal. Chem.*, 2015, **87**, 4201–4209.
- 27 C.-C. Huang, Y.-F. Huang, Z. Cao, W. Tan and H.-T. Chang, *Anal. Chem.*, 2005, **77**, 5735–5741.
- 28 M. Bauch, S. Hageneder and J. Dostalek, *Opt. Express*, 2014, **22**, 32026–32038.
- 29 M. Bauch, K. Toma, M. Toma, Q. Zhang and J. Dostalek, *Plasmonics*, 2014, **9**, 781–799.
- 30 L.-Q. Chu, R. Förch and W. Knoll, *Angew. Chem., Int. Ed.*, 2007, **46**, 4944–4947.
- 31 F. Yu, B. Persson, S. Löfås and W. Knoll, *J. Am. Chem. Soc.*, 2004, **126**, 8902–8903.
- 32 Q. W. Song, M. S. Peng, L. Wang, D. C. He and J. Ouyang, *Biosens. Bioelectron.*, 2016, **77**, 237–241.
- 33 Y. F. Pang, Z. Rong, R. Xiao and S. Q. Wang, *Sci. Rep.*, 2015, **5**, 1.
- 34 D. A. Weitz, S. Garoff, C. D. Hanson, T. J. Gramila and J. I. Gersten, *J. Lumin.*, 1981, **24**, 83–86.
- 35 H. Cang, Y. Liu, Y. Wang, X. Yin and X. Zhang, *Nano Lett.*, 2013, **13**, 5949–5953.
- 36 M. E. Koivunen and R. L. Krogsrud, *Lab. Med.*, 2006, **37**, 490–497.
- 37 A. T. Csordas, A. Jørgensen, J. Wang, E. Gruber, Q. Gong, E. R. Bagley, M. A. Nakamoto, M. Eisenstein and H. T. Soh, *Anal. Chem.*, 2016, **88**, 10842–10847.
- 38 K.-A. Lee, J.-Y. Ahn, S.-H. Lee, S. Singh Sekhon, D.-G. Kim, J. Min and Y.-H. Kim, *Sci. Rep.*, 2015, **5**, 10897.
- 39 A. Sosic, A. Meneghello, E. Cretaio and B. Gatto, *Sensors*, 2011, **11**, 9426–9441.
- 40 A. Chen, M. Yan and S. Yang, *TrAC, Trends Anal. Chem.*, 2016, **80**, 581–593.
- 41 J. Liu, W. Bai, S. Niu, C. Zhu, S. Yang and A. Chen, *Sci. Rep.*, 2014, **4**, 7571.

- 42 J.-H. Park, J.-Y. Byun, W.-B. Shim, S. U. Kim and M.-G. Kim, *Biosens. Bioelectron.*, 2015, **73**, 26–31.
- 43 Y. Tang, F. Long, C. Gu, C. Wang, S. Han and M. He, *Anal. Chim. Acta*, 2016, **933**, 182–188.
- 44 H. Yu, J. Canoura, B. Guntupalli, X. Lou and Y. Xiao, *Chem. Sci.*, 2017, **8**, 131–141.
- 45 S. E. Lee, Q. Chen, R. Bhat, S. Petkiewicz, J. M. Smith, V. E. Ferry, A. L. Correia, A. P. Alivisatos and M. J. Bissell, *Nano Lett.*, 2015, **15**, 4564–4570.
- 46 C. Liu, X. Liu, Y. Qin, C. Deng and J. Xiang, *RSC Adv.*, 2016, **6**, 58469–58476.
- 47 N. Yildirim, F. Long, C. Gao, M. He, H.-C. Shi and A. Z. Gu, *Environ. Sci. Technol.*, 2012, **46**, 3288–3294.
- 48 Q. Zhou, T. Kwa, Y. Gao, Y. Liu, A. Rahimian and A. Revzin, *Lab Chip*, 2014, **14**, 276–279.
- 49 K. S. McKeating, A. Aube and J.-F. Masson, *Analyst*, 2016, **141**, 429–449.
- 50 S. Ohlson, C. Jungar, M. Strandh and C.-F. Mandenius, *Trends Biotechnol.*, 2000, **18**, 49–52.
- 51 M. Strandh, B. Persson, H. Roos and S. Ohlson, *J. Mol. Recognit.*, 1998, **11**, 188–190.
- 52 E. Meiby, S. Knapp, J. M. Elkins and S. Ohlson, *Anal. Bioanal. Chem.*, 2012, **404**, 2417–2425.
- 53 M.-D. Duong-Thi, E. Meiby, M. Bergström, T. Fex, R. Isaksson and S. Ohlson, *Anal. Biochem.*, 2011, **414**, 138–146.
- 54 L. J. Nielsen, L. F. Olsen and V. C. Ozalp, *ACS Nano*, 2010, **4**, 4361–4370.
- 55 F. Melaine, Y. Roupioz and A. Buhot, *Microarrays*, 2015, **4**, 41.
- 56 D. E. Huizenga and J. W. Szostak, *Biochemistry*, 1995, **34**, 656–665.
- 57 T. Liebermann and W. Knoll, *Colloids Surf., A*, 2000, **171**, 115–130.
- 58 K. E. Nelson, L. Gamble, L. S. Jung, M. S. Boeckl, E. Naeemi, S. L. Golledge, T. Sasaki, D. G. Castner, C. T. Campbell and P. S. Stayton, *Langmuir*, 2001, **17**, 2807–2816.
- 59 K. Sergelen, S. Fossati, A. Turupcu, C. Oostenbrink, B. Liedberg, W. Knoll and J. Dostalek, *ACS Sens.*, 2017, DOI: 10.1021/acssensors.7b00131.
- 60 T. Liebermann, W. Knoll, P. Sluka and R. Herrmann, *Colloids Surf., A*, 2000, **169**, 337–350.
- 61 A. Dasgupta, in *Therapeutic Drug Monitoring*, Academic Press, Boston, 2012, pp. 1–29, DOI: 10.1016/B978-0-12-385467-4.00001-4.
- 62 M. Luke, in *Therapeutic Drug Monitoring*, Academic Press, Boston, 2012, pp. 243–267, DOI: 10.1016/B978-0-12-385467-4.00012-9.
- 63 S. S. Zhao, N. Bukar, J. L. Toulouse, D. Pelechacz, R. Robitaille, J. N. Pelletier and J.-F. Masson, *Biosens. Bioelectron.*, 2015, **64**, 664–670.
- 64 B. S. Ferguson, D. A. Hoggarth, D. Maliniak, K. Ploense, R. J. White, N. Woodward, K. Hsieh, A. J. Bonham, M. Eisenstein, T. Kippin, K. W. Plaxco and H. T. Soh, *Sci. Transl. Med.*, 2013, **5**, 213ra165–213ra165.
- 65 M. Farias, M. W. Gorman, M. V. Savage and E. O. Feigl, *Am. J. Physiol.: Heart Circ. Physiol.*, 2005, **288**, H1586–H1590.
- 66 B. B. Fredholm, *Sleep Biol. Rhythms*, 2011, **9**, 24–28.
- 67 F. M. Gribble, G. Loussouarn, S. J. Tucker, C. Zhao, C. G. Nichols and F. M. Ashcroft, *J. Biol. Chem.*, 2000, **275**, 30046–30049.
- 68 Z. Liu, S. Chen, B. Liu, J. Wu, Y. Zhou, L. He, J. Ding and J. Liu, *Anal. Chem.*, 2014, **86**, 12229–12235.
- 69 M. Bauch and J. Dostalek, *Opt. Express*, 2013, **21**, 20470–20483.
- 70 Y. Wang, J. Dostálek and W. Knoll, *Biosens. Bioelectron.*, 2009, **24**, 2264–2267.
- 71 F. Saint-Marcoux, in *Therapeutic Drug Monitoring*, Academic Press, Boston, 2012, pp. 103–119, DOI: 10.1016/B978-0-12-385467-4.00005-1.

Electronic Supplementary Information

Surface plasmon field-enhanced fluorescence reversible split aptamer biosensor

K. Sergelen,^{a, b, c} B. Liedberg,^b W. Knoll^a and J. Dostálek^a

^a *BioSensor Technologies, AIT-Austrian Institute of Technology, Muthgasse 11, 1190 Vienna, Austria. E-mail: jakub.dostalek@ait.ac.at. Tel: +43 50550 4470; Fax: +43 50550-4450*

^b *Nanyang Technological University, Centre for Biomimetic Sensor Science, School of Materials Science and Engineering, 50 Nanyang Drive, Singapore 637553*

^c *International Graduate School on Bionanotechnology, University of Natural Resources and Life Sciences, Austrian Institute of Technology and Nanyang Technological University.*

Characterization of the biointerface architecture

The surface mass density of neutravidin and S1-Biotin segment at the sensor surface was measured as 1.49 ng/mm² and 0.47 ng/mm², respectively. These values were determined from shifts of SPR dip in the angular reflectivity spectra presented in Figure S1. The surface mass density of neutravidin (molecular weight of 60kDa) is comparable to full packed monolayer [1]. The three – fold smaller surface mass density of the aptamer segment S1-Biotin (molecular weight of 9.37kDa) corresponds to about 2 strands immobilized per attached neutravidin.

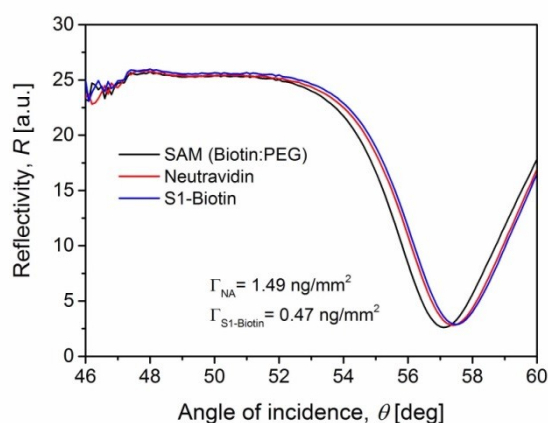


Figure S1. Angular reflectivity spectra $R(\theta)$ measured at sensor chip functionalization steps.

0

Thicknesses of immobilized NA and S1-Biotin were calculated by fitting the angular reflectivity spectra using transfer matrix-based model with the software Winspall (Max Planck Institute for Polymer Research, Germany). In the fitting, refractive index of buffer was assumed as $n_b=1.333$, n_{SAM} and refractive index n of polymer layer with a thickness d_p on the top of the gold surface was $n_p=1.45$. The surface mass density Γ is calculated with the obtained thickness values using the formula $\Gamma=(n_p-n_b) \cdot d_p \cdot \partial c / \partial n$, where $\partial n / \partial c=0.2 \text{ mm}^{-3} \text{ mg}^{-1}$.

Optimization of S2-AF647 concentration

In the fluorescence assay, the concentration of S2-AF647 aptamer segment was chosen based on data presented in Figure.S2. Fluorescence signal intensity was recorded for ATP-assisted formation of the complex between S1-Biotin and S2-AF647 segments. S2-AF647 concentration of 10 nM and 100 nM and varying ATP concentrations between 1 μM and 1 mM were used and the limit of detection (LOD) determined as a concentration for which the calibration curve intersects with the baseline noise. As the LOD for 100 nM concentration out-performed that for 10 nM S2-AF647 concentration, the higher one was used in the assay. The even higher concentration was not considered as the further increased background signal F_0 would limit the dynamic range of the fluorescence detection.

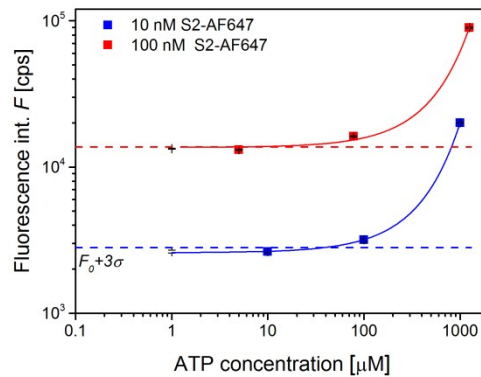


Figure S2. Titration measurements performed with S2-AF647 concentration of 10 nM and 100 nM and varying ATP concentrations between 1 μM and 1 mM.

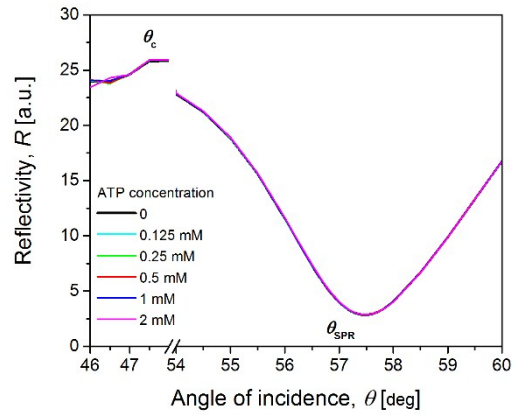


Figure S3. Angular reflectivity spectra $R(\theta)$ measured upon the affinity binding of ATP to the sensor surface from samples with ATP concentration from 0.125 to 2 mM (Figure 2 of manuscript).

Determination of equilibrium affinity binding constants

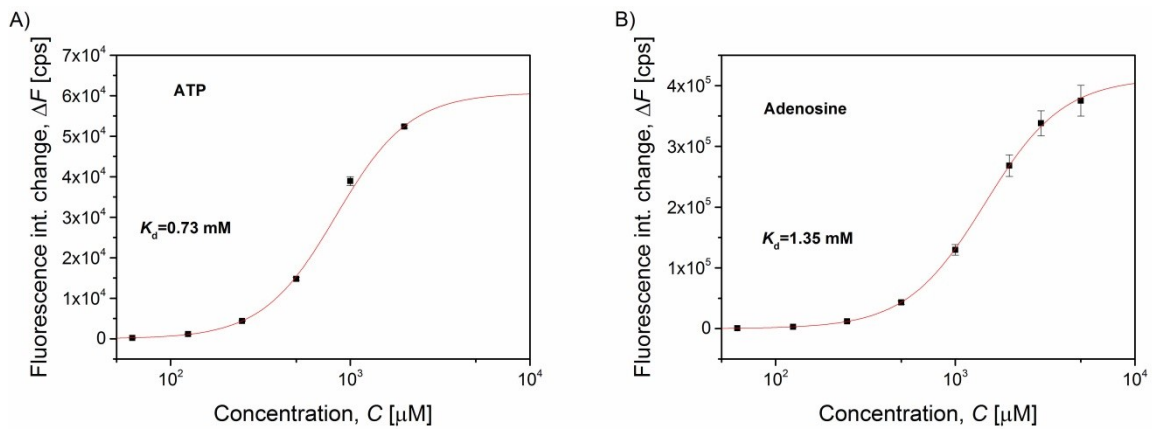


Figure S4. Calibration curves of A) ATP and B) Adenosine detection fitted with the Langmuir isotherm model. Dissociation constant K_d values determined as the half saturation concentration of the analyte.

Reversibility of the assay performed in 10% serum

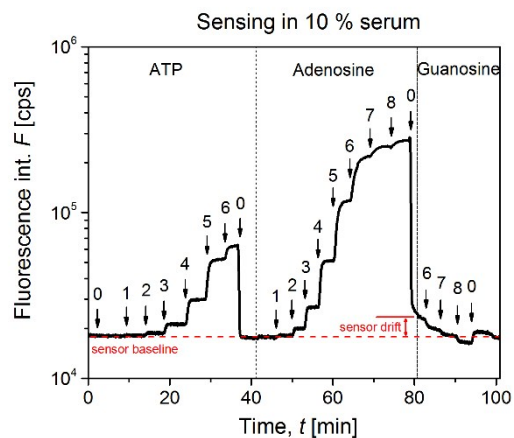


Figure S5. The titration measurements illustrating the reversibility of the split aptamer based assay in 10 % serum. Analyte concentrations indicated in sequential numbers are as follows: 0- 0; 1- 0.062 mM; 2- 0.125 mM; 3- 0.25 mM; 4- 0.5 mM; 5- 1 mM; 6- 2 mM; 7- 3 mM; 8- 5 mM, respectively.

References

- [1] T. Liebermann and W. Knoll, *Colloids and Surfaces A: Physicochemical and Engineering Aspects*, 2000, **171**, 115-130.

6. Free-standing hydrogel membrane with dynamically controlled permeability for lab-on-chip applications

Khulan Sergelen, Christian Petri, Ulrich Jonas and Jakub Dostálek, *Biointerphases*, submitted in July 2017.

Free-standing hydrogel-particle composite membrane with dynamically controlled permeability for lab-on-chip applications

Khulan Sergelen

BioSensor Technologies, AIT-Austrian Institute of Technology GmbH, Muthgasse 11, 1190 Vienna, Austria

Center for Biomimetic Sensor Science, Nanyang Technological University, 50 Nanyang Avenue, 637553 Singapore

International Graduate School on Bionanotechnology, University of Natural Resources and Life Sciences, Austrian Institute of Technology and Nanyang Technological University

Christian Petri

Macromolecular Chemistry, University of Siegen, Adolf-Reichwein-Strasse 2, 57076 Siegen, Germany

Ulrich Jonas

Macromolecular Chemistry, University of Siegen, Adolf-Reichwein-Strasse 2, 57076 Siegen, Germany

Jakub Dostalek^{a)}

BioSensor Technologies, AIT- Austrian Institute of Technology GmbH, Muthgasse 11, 1190 Vienna, Austria

^{a)} Electronic mail: jakub.dostalek@ait.ac.at

The preparation and investigation of a free-standing membrane made from a composite of thermoresponsive poly(*N*-isopropylacrylamide) (pNIPAAm) and polystyrene nanoparticles (PS NP) with temperature-controlled permeability is reported. The method exploits the light-induced crosslinking of the photo-reactive pNIPAAm-based polymer and mechanical reinforcement of the membrane structure by the polystyrene

nanoparticles. About micrometer thick layers were either directly attached to a gold surface or prepared as free-standing layers spanning over arrays of microfluidic channels with a width of about hundred microns by using template stripping. Diffusion of liquid medium, low molecular weight molecules, and large molecular weight proteins contained in blood through the composite membrane was observed with combined surface plasmon resonance (SPR) and optical waveguide spectroscopy (OWS). The swelling ratio, permeability, and non-specific sorption to these composite membranes were investigated by SPR and OWS as a function of molecular weight of analyte, loading of PS NP in the composite film, and temperature. We show successful preparation of a defect-free membrane structure that acts as a thermoresponsive filter with nanoscale pores spanning over an area of several square millimeters. This membrane can be reversibly switched to block or allow the diffusion of low mass molecules to the sensor surface by temperature-triggered swelling and collapsing of the hydrogel component. Low unspecific sorption and blocking of diffusion of proteins contained in blood serum is observed. These features make this platform interesting for potential future applications in continuous monitoring biosensors for the analysis of low molecular weight drug analytes or for advanced cell-on-chip microfluidic studies.

I. INTRODUCTION

Hydrogel materials are increasingly used in important fields spanning from tissue engineering,¹ drug delivery,² implants,³ and wound dressings^{4, 5} to various analytical technologies.⁶⁻⁸ Sensor and biosensor analytical applications typically take advantage of hydrogels that exhibit large surface area, are resistant to fouling by biomolecules present

in complex media and can be tailored to provide additional biological function.^{9, 10} They can be used as thin layers attached to a sensor surface that serve as a highly open binding matrix when post-modified with ligands specific to target analytes.¹¹⁻¹³ Besides affinity biosensors for *in situ* detection of analyte species, hydrogels are also pursued to advance implanted biosensors by preventing adhesion of cells and thus prolong their lifetime.¹⁴ In addition, cell-on-chip microfluidic systems increasingly employ hydrogels that mimic the extracellular matrix and which allow for design of complex artificial architectures resembling 3D living tissues.^{15,16} For instance, bulk silk hydrogels that were enzymatically crosslinked in a microfluidic device were successfully utilized for 3D cell culturing.¹⁷ In another approach an agarose based hydrogel was employed to form microfluidic channels for controlled biomolecule delivery to cell cultures.¹⁸ Besides bulk materials, structuring of hydrogels was demonstrated to be vital for culturing of specific cell types, for example vascularization by endothelial cells¹⁹, or neural cell network formation.²⁰ More complex hydrogel microstructures have been exploited in microfluidic actuators for stimuli-responsive control of liquid flow.^{21, 22, 23} In particular, they allowed fabrication of microfluidic valves^{24, 25} and reservoirs for pre-concentration of selected biomolecules.^{26, 27}

Among various geometries, hydrogel membranes attract increasing attention for many applications.²⁸ Such membranes were prepared by layer-by-layer polymer deposition onto a sacrificial layer through spin-coating to form a very thin (30-100 nm thick) suspended structure spanning over 10 μm gaps.²⁹ However, the majority of free-standing hydrogel membranes reported are much thicker. A porous, flexible free-standing composite hydrogel film with around 7 micron thickness was fabricated by filtration of

graphene and polyaniline hydrogel composite aggregates.³⁰ A crosslinked free-standing polyvinyl alcohol-based hydrogel film with 300 micrometer thickness was fabricated through solution casting in a predefined mold.³¹ Free-standing hydrogel macrostructures are also reported for syringe polymerization to yield tubular or cylindrical hydrogel structures³² or for molecular self-assembly into various predefined shapes.³³ Free-standing structures with various shapes and functionalities make an attractive means for sensing applications. In a recent report, free-standing molecularly imprinted photonic hydrogels with thickness of around 100 microns were constructed through a colloidal crystal templating method and applied for the detection of analytes.³⁴ A free-standing composite film composed of a gold nanoshell microsphere colloidal crystal and a polyacrylic acid-based hydrogel was prepared by photopolymerization and was utilized for sensing of pH changes.³⁵ Furthermore, the application of free-standing hydrogel structures expands to cellular studies, where for example, hydrogel biopaper substrates with 50-200 micron thickness were made with living cells and a hydrogel composite through polymerization on micropatterned substrates.³⁶ Thermoresponsive poly-(*N*-isopropyl)acrylamide (pNIPAAm) based free-standing hydrogel films (100-300 micron thickness) were constructed by injection compression molding.³⁷ Free-standing polyethylene glycol diacrylate-based hydrogel films with a thickness around 200 microns were prepared by polymerizing between Teflon-coated quartz plates and with these high water intake, anti-fouling, antimicrobial and oil/water filtration activities were demonstrated.³⁸ Recent studies have sought to improve hydrogel mechanical stability, stretchability³⁹ and macroshaping⁴⁰ that could be further applied for wearable sensors or tissue engineering.

We report on the facile preparation of a mechanically robust, thermoresponsive, free-standing pNIPAAm hydrogel-polystyrene nanoparticle (PS NP) composite membranes that span over a distance of 100 micrometers across microfluidic channels with a mere film thickness as low as one micrometer. These free-standing hydrogel membranes are prepared by template stripping over a channel array casted onto a surface plasmon resonance (SPR) sensor chip. Rapid diffusion of low molecular weight molecules and soluble constituents present in blood plasma is investigated for these pNIPAAm-PS NP composite membranes, and their on demand switching from a permeable to a closed states is demonstrated by combined optical waveguide spectroscopy (OWS) and SPR measurements.

II. EXPERIMENTAL

A. Materials

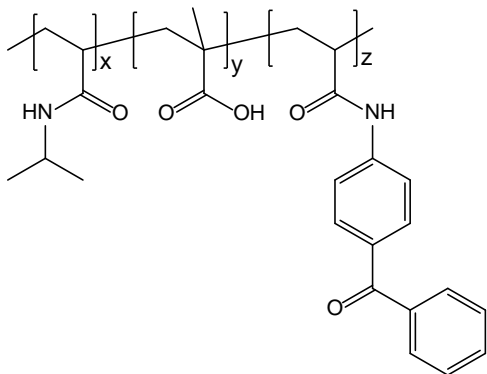
D-(+)-Maltose monohydrate was obtained from Carl Roth (Germany), phosphate buffered saline (PBS, 140mM NaCl, 10mM phosphate, 3mM KCl, pH 7.4) was purchased from Calbiochem (Germany), off-stoichiometry thiol-ene polymer (OSTEmer 322 Crystal clear) was obtained from Mercene Labs (Sweden), Hellmanex III was obtained from Hellma Analytics, Polybead 100nm microbeads (Polystyrene- PS) were purchased from PolySciences (Germany), newborn calf serum was purchased from Invitrogen (Germany), polydimethylsiloxane (PDMS, Sylgard 184) was obtained from Dow Corning (USA).

B. Experimental setup and methodology

1. *p*NIPAAm-based polymer

The *p*NIPAAm-based terpolymer with 94:5:1 molar ratio of *N*-isopropylacrylamide, methacrylic acid and 4-methacryloyloxy benzophenone was synthesized as previously described¹¹ and its structure is showed in Figure 1A.

(A)



(B)

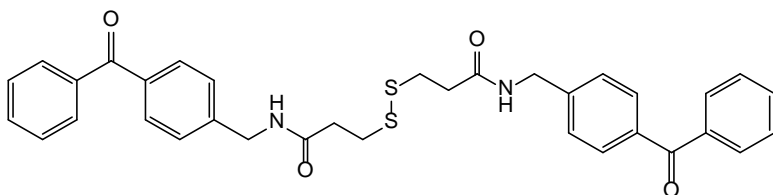


FIG. 1. Chemical structure of (A) the benzophenone-modified, crosslinkable, carboxylated *p*NIPAAm terpolymer and (B) the benzophenone-modified disulfide (4-AMBP-disulfide).

2. *3,3'*-Disulfanediylbis(*N*-(4-benzoylbenzyl)propanamide

For the surface attachment of the respective *p*NIPAAm-based composite films to the gold substrates, a novel benzophenone derivative with a disulfide anchor group was developed, see Figure 1B. For this purpose, bis(2,5-dioxopyrrolidin-1-yl) 3,3'-

disulfaneyldipropoate was reacted with 4-(aminomethyl)benzophenone (4-AMBP)⁴¹ in the presence of triethylamine at room temperature, see Figure S1. Bis(2,5-dioxopyrrolidin-1-yl) 3,3'-disulfaneyldipropoate (0.74 mmol, 0.30 g) was dissolved in DMSO (14 ml) and cooled with an ice-water bath to 0°C. 4-(Aminomethyl)benzophenone (3.30 mmol, 0.70 g) dissolved in DMSO (6 ml) and Et₃N (3.20 mmol, 0.45 ml) were added and the solution stirred for 16 h at room temperature. DCM (20 ml) was added and the organic layer was washed with water (2 × 20 mL). The formed precipitate in the organic layer was filtered off and washed with small portions of DCM, followed by drying of the remaining product under reduced pressure. The yield was of 51 % (0.38 mmol, 0.26 g) of a white solid. The resulting product was characterized by ¹H and ¹³C NMR spectroscopy (provided in the Supporting Information in Figures S2 and S3), showing only minor impurities of a mono-substituted product. IR spectroscopy showed bands (cm⁻¹) at 3295 (N-H), 3052 (C-H_{aromatic}), 2907 (C-H), 1641 (C=O).

3. *Nanocomposite hydrogel thin film preparation*

Composite hydrogel films were prepared by spin-coating an ethanolic solution with dissolved pNIPAAm and suspended polystyrene nanoparticles at weight fractions as specified in Table I. These films were either attached directly to a gold surface for the SPR/OWS studies or on top of an array of OSTEmer channels in order to serve as a free-standing membrane. Both types of structures were prepared on BK7 glass substrates that were cut into 20 × 25 mm pieces and sequentially washed with 1% Hellmanex III solution, distilled water and absolute ethanol, amid sonicating, and dried under air stream.

Subsequently, 2 nm chromium film and 50 nm thick gold films were deposited by vacuum thermal evaporation (HHV Auto306 Lab Coater).

TABLE I

pNIPAAm, wt %	PS nanoparticles, wt %	Ratio PS/pNIPAAm, r_c
2.5	0	0
2.5	0.625	0.25
2.5	1.25	0.5
2.5	2.5	1
2.5	3.5	1.4
1	5	5

For the preparation of attached composite films, gold-coated substrates were immersed overnight into 1 mM solution of 4-AMBP-disulfide dissolved in DMSO in order to form a self-assembled monolayer (SAM). Such benzophenone SAM-functionalized substrates were rinsed with copious amounts of ethanol and dried in a stream of air. An ethanolic solution with pNIPAAm and PS nanoparticles was then spun onto the sensor chip at 2000 rpm for 60 seconds followed by drying overnight at 50 °C under vacuum (Heraeus Vacuum Oven VT 6025, Thermo Scientific). The resulting films were crosslinked and simultaneously attached to the sensor chip via the photoreactive 4-AMBP-disulfide SAM by exposure to 365 nm UV light with an irradiation dose of 4 J/cm² followed by rinsing with ethanol and dried before measurements.

In order to prepare a free-standing pNIPAAm/PS NP-based membrane, the modified procedure introduced in Figure 2 was developed. Firstly, nanocomposite polymer layer was deposited on a flat PDMS block (2 × 2 × 0.5 cm) by spin coating at

1000 rpm for 60 seconds followed by drying overnight at 35 °C. Meanwhile, a PDMS stamp with casted arrays of grooves was placed above a gold-coated substrate (step A in Figure 2) and the formed channels were filled with an OSTEmer resin by the capillary effect (step B in Figure 2). The OSTEmer was then UV-cured with an irradiation dose of 0.8 J/cm² at a wavelength of 365 nm. Subsequently, the PDMS stamp was removed exposing arrays of adhesive OSTEmer ribs with reactive epoxy groups (step C in Figure 2). The hydrogel nanocomposite membrane on the flat PDMS (step D in Figure 2) was then placed over the OSTEmer structure and allowed to bond at 40 °C overnight (step E in Figure 2). Finally, the flat PDMS support was lifted off the hydrogel membrane to reveal a free-standing membrane spanning over the OSTEmer channel structure (step F in Figure 2). The resulting cavities, which were capped with the composite pNIPAAm-based polymer films, had a depth of $d_c=45 \mu\text{m}$ and a width of $w_c=30\text{-}95 \mu\text{m}$.

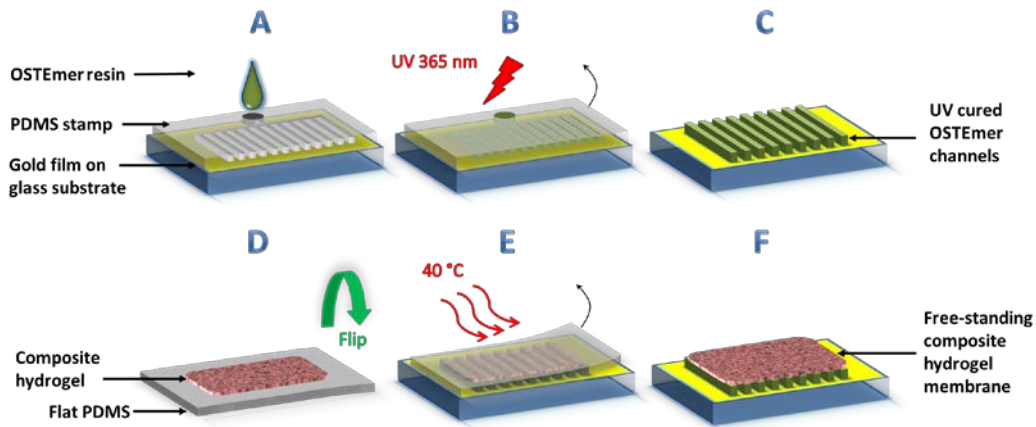


FIG.2. Preparation of thin hydrogel composite films attached as a free-standing membrane spanning over a narrow channel: (A) filling of PDMS channels with OSTEmer on gold surface followed by (B) UV curing and (C) detachment of the PDMS support to reveal epoxy-activated OSTEmer channel structures, then (D) transfer of spin-coated,

dried and crosslinked hydrogel-PS NP composite film on flat PDMS onto OSTEm channels and subsequently (E) thermal hardening and bonding of OSTEm channels to the composite hydrogel films. Finally, (F) lifting off the PDMS support to reveal free-standing composite hydrogel membrane over OSTEm channel structures.

4. *Visualization of the hydrogel composite morphology*

Hydrogel composite films and membranes were investigated using an optical microscope (Olympus BX51M) and a scanning electron microscope (SEM) operated at a low voltage of 5 kV (Carl Zeiss EVO). Samples of hydrogel composite films or membranes were sputtered (Cressington Sputter Coater 108auto) for SEM with a 13 nm thick layer of platinum.

5. *Optical setup for SPR/OWS measurements*

SPR and OWS measurements were carried out by using an optical setup with the Kretschmann configuration of attenuated total reflection (ATR) which was described in our previous works in more detail.⁴² As Figure 3 shows, the glass substrate with hydrogel nanocomposite film was optically matched onto a LASFN9 glass prism with an appropriate immersion oil. A laser beam at $\lambda=633$ nm was coupled to the prism to hit the gold surface at an angle θ . The angular reflectivity spectrum $R(\theta)$ was measured by using a rotation stage for transverse magnetic (TM) and transverse electric (TE) polarization. In order to flow aqueous samples over the surface of the pNIPAAm-based composite film, a flow cell was clamped and connected to a peristaltic pump (Ismatec, IDEX Health & Science SA, Switzerland) by using Tygon tubing with an inner diameter of 0.25 μm . For

temperature-controlled permeability measurements a Peltier element was integrated into a flow-cell as described before.¹¹

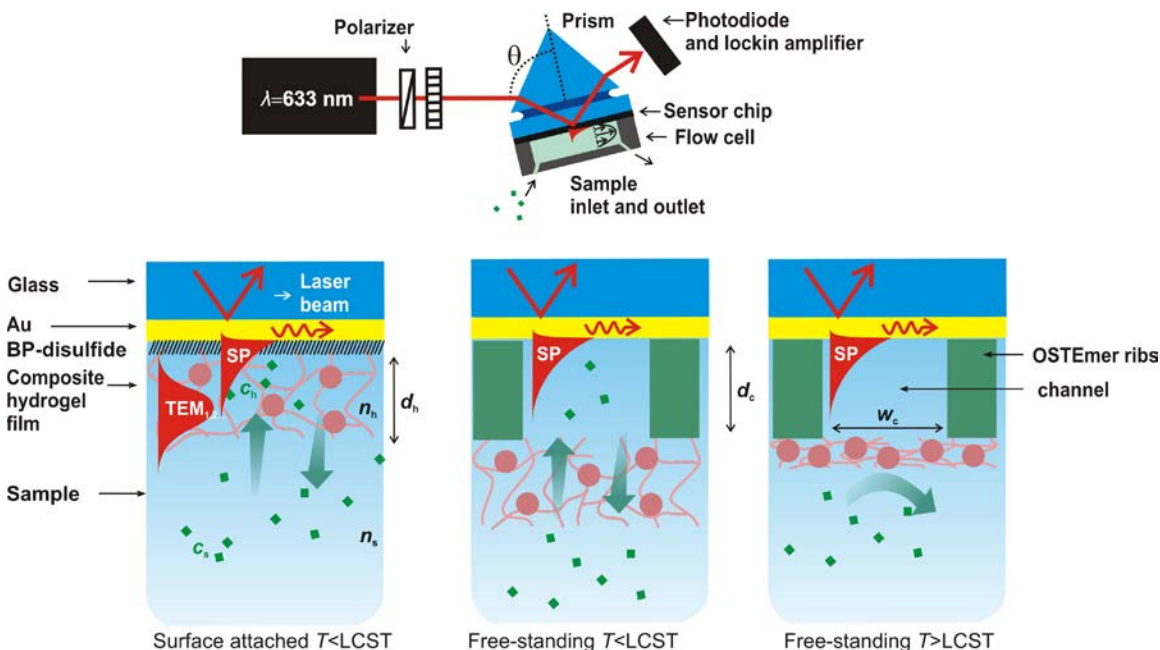


FIG. 3. Optical setup for the observation of thin hydrogel films and diffusion of biomolecules based on combined surface plasmon resonance (SPR) and optical waveguide spectroscopy (OWS).

6. Acquisition and evaluation of SPR/OWS data

The swelling properties of hydrogel composite film attached to a gold surface were investigated by OWS. In this method, the refractive index n_h and thickness d_h of the layer were determined by fitting the measured angular reflectivity spectra $R(\theta)$. These spectra exhibit series of characteristic dips at certain angles due to the resonant excitation of surface plasmons (SPs) and higher waveguide modes ($TEM_{1,2,\dots}$), see Figure.S3 in Supporting Information. By using transfer matrix-based model implemented in the

software Winspall (MPI for Polymer Research, Germany), the optical properties of prepared films were assessed.⁴³ Parameters of the BK7 glass substrate, chromium, gold and disulfide linker SAM layers are kept constant throughout all fitting as determined on substrates without the hydrogel composite.

For the study of permeation of blood serum and low molecular weight maltose analyte to the attached composite hydrogel film, changes in the refractive index of the film n_h were compared to those measured for the solution n_s flowed over the surface. Refractive index n_s was determined from changes in the critical angle θ_c (see Figure S4). Changes in these refractive indices Δn_s and Δn_h were assumed to be proportional to the concentration of the analyte molecules in the liquid sample c_s and in the hydrogel composite c_h , respectively. Consequently, the concentration ratio of biomolecules in the layer and that in the sample relates directly to the corresponding ratio of refractive index changes $c_h/c_s = \Delta n_h / \Delta n_s$.

For the study of permeation of low molecular weight analyte through the free-standing hydrogel composite membrane, the gold surface at the bottom of the OSTEmer channel was probed by resonantly excited SPs (see bottom right of Figure 3). Changes in the reflectivity R due to the refractive index changes induced by the analyte diffusion were recorded in time at incidence angle θ fixed at the slope of the SPR dip.

III. RESULTS AND DISCUSSION

A. Morphology of prepared membranes

The surface morphology of the crosslinked polymer films being composed of pNIPAAm-based polymer and PS nanoparticles was firstly scrutinized by SEM. The panels of the left row in Figure 4 shows the acquired top view for films prepared with the weight fraction ratio for PS nanoparticles versus pNIPAAm of $r_c=0.25$, 0.5, and 1. These images reveal that the PS nanoparticles are homogeneously embedded in the pNIPAAm matrix and that an increasing concentration of the nanoparticles in the solution spun on the surface leads to an apparent increase of the NP density in the film. For the studied range, the middle and right panels of Figure 4 confirm that the dry composite films with a thickness of $d_{h-dry}=70$ -280 nm could be successfully transferred on top of the OSTEmer channels with a width of $w_c=30$ μm . From previous studies of the pNIPAAm matrix on planar PS substrates it can be inferred that the PS particles are covalently attached to the pNIPAAm network after photocrosslinking,⁴⁴ which is also corroborated by the robustness of the composite membrane in the swelling studies described below.

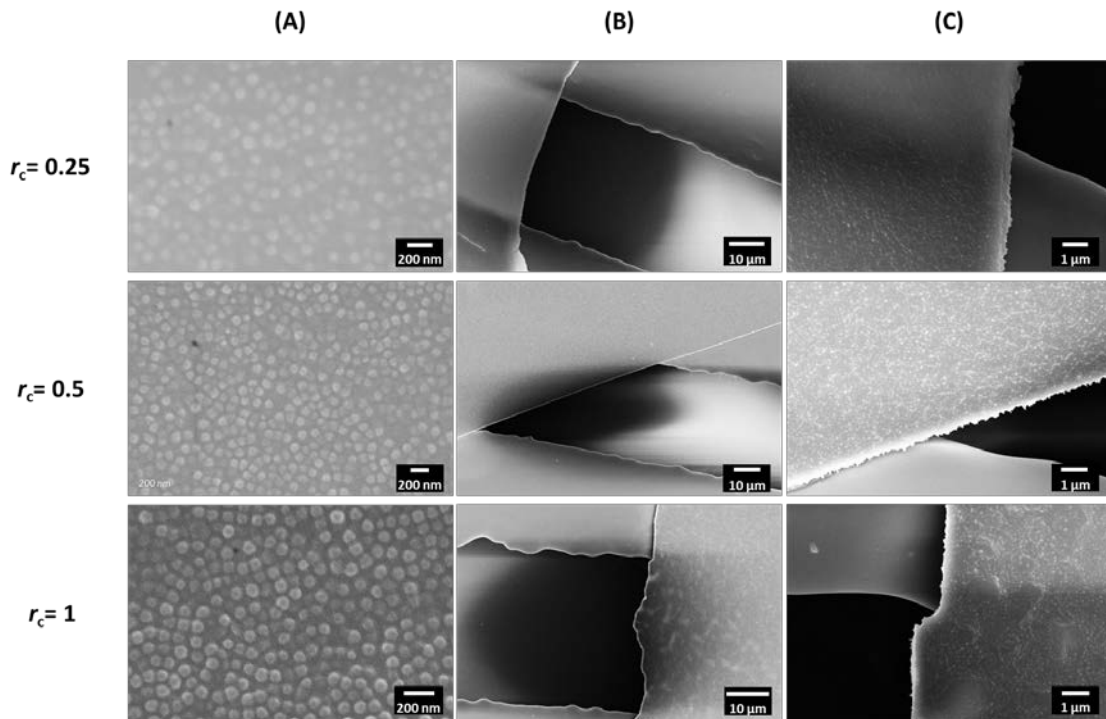


FIG. 4. SEM images of dry prepared composite films. Columns show (A) top view of composite films, (B) broad view of a free-standing composite membrane spanning over a channel and (C) close-up view of the edge of the free-standing composite membrane.

B. Swelling properties of nanocomposite films

When exposed to aqueous media, the hydrogel matrix is able to swell and form a permeable structure. To test the swelling of prepared membranes spanning over the channels in water, optical microscopy was used. Figure.5 shows series of images obtained for hydrogel films with varied composition $r_c=0, 0.25, 0.5,$ and 1. The upper panel was measured in water at room temperature $T=20$ °C and the lower panel is measured after removing the water and letting the membrane dry for 10 minutes at room temperature. The composite hydrogel membranes show 3D swelling behavior that leads to their buckling. However, with increasing content of PS particles, the composite hydrogel membranes swell less, which reduces this effect. The increasing mechanical rigidity of the hydrogel composite membrane was visually observed during preparation, however membranes with the higher concentrations of PS ($r_c=0.5,$ and 1) were more brittle.

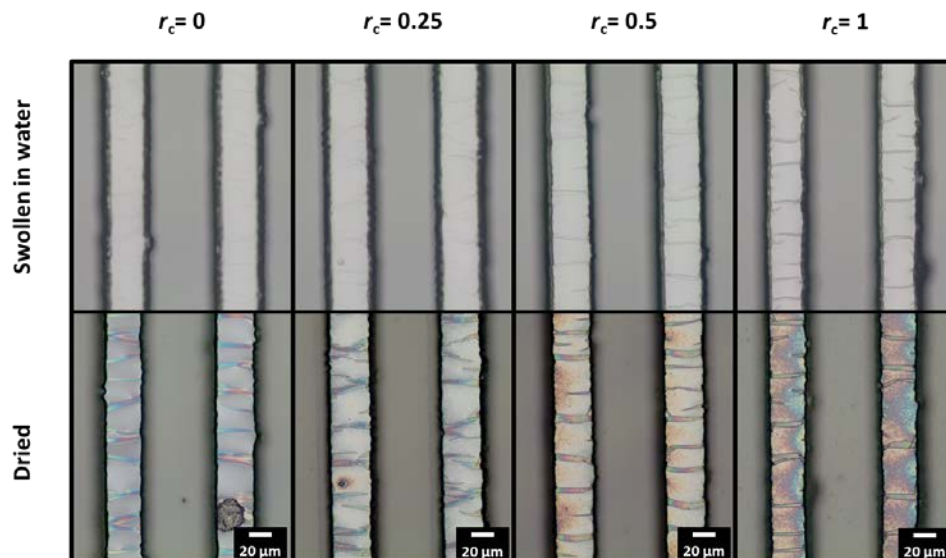


FIG. 5. Optical microscope images of free-standing composite membranes spanning over a 30 micrometer-wide microfluidic channel. Columns show structures with varied wt % PS/pNIPAAm ratio $r_c=0, 0.25, 0.5,$ and 1. Upper row shows images acquired in water and bottom row after drying in air.

With the aim of characterizing the role of embedded PS nanoparticles on the swelling behavior and mechanical stability of hydrogel membranes, OWS was used to measure the changes in the swelling ratio of the composite films attached to a planar gold surface. The swelling ratio (SR) of composite films was calculated as the ratio of the swollen film thickness d_h to the dry thickness d_{h-dry} . The measured dependence on the loading with PS nanoparticles r_c is presented in Figure 6. The SR of hydrogel composite is strongly suppressed by a factor of about 2-fold when PS nanoparticle loading is $r_c=0.25$ compared to the native hydrogel film ($r_c=0$). Further reduction in the swelling of hydrogel composite films with increased loading of PS nanoparticles is observed. For higher PS loads of $r_c=1$ and 5, almost no swelling occurs, as evidenced by the measured

SR of around 1. The reduction of the SR for composite hydrogels with PS nanoparticles is consistent with previous reports of a similar system.⁴⁵

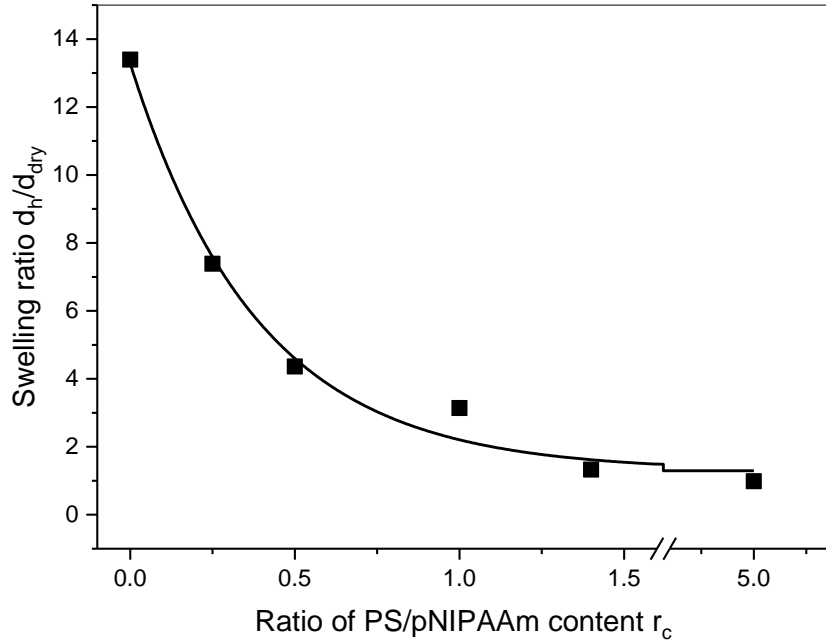


FIG.6. Swelling ratio of surface-attached hydrogel composite films with varying loading ratio of PS nanoparticles in the pNIPAAm matrix. Temperature of measurement $T=20^{\circ}\text{C}$.

The swelling ratio SR relates to the mesh size of the polymer networks. For instance, for a similar native pNIPAAm hydrogel film swollen in ethanol with $SR=12$ exhibited a mesh size of 3.4 nm as determined by fluorescence correlation spectroscopy.⁴⁶ In addition, it is worth noting that the herein performed OWS measurements capture only swelling in the direction perpendicular to the substrate plane as the studied films were covalently attached to the solid substrate. In contrast, the swelling of free-standing membranes can also occur laterally by a buckling mode (visible in Figure 5), which the OWS data does not take into account.

C. Permeability of the attached nanocomposite films

For the observation of diffusion of biomolecules through the composite membrane, the same OWS technique was employed with a series of aqueous sample being flowed over the surface-attached composite films. The diffusion of biomolecules dissolved in such liquid samples were determined from the measured refractive index changes Δn_s and Δn_c which are directly proportional to the biomolecule concentration. These measurements were performed at $T=20$ °C, which is below the LCST of the pNIPAAm matrix in order to assure appropriate swelling.

Firstly, diffusion of the small analyte maltose with a molecular weight of 0.36 kDa, dissolved in PBS buffer at a concentration of $c_s=0.2$ M, was measured. Before the beginning of the diffusion experiments, each composite film was exposed to PBS solution to allow equilibrium swelling. Then, PBS with maltose was flowed for more than 10 min until equilibrium in diffusion was reached. The reflectivity spectra were measured for the structures immersed in PBS and in PBS with maltose (see Figure S3 in Supporting Information). The analysis of the acquired spectra allowed the determination of the maltose concentration in the composite film that was normalized with that in the bulk solution c_h/c_s . Results in Figure 7 show a slow decrease of the c_h/c_s from about 0.85 to 0.4 when increasing the loading of PS nanoparticles in the composite from $r_c=0$ to 5. These data indicate efficient diffusion of the low molecular weight analyte through the hydrogel network between the PS nanoparticles (which are impermeable by the aqueous solution) and are consistent with complementary FCS data on diffusion of small fluorophore tracers.⁴⁷

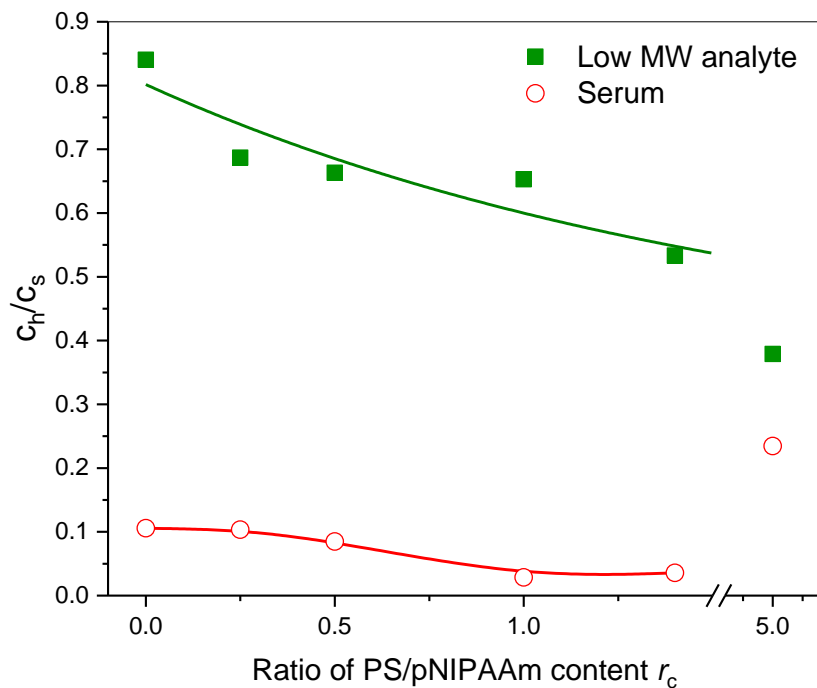


FIG. 7. OWS investigation of the diffusion of a low molecular weight analyte (maltose, MW=0.36 kDa, at a concentration of 0.2 M in PBS buffer) and undiluted blood serum (molecular weights of major protein components 66 kDa – 160 kDa) through the surface-attached hydrogel composite film with varying wt% ratio of PS NP/pNIPAAm $r_c=0-5$.

In order to assess information on the diffusion of biomolecules with larger molecular weight, the interaction of composite films with undiluted blood serum was studied by OWS. The majority of proteins present in serum exhibit a molecular weight between 66 kDa and 160 kDa. The obtained data presented in Figure 7 indicate that for a hydrogel film without PS nanoparticles, the concentration of biomolecules that diffuse into the polymer network is ten times lower compared to that in serum $c_h/c_s=0.1$. When decreasing the swelling ratio SR by introducing PS nanoparticles, the permeation of proteins is further hindered to $c_h/c_s=0.03$ for $r_c=1.5$. Surprisingly, the amount of serum

proteins that is present in the composite film is enhanced to about $c_h/c_s=0.25$ when increasing the loading with PS nanoparticles to $r_c=5$. This effect can be attributed to only partial coverage of PS nanoparticles with pNIPAAm hydrogel which leads to unspecific sorption of proteins to polystyrene surface. In addition, the mechanical swelling stress may lead to the occurrence cracks of brittle membranes with high r_c . This effect in conjunction with low content of hydrogel can strongly increase the pore size to values much greater than the hydrodynamic radius of large proteins like IgG ($R_h = 6.5$ nm).⁴⁸ It is worth of noting that a similar effect was observed for the pNIPAAm-based composite film with molecularly imprinted polymer nanoparticles.⁴⁹

In order to distinguish between protein molecules diffusion through the membrane and their unspecific sorption, OWS measurements were performed after the exposure to undiluted serum for 30 minutes and rinsing with PBS for 10 min. Indeed, the effect fouling of the network with serum was not measurable for the composites with $r_c=0-1.5$. Contrary to these results, composite with very high nanoparticle content $r_c=5$ showed a significant increase in the refractive index $\Delta n_h=2\times 10^{-4}$ due to the unspecific sorption of serum proteins. This value translates to an increase in the surface mass density of the composite film by 2.1 % and it can be attributed to the fact that at high r_c , PS nanoparticles are not capped with hydrophilic pNIPAAm hydrogel and thus are prone to unspecific sorption of proteins.^{49, 50}

D. Permeability of free-standing nanocomposite film

The permeability of the free-standing membrane spanning the channel structure (refer to scheme in Fig. 2), which was prepared with a thickness of ~ 1 μm and a PS

nanoparticles loading of $r_c=0.33$, was tested for the low molecular weight analyte maltose. In these experiments, the possibility to reversibly switch the permeation by controlling the swelling state of the pNIPAAm-based membrane with temperature was explored. The pNIPAAm polymer exhibits a lower critical solution temperature at $LCST=32\text{ }^\circ\text{C}$ and increasing the temperature above the LCST leads to the collapse of the networks. In the collapsed state a denser membrane will result possessing a smaller pore size. The transport of maltose through the composite film in the permeable "open" state at $T=20\text{ }^\circ\text{C}$ and in the collapsed "closed" state at $T=40\text{ }^\circ\text{C}$ was monitored by probing the liquid volume in the channel below the membrane by resonantly excited SPs at the gold surface (see Figure 3). The distance of the membrane from the gold was of about $d_c=45\text{ }\mu\text{m}$ which is more than two orders of magnitude longer than the probing depth of the evanescent SP field of about $0.1\text{ }\mu\text{m}$. Therefore, the measured changes in SPR can be specifically attributed to only species that diffuse into the cavity through the membrane.

Firstly, the membrane was heated to $T=40\text{ }^\circ\text{C}$ (collapsed state) and water was circulated through the flow-cell over the top of the composite membrane. After equilibration to establish a stable baseline in the SPR signal, the 0.2 M maltose PBS solution at this elevated temperature was injected at $t=5\text{ min}$ followed by rinsing with warm water at $t=12\text{ min}$. The respective SPR kinetics are shown in Figure 8 (curve 1). Apparently, the maltose diffusion across the membrane is hindered at $T=40\text{ }^\circ\text{C}$, thus no measurable increase in the refractive index within the channel under the membrane occurs.

Secondly, the membrane was cooled to $T=20\text{ }^\circ\text{C}$ and the same experiment was repeated. Contrary to the previous data, the measured curve 2 in Figure 8 shows that the

injection of maltose induces a strong increase in SPR signal after $t=5$ min, which reaches equilibrium after several minutes. When rinsing the top flow cell with cold water, the maltose quickly diffuses out through the membrane, which is manifested as a decrease in the reflectivity after $t=12$ min. The observed time response of several minutes is in agreement with the diffusion-controlled transfer, which can be described based on Fick's law as $\Delta t \sim d_c^2/D$. Assuming a diffusion coefficient of maltose of $D=5 \times 10^{-6} \text{ cm}^2\text{s}^{-1}$,⁵¹ the characteristic time of $\Delta t \sim 5$ s is predicted to fill the channels. The measured response time in the minute range is significantly longer, which can be ascribed to the slower, hindered diffusion through the hydrogel composite membrane and to the mixing occurring upon the transport in the flow-cell and tubing.

Finally, the membrane was kept at $T=20$ °C for which maltose can diffuse through the swollen composite membrane and fill the probed channels. After saturating the liquid volume in the channel with maltose, the membrane was heated to $T=40$ °C which switches it to the collapsed, non-permeable state. As curve 3 in Figure 8 reveals, when the volume of the flow-cell above was rinsed with warm water, the diffusion of maltose through the sealed membrane is strongly hindered and only a slow decrease in the SPR signal is observed.

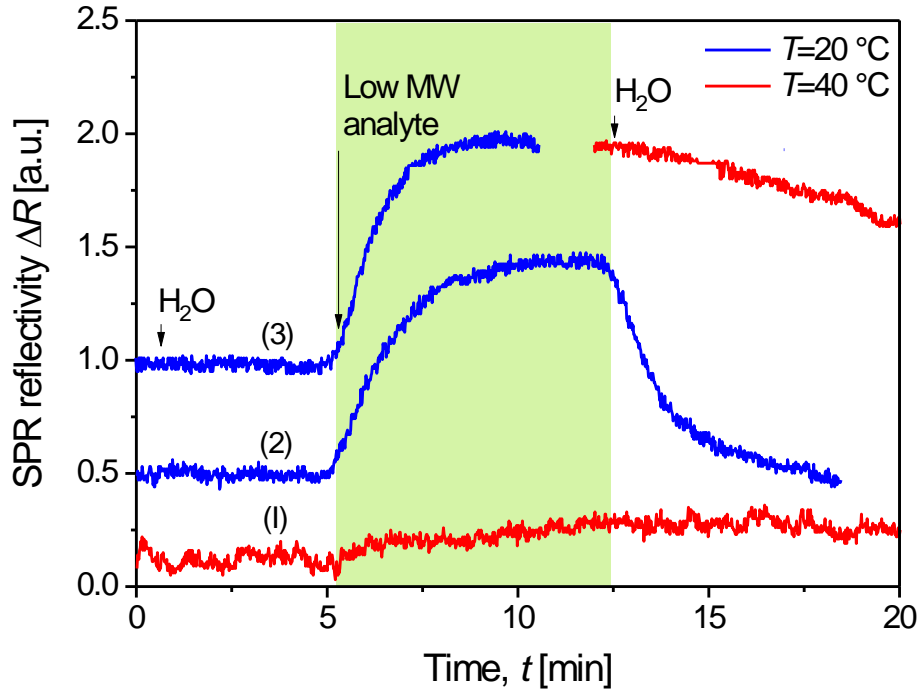


FIG. 8. SPR investigation of diffusion of low molecular weight analyte (maltose, MW=0.36 kD, dissolved 0.5 mM in PBS buffer) across the free-standing PS / pNIPAAm composite membrane with $r_c=0.25$. The permeability of the membrane was switched by changing the temperature from the "open" state at $T=20$ °C below the LCST of NIPAAm (around 32°C) to the "closed" state at $T=40$ °C above the LCST. Curves (1) indicate the closed state, (2) the open state, and (3) diffusion of molecules through open membrane and their trapping by switching to closed state.

IV. SUMMARY AND CONCLUSIONS

In this report, PS nanoparticle were incorporated into a pNIPAAm hydrogel matrix to produce free-standing hydrogel membranes with improved mechanical stability. We utilized a thiol-ene-epoxy resin OSTEmmer to fabricate microchannel structures that can be firmly bound to the hydrogel composite in a simple two-step process, yielding a

free-standing membrane over a total area of about one square millimeter. Investigation of the morphology in the hydrogel-nanoparticle composite revealed a reduced bulging of the membranes when swollen in water as compared to a neat hydrogel membrane without PS nanoparticles. Surface-attached films of these hydrogel composites were investigated by SPR/OWS for their swelling behavior, as well as the selective permeability for low molecular-weight compound and large proteins present in complex blood serum samples. Hydrogel composites with an excess of the hydrogel component compared to the PS nanoparticle content showed efficient semi-permeability to maltose while blocking serum proteins, as well as sound non-fouling capability. In contrast, an excess of PS nanoparticle loading in the hydrogel matrix lead to an enhanced adsorption of the serum proteins (potentially by a large increase of the fouling PS particle surface), in addition to loss of the semi-permeability. Finally, the thermal response of the swelling state in the pNIPAAm hydrogel was exploited to dynamically control the permeability of the free-standing composite membrane. The SPR observation showed rapid diffusion of low molecular weight molecules through the swollen membrane at temperatures below the LCST of 32°C and blocking of the diffusion when collapsing the hydrogel at a temperature well above its LCST. The herein reported semi-permeable, free-standing hydrogel composite membranes can be applied to various microstructures and microfluidic architectures, paving the way for a wide range of novel applications in lab-on-a-chip⁵² or biosensing⁵³ of crude samples (e.g. whole blood or serum).⁵⁴

ACKNOWLEDGMENTS

KS acknowledges financial support from the Austrian Federal Ministry for Transport, Innovation and Technology (GZ BMVIT-612.166/0001-III/I1/2010).

See supplementary material at [URL will be inserted by AIP Publishing] for synthesis, ^1H NMR and ^{13}C NMR spectra of 3,3'-disulfanediybis(*N*-(4-benzoylbenzyl)propanamide) and angular reflectivity spectra of composite films.

References

1. F. Chen, S. Yu, B. Liu, Y. Ni, C. Yu, Y. Su, X. Zhu, X. Yu, Y. Zhou and D. Yan, *Scientific Reports* **6**, 20014 (2016).
2. T. Billiet, M. Vandehaute, J. Schelfhout, S. Van Vlierberghe and P. Dubruel, *Biomaterials* **33** (26), 6020-6041 (2012).
3. A. K. Riau, D. Mondal, T. T. Aung, E. Murugan, L. Y. Chen, N. C. Lwin, L. Zhou, R. W. Beuerman, B. Liedberg, S. S. Venkatraman and J. S. Mehta, *ACS Biomater. Sci. Eng.* **1** (12), 1324-1334 (2015).
4. J. Li and D. J. Mooney, *Nature Reviews Materials* **1**, 16071 (2016).
5. C. M. Magin, D. B. Neale, M. C. Drinker, B. J. Willenberg, S. T. Reddy, K. M. D. La Perle, G. S. Schultz and A. B. Brennan, *Experimental Biology and Medicine* **241** (9), 986-995 (2016).
6. G. Sun, X. Zhang, Y.-I. Shen, R. Sebastian, L. E. Dickinson, K. Fox-Talbot, M. Reinblatt, C. Steenbergen, J. W. Harmon and S. Gerecht, *Proceedings of the National Academy of Sciences of the United States of America* **108** (52), 20976-20981 (2011).
7. D. Puchberger-Enengl, C. Krutzler, F. Keplinger and M. J. Vellekoop, *Lab on a Chip* **14** (2), 378-383 (2014).
8. H. Vaisocherova, W. Yang, Z. Zhang, Z. Q. Cao, G. Cheng, M. Pilarik, J. Homola and S. Y. Jiang, *Analytical Chemistry* **80** (20), 7894-7901 (2008).
9. A. Mateescu, Y. Wang, J. Dostalek and U. Jonas, *Membranes* **2** (1), 40-69 (2012).
10. T. Ekblad, G. Bergstroem, T. Ederth, S. L. Conlan, R. Mutton, A. S. Clare, S. Wang, Y. L. Liu, Q. Zhao, F. D'Souza, G. T. Donnelly, P. R. Willemsen, M. E. Pettitt, M. E. Callow, J. A. Callow and B. Liedberg, *Biomacromolecules* **9** (10), 2775-2783 (2008).
11. A. Aulasevich, R. F. Roskamp, U. Jonas, B. Menges, J. Dostálek and W. Knoll, *Macromolecular Rapid Communications* **30** (9-10), n/a-n/a (2009).
12. Y. Wang, A. Brunsen, U. Jonas, J. Dostalek and W. Knoll, *Analytical Chemistry* **81** (23), 9625-9632 (2009).
13. O. Andersson, A. Larsson, T. Ekblad and B. Liedberg, *Biomacromolecules* **10** (1), 142-148 (2009).

14. R. M. Gant, A. A. Abraham, Y. Hou, B. M. Cummins, M. A. Grunlan and G. L. Cote, *Acta Biomater.* **6** (8), 2903-2910 (2010).
15. X. J. Li, A. V. Valadez, P. Zuo and Z. H. Nie, *Bioanalysis* **4** (12), 1509-1525 (2012).
16. M. B. Chen, S. Sriganapalan, A. R. Wheeler and C. A. Simmons, *Lab on a Chip* **13** (13), 2591-2598 (2013).
17. S. Zhao, Y. Chen, B. P. Partlow, A. S. Golding, P. Tseng, J. Coburn, M. B. Applegate, J. E. Moreau, F. G. Omenetto and D. L. Kaplan, *Biomaterials* **93**, 60-70 (2016).
18. S. Cosson and M. P. Lutolf, **4**, 4462 (2014).
19. S. Muehleder, A. Ovsianikov, J. Zipperle, H. Redl and W. Holthoner, *Frontiers in Bioengineering and Biotechnology* **2** (52) (2014).
20. K. Yoichi, N. Yoji, Y. Yuya, Y. Masumi and S. Minoru, *Biofabrication* **6** (3), 035011 (2014).
21. L. Dong and H. Jiang, *Soft Matter* **3** (10), 1223-1230 (2007).
22. X. Zhang, L. Li and C. Luo, *Lab on a Chip* **16** (10), 1757-1776 (2016).
23. D. H. Kang, S. M. Kim, B. Lee, H. Yoon and K.-Y. Suh, *Analyst* **138** (21), 6230-6242 (2013).
24. D. J. Beebe, J. S. Moore, J. M. Bauer, Q. Yu, R. H. Liu, C. Devadoss and B.-H. Jo, *Nature* **404** (6778), 588-590 (2000).
25. R. H. Liu, Y. Qing and D. J. Beebe, *Journal of Microelectromechanical Systems* **11** (1), 45-53 (2002).
26. R. R. Niedl and C. Beta, *Lab on a Chip* **15** (11), 2452-2459 (2015).
27. T. Shay, M. D. Dickey and O. D. Velev, *Lab on a Chip* **17** (4), 710-716 (2017).
28. I. Tokarev and S. Minko, *Advanced Materials* **21** (2), 241-247 (2009).
29. C. Jiang and V. V. Tsukruk, *Soft Matter* **1** (5), 334-337 (2005).
30. M. Moussa, Z. Zhao, M. F. El-Kady, H. Liu, A. Michelmore, N. Kawashima, P. Majewski and J. Ma, *Journal of Materials Chemistry A* **3** (30), 15668-15674 (2015).
31. N. Batische and E. Raymundo-Piñero, *Journal of Power Sources* **348**, 168-174 (2017).
32. J. Sun, B. V. K. J. Schmidt, X. Wang and M. Shalom, *ACS Applied Materials & Interfaces* **9** (3), 2029-2034 (2017).
33. M. Lovrak, W. E. J. Hendriksen, C. Maity, S. Mytnyk, V. van Steijn, R. Eelkema and J. H. van Esch, **8**, 15317 (2017).
34. Z. Yang, D. Shi, M. Chen and S. Liu, *Analytical Methods* **7** (19), 8352-8359 (2015).
35. D. D. Men, F. Zhou, H. L. Li, L. F. Hang, X. Y. Li, D. L. Liu, W. P. Cai, L. M. Qi, L. B. Li and Y. Li, *Journal of Materials Research* **32** (4), 717-725 (2017).
36. W. Lee, C. Y. Bae, S. Kwon, J. Son, J. Kim, Y. Jeong, S.-S. Yoo and J.-K. Park, *Advanced Healthcare Materials* **1** (5), 635-639 (2012).
37. S. Tommaso, M. Federico, T. Alessandro, G. Federico, W. Patrick, M. Paolo and L. Cristina, *Journal of Micromechanics and Microengineering* **22** (10), 105033 (2012).

38. Y.-H. La, B. D. McCloskey, R. Sooriyakumaran, A. Vora, B. Freeman, M. Nassar, J. Hedrick, A. Nelson and R. Allen, *Journal of Membrane Science* **372** (1), 285-291 (2011).
39. J.-Y. Sun, X. Zhao, W. R. K. Illeperuma, O. Chaudhuri, K. H. Oh, D. J. Mooney, J. J. Vlassak and Z. Suo, *Nature* **489** (7414), 133-136 (2012).
40. Z. L. Wu, M. Moshe, J. Greener, H. Therien-Aubin, Z. Nie, E. Sharon and E. Kumacheva, *4*, 1586 (2013).
41. R. F. Roskamp, Johannes Gutenberg-Universität Mainz, 2009.
42. M. J. N. Junk, U. Jonas and D. Hinderberger, *Small* **4** (9), 1485-1493 (2008).
43. M. Toma, U. Jonas, A. Mateescu, W. Knoll and J. Dostalek, *The Journal of Physical Chemistry C* **117** (22), 11705-11712 (2013).
44. I. Anac, A. Aulasevich, M. J. N. Junk, P. Jakubowicz, R. F. Roskamp, B. Menges, U. Jonas and W. Knoll, *Macromolecular Chemistry and Physics* **211** (9), 1018-1025 (2010).
45. J. Dostálek and W. Knoll, in *Polymer Science: A Comprehensive Reference*, edited by M. Möller (Elsevier, Amsterdam, 2012), pp. 647-659.
46. C. R. van den Brom, I. Anac, R. F. Roskamp, M. Retsch, U. Jonas, B. Menges and J. A. Preece, *Journal of Materials Chemistry* **20** (23), 4827-4839 (2010).
47. M. Gianneli, R. F. Roskamp, U. Jonas, B. Loppinet, G. Fytas and W. Knoll, *Soft Matter* **4** (7), 1443-1447 (2008).
48. R. Raccis, R. Roskamp, I. Hopp, B. Menges, K. Koynov, U. Jonas, W. Knoll, H. J. Butt and G. Fytas, *Soft Matter* **7** (15), 7042-7053 (2011).
49. N. Sharma, C. Petri, U. Jonas, M. Bach, G. Tovar, K. Mrkvová, M. Vala, J. Homola, W. Knoll and J. Dostálek, *Macromolecular Chemistry and Physics* **215** (23), 2295-2304 (2014).
50. PolySciences, (2013), Vol. 2017.
51. H. Uedaira and H. Uedaira, *Bulletin of the Chemical Society of Japan* **42**, 2140-2142 (1969).
52. M. Lundqvist, J. Stigler, G. Elia, I. Lynch, T. Cedervall and K. A. Dawson, *Proceedings of the National Academy of Sciences* **105** (38), 14265-14270 (2008).
53. D. Sticker, S. Lechner, C. Jungreuthmayer, J. Zanghellini and P. Ertl, *Analytical Chemistry* **89** (4), 2326-2333 (2017).
54. H. Im, N. J. Wittenberg, A. Lesuffleur, N. C. Lindquist and S.-H. Oh, *Chemical Science* **1** (6), 688-696 (2010).

Supporting information:

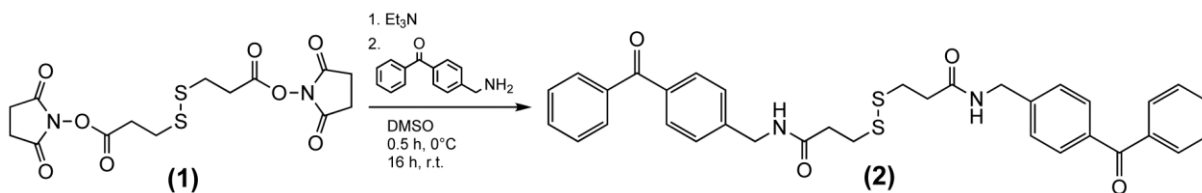


FIG. S1 Bis(2,5-dioxopyrrolidin-1-yl) 3,3'-disulfanediyldipropionate (**1**) reacted with 4-(aminomethyl)benzophenone (4-AMBP) in order to prepare 3,3'-disulfanediyldis(*N*-(4-benzoylbenzyl)propanamide).

¹H NMR (400 MHz, DMSO-*d*₆) δ 8.60 (t, *J* = 6.0 Hz, 1H), 7.76 – 7.62 (m, 5H), 7.55 (t, *J* = 7.6 Hz, 2H), 7.43 (d, *J* = 8.0 Hz, 2H), 4.38 (d, *J* = 5.9 Hz, 2H), 2.96 (t, *J* = 7.1 Hz, 2H), 2.60 (t, *J* = 7.1 Hz, 2H). ¹³C NMR (101 MHz, DMSO-*d*₆) δ 196.67, 171.52, 145.81, 138.41, 136.77, 133.84, 131.06, 130.78, 129.80, 128.42, 43.19, 36.18, 35.13.

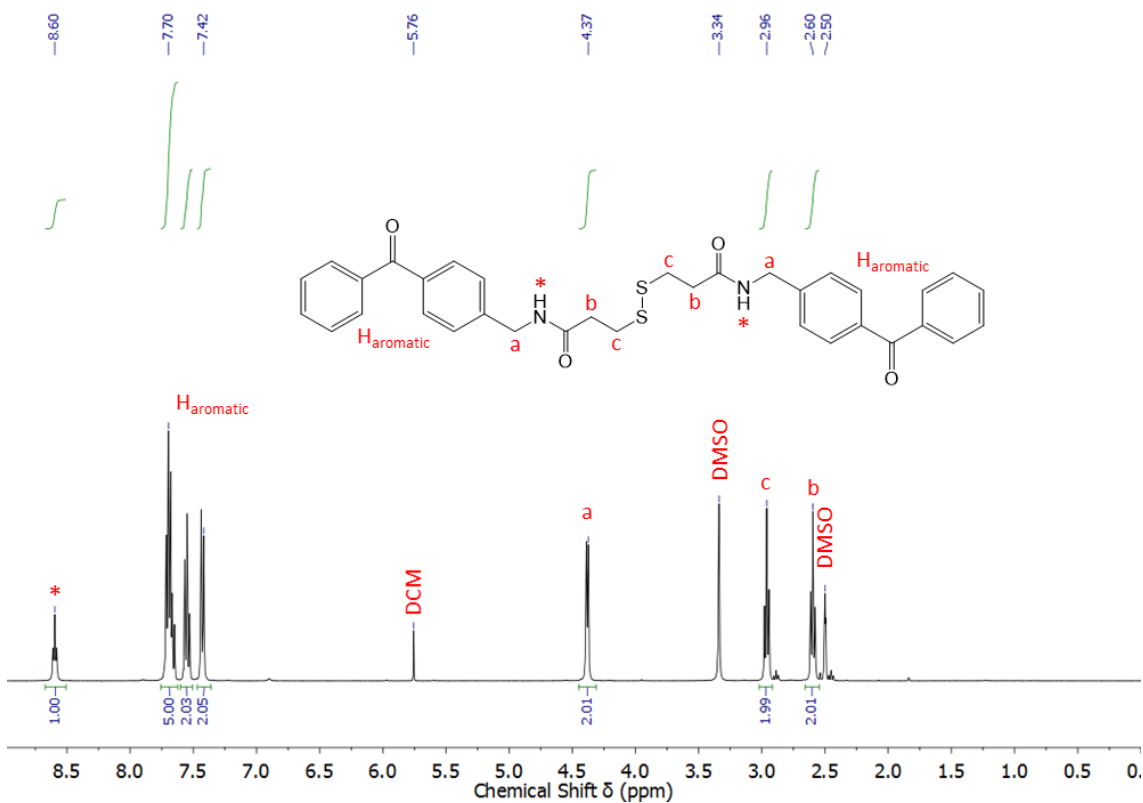


FIG. S2. $^1\text{H-NMR}$ Spectrum of 3,3'-disulfanediylbis(*N*-(4-benzoylbenzyl)propanamide) (recorded in DMSO- d_6).

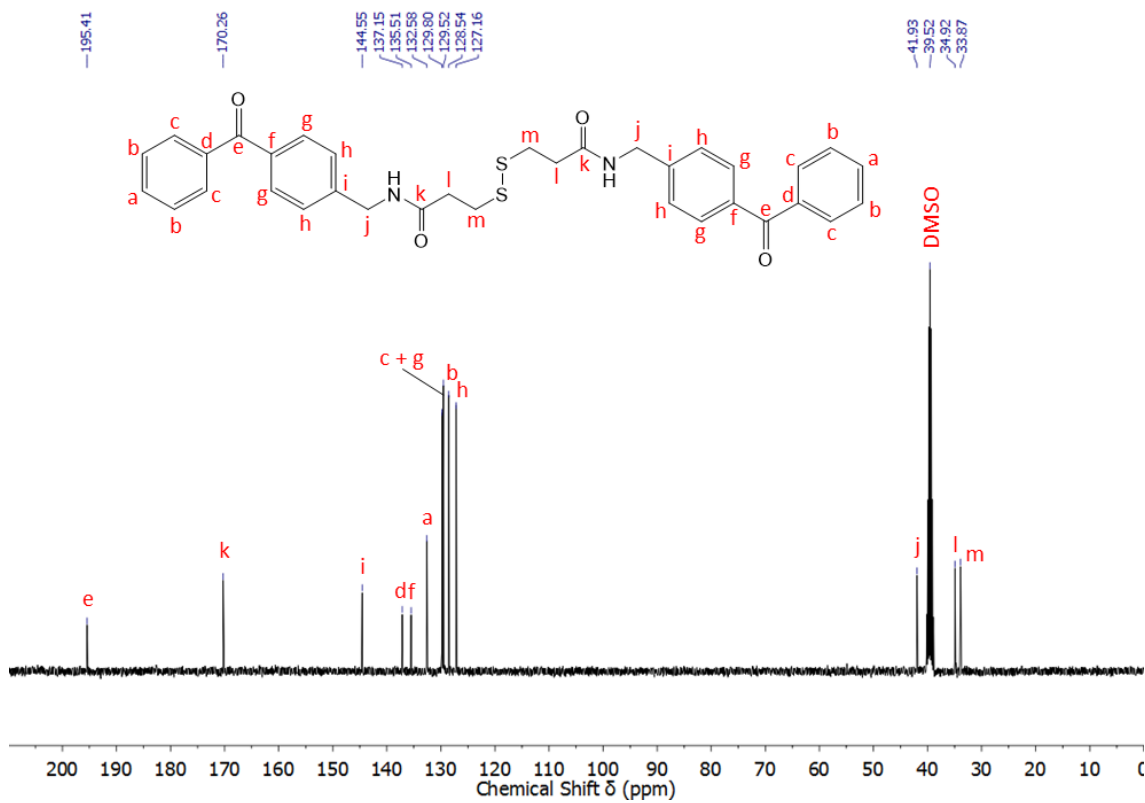


FIG. S3. $^{13}\text{C-NMR}$ Spectrum of 3,3'-disulfanediylbis(*N*-(4-benzoylbenzyl)propanamide) (recorded in DMSO- d_6).

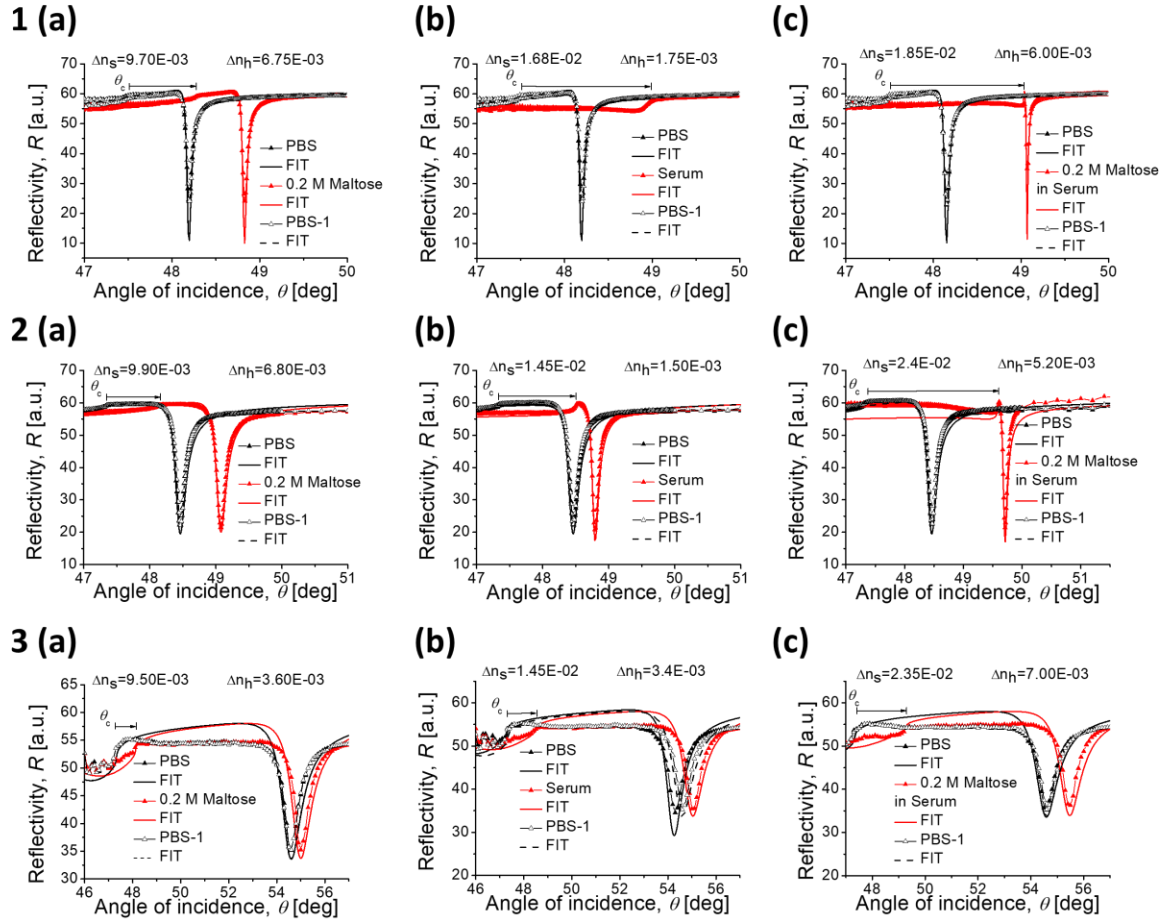


FIG. S4. Examples of measured angular reflectivity spectra of composite films swollen in: (a) 0.2 M maltose in PBS buffer, (b) undiluted serum, and (c) in 0.2 M maltose spiked to undiluted serum. Line connected empty triangles represents spectra measured after washing with PBS. (1) Hydrogel with no nanoparticles. Composites with a PS NP versus hydrogel weight fraction ratio of (2) 0.5 and (3) 5.

7. Enzymatic amplification of fluorescence immunoassay in hydrogel binding matrix

This work was carried out within the frame of European Union's Horizon 2020 research and innovation programme funded project ULTRAPLACAD (ULTRAsensitive PLAsmonic devices for early Cancer Diagnosis) numbered 633937.

Introduction

Many disease biomarkers require highly sensitive detection methods, as they are present in trace amounts [212-214]. Among the many signal transduction methods, fluorescence based sensors offer exceptional sensitivity through signal enhancement strategies [147]. The surface plasmon field-enhanced fluorescence PEF method is demonstrated for ultrasensitive biosensors detecting protein biomarkers [154]. In combination with high binding hydrogel matrix, further improvements of the sensitivity of such sensors were reported [150]. For the commonly used immunoassays applied for such biosensors, the detection antibodies used are usually available with fluorophore dye conjugate of choice. Such antibodies with fluorophores conjugates typically yields 3-5 fluorophore dye per antibody molecule [215] due to the limited availability of reactive groups on the immunoglobulin G molecules. An efficient signal amplification method for fluorescence immunoassays through the enzymatic coupling of fluorophore conjugated reactive tyramide to tyrosine groups has been reported for immunohistochemistry (IHC) [216], fluorescence in-situ hybridization (FISH) [217]. This method allows for localized high density labeling of proteins with fluorophores. Tyramide signal amplification was investigated in microarrays relying on monolayer architecture of immobilized protein ligands [218]. However, the enhancement factor was moderate which could be ascribed to short lifetime of activated fluorophore conjugates and low density of available tyrosine moieties in the 2D architecture. The current chapter pursues the implementation of such amplification strategy in a 3D hydrogel binding matrix that can accommodate higher amounts of ligands with tyrosine moieties and is suitable for the subsequent implementation of surface plasmon field-enhanced fluorescence based detection (Figure 15).

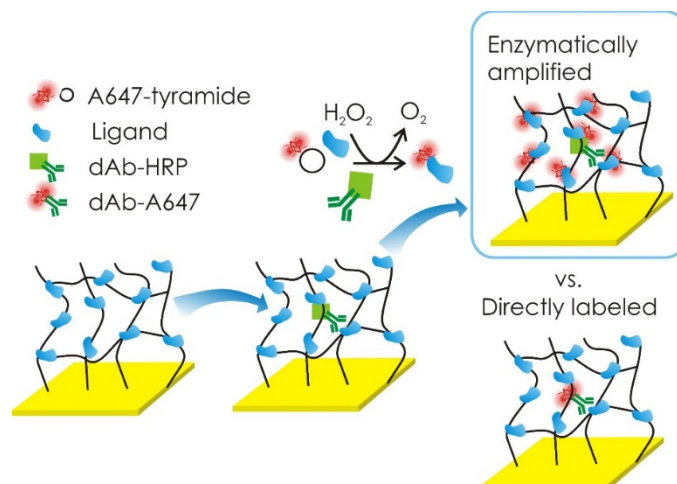


Figure 15: The principle of fluorescence assay that utilizes horseradish peroxidase label and fluorophore-tyramide conjugates for the label-mediated fluorophore attachment on proteins within hydrogel binding matrix in contrast to pre-labeled detection antibody.

Materials and methods

Materials

pNIPAAm-based terpolymer (with 94:5:1 ratio of N-isopropylacrylamide, methacrylic acid, 4-methacroyloxy benzophenone) [211] as well as sodium para-tetrafluorophenolsulfonate (TFPS) [219] and 3,3'-disulfanediylbis(N-(4-benzoylbenzyl)propanamide (4-AMBP-disulfide) [210] were provided by University of Siegen. IgG from mouse serum, 1-Ethyl-3-(3-dimethylaminopropyl)carbodiimide (EDC) and polyethylene glycol sorbitan monolaurate Tween 20 were purchased from Sigma Aldrich (Austria). Goat anti-mouse IgG labelled with AlexaFluor 647 (AF647), Tyramide AlexaFluor 647 (Tyr-AF647) reagent and bovine serum albumin (BSA) were from Invitrogen (USA). Horse radish peroxidase labelled goat anti-mouse IgG and tyramide signal amplification (TSA) 1X Plus amplification reagent were obtained from Perkin Elmer (Austria). Phosphate buffered saline was prepared from PBS tablet (Calbiochem, Germany) in ultrapure water (arium pro, Sartorius Stedim, Germany) to obtain 1X buffer solution (PBS, 140 mM NaCl, 10 mM phosphate, 3 mM KCl, pH=7.4).

Sensor chip preparation

Hydrogel film deposition

BK7 glass substrates (20 X 25 mm) were sequentially washed with 1% Hellmanex III solution, distilled water and absolute ethanol by sonication and dried under stream of air. Subsequently, 2 nm Cr and 50 nm Au were deposited through vacuum thermal evaporation (HHV Auto306 Lab Coater). Gold coated substrates were immersed overnight in 1 mM solution of 4-AMBP-disulfide dissolved in DMSO to allow SAM formation. After rinsing the sensor chips with copious amount of ethanol and drying under stream of air, 2.5 wt% ethanolic solution of pNIPAAm was spin coated at 2000 rpm for 60 seconds. The polymer coated sensor chips were dried overnight at 50 °C under vacuum (Heraeus Vacuum Oven Vt 6025, Thermo Scientific, Austria) and the resulting films were exposed to 365 nm UV light (BLX-E365, Vilber, Germany) with an irradiation dose of 4 J/cm², for both polymer crosslinking and attachment to the gold surface. The non-crosslinked polymer chains were rinsed with ethanol and polymer films were dried before measurements. All steps of the preparation were performed under minimal light exposure.

Characterization of hydrogel films

To characterize the hydrogels and calculate the surface mass density of immobilized ligands, firstly, the thickness (d_{h-dry}) of the dry film and swollen hydrogel matrix d_h and refractive index n_h were determined by the analysis of hydrogel optical waveguides (HOWs) [2]. Reflectivity spectra $R(\theta)$ were analyzed by using the transfer matrix-based model with the software Winspall (MPI for Polymer Research, Germany). Parameters of other layers and materials on the sensor chip were fixed at values taken from literature or from independent measurements. These include BK7 glass $n_{BK7} = 1.845$, chromium $n_{Cr} = 3.1 + 3.3i$ and $d_{Cr} = 2$ nm, gold $n_{Au} = 0.2 + 3.5i$ and $d_{Au} = 50$ nm, 4-AMBP-disulfide SAM $n_{BP-dS} = 1.48$ and $d_{BP-dS} = 1$ nm, dry hydrogel film $n_{h-dry} = 1.48$ and PBS buffer $n_{PBS} = 1.333$. By fitting the reflectivity spectra $R(\theta)$ measured in both TM and TE polarization, the values of hydrogel thicknesses d_{h-dry} , d_h and hydrogel refractive index n_h at swollen states were determined. The swelling ratio (SR) of the hydrogel layers was determined as d_h/d_{h-dry} . The surface mass density of hydrogel before and after ligand (mouse IgG) immobilization was calculated as $\Gamma = (n_h - n_b)d_h\partial c/\partial n_h$, with $\partial c/\partial n_h = 0.2$ mm³/mg, and the resulting difference was ascribed to the surface mass density of immobilized ligand.

Ligand immobilization in hydrogel matrix

A flow-cell with a volume of 10 μL was attached to the sensor surface to contain liquid samples transported via fluidic tubings (Tygon LMT-55) with 0.25 mm inner at 15 $\mu\text{L}/\text{min}$ flow rate. The flow-cell consisted of a PDMS gasket (thickness of 127 μm) and a transparent glass substrate with drilled inlet and outlet ports. Mouse IgG molecules were used as ligand for the (model) immunoassay and immobilized covalently *in situ* using the flow-cell construct. Initially, the hydrogel matrix was allowed to swell in PBS buffer for around 2 hours and reflectivity spectra $R(\theta)$ were measured in both TM and TE polarizations. Next, hydrogel was swollen in acetate buffer (ACT, 10 mM acetate buffer, pH=4) buffer for 30 minutes and then $-\text{COOH}$ groups were activated by injection of 21 mg/mL TFPS and 75 mg/mL EDC aqueous solution for 15 minutes. After washing with ACT buffer briefly for 3 minutes a 50 $\mu\text{g}/\text{mL}$ mIgG (500 μL) in ACT buffer was injected for 60 minutes, to allow for amine groups of the protein to couple to active TPFS ester groups in the hydrogel. The unreacted mIgG molecules were washed with ACT buffer for 3 minutes, followed by injection of 1 M ethanolamine for 15 minutes to passivate the remaining active TFPS ester groups. To determine the thickness and refractive index changes after protein immobilization, the hydrogel was washed with PBS buffer for 5 minutes and $R(\theta)$ were measured.

Detection assay

Fluorescence immunoassays detection were performed with mouse IgG as the ligand and two types of detection antibodies serving as target analyte: a) directly fluorophore-labelled goat anti-mouse IgG and b) horse radish peroxidase (HRP) enzyme-labelled goat anti-mouse IgG along with tyramide-fluorophore conjugate for enzymatic amplified labelling. All antibodies were diluted in series with PBST buffer (assay buffer) and before and after injection of each concentration, the mouse IgG immobilized hydrogel was washed for 5 minutes with assay buffer, followed by fluorescence angular spectrum $F(\theta)$ measurement. In the case of the enzymatically amplified assay, after each detection antibody injection and washing, the tyramide-AF647 conjugate diluted in 1X TSA amplification reagent was injected followed by washing with assay buffer for 5 minutes and fluorescence angular spectra $F(\theta)$ measurements.

Readout of the fluorescence assay

The sensor chip was optically matched to an LASFN9 glass prism with refractive index matching oil. TM or TE polarized beam from a HeNe laser ($\lambda=632.8$ nm) was coupled to a prism in order to excite the hydrogel

waveguide modes by the Kretschmann configuration of ATR method. The prism and sensor chip assembly was placed on a motorized rotating stage and by changing the incident angle θ , the angular reflectivity $R(\theta)$ and fluorescence spectra were recorded. Refractive index (n_h) and thickness (d_h) of hydrogel layers were determined by fitting the measured angular reflectivity spectra using transfer matrix-based model with the software Winspall (MPI for Polymer Research, Mainz, Germany).

The enhanced field intensity occurring upon the resonant coupling to hydrogel waveguide modes excites the Alexa Fluor-647 molecules on the sensor surface. The fluorescence light emitted at wavelength around $\lambda=670$ nm to the direction normal to the surface was collected by an objective lens, made pass through two bandpass filters (transmission wavelength $\lambda=670$ nm, 670FS10-25, Andover Corporation Optical Filter) and a notch filter (central stop-band wavelength $\lambda=632.8$ nm, XNF-632.8-25.0M, CVI Melles Griot), and it was coupled to a multimode optical fiber (FT400EMT, Thorlabs) connected to an avalanche photodiode photon counter (Count-200-FC, Laser Components). The intensity of fluorescence light (F) was measured by a counter (53131A, Agilent) in counts per second (cps) and recorded by the software Wasplas (MPI for Polymer Research, Mainz, Germany).

Results

Immobilization of ligands and characterization of hydrogel matrix

By fitting the angles at which resonant coupling to hydrogel waveguide modes occurs in the measured reflectivity spectra $R(\theta)$, the following thickness and refractive index value ranges were determined for the prepared hydrogel films both in dry and swollen (in PBS buffer) states: $d_{h-dry}=137-143$ nm, $d_h=943-975$ nm and $n_h=1.3554-1.356$. The mean swelling ratio in the swollen state (PBS) was determined to be $SR=6.9 \pm 0.1$. The hydrogel films were prepared so that the thickness of swollen hydrogel films was around $1 \mu\text{m}$, for the purpose of obtaining only one hydrogel waveguide mode, as multiple waveguide modes would complicate the analysis of fluorescence measurements during assay performance. From the calculated surface mass density, Γ values of hydrogel films with and without ligand immobilized, the surface mass density of immobilized mIgG ligand was determined as $\approx 50.6 \pm 1.32$ ng/mm². It is plausible to conclude that the preparation of the sensor chips was consistent and supporting details of the hydrogel characterizations can be found in Table 2.

	n	d, nm	Γ ng/mm ²	mIgG immobilization, Γ_{ligand} ng/mm ²	Swelling ratio
Sample 1					
Dry	1.48	142.7	NA	52	6.83
Swollen	1.356	975	114		
mIgG immobilized	1.3678	944	166		
Sample 2					
Dry	1.48	137		51.1	6.88
Swollen	1.3558	943	109.85		
mIgG immobilized	1.369	882	160.96		
Sample 3					
Dry	1.48	140		50.2	6.82
Swollen	1.3558	956	111.37		
mIgG immobilized	1.3694	876	161.62		
Sample 4					
Dry	1.48	137		48.9	7.05
Swollen	1.3554	966	110.6		
mIgG immobilized	1.3676	909	159.5		
			Mean	50.55	6.89

Table 2. Summary of calculated refractive indices (n_h and $n_{h\text{-dry}}$) and thicknesses (d_h , $d_{h\text{-dry}}$ and d_{mIgG}) of prepared hydrogel films, in dry, swollen and ligand immobilized states, for representative samples. Immobilized ligand concentration, Γ_{ligand} , determined from surface mass densities.

Enzymatically amplified fluorescence immunoassay optimization

The pNIPAAm terpolymer that was used for the preparation of hydrogel binding matrix exhibit a net negative charge, due to the carboxylic acid (-COOH) moieties that serve for covalent immobilization of protein ligands. This charge can be changed upon protein immobilization, mostly depending on the isoelectric point (pI) of the immobilized protein and the pH of buffer solution used. In this case, the immobilized mIgG ligand has a pI around 7.3-8 and PBS buffer (same as in PBST assay buffer) used throughout the immunoassay performance has pH= 7.4. The extent of the change after mIgG immobilization in the hydrogel was not defined, however, the red fluorophores (either detection antibody labelling or tyramide conjugated) available had either net negative (-2 for Alexa Fluor 647) or positive (+1 for Cy5) charges. The effect of these two differently charged fluorophores in terms of Coulombic attraction to the polymer network and their contribution to background fluorescence signal intensity were studied. First, PBST was spiked with of fluorophore labelled (AF647 or Cy5) goat anti-mouse IgG detection antibodies (125 pM) and used in a model fluorescence detection experiment. The affinity binding of

detection antibody resulted in an increase in fluorescence intensity, ΔF_{AF647} and ΔF_{Cy5} from the original values, $F_{0-AF647}$ and F_{0-Cy5} , respectively, measured after the immobilization of ligands in the hydrogel binding matrix. As can be seen in Figure 16, the angular fluorescence spectra exhibit distinct peak at the angle $\theta=47.7$ deg. Further, the peak fluorescence signal is compared for different assays. For 125 pM detection antibody labelled with AF647, ΔF was 2.8×10^4 cps and 1.9×10^4 cps for Cy5 labelled detection antibody, as can be seen in Figure 16. Values for ΔF were obtained by subtracting the $F_{0-AF647}$ and F_{0-Cy5} from labelled antibody binding generated F (peak values of red lines in Figure 16).

Enzymatic amplification fluorescence using HRP activity to activate and bind tyramide fluorophore conjugate to tyrosine residues of the proteins in the near proximity requires a two-step immunoassay protocol, where first the HRP labelled detection antibody is introduced, followed by tyramide fluorophore conjugate in appropriate buffer suited for HRP enzymatic activity. To evaluate the baseline signal for this assay, the tyramide-fluorophore solution is exposed to ligand immobilized hydrogel matrix for 30 minutes, before any HRP labelled detection antibody is injected. After washing with assay buffer, fluorescence angular spectra $F(\theta)$ were measured to determine baselines, $F_{0-Tyr-AF647}$ and $F_{0-Tyr-Cy5}$ (green lines in Figure 16). Further, 125 pM HRP labelled detection antibody is flowed for 30 minutes and after washing with buffer, enzymatic labelling reaction is allowed to occur by flowing tyramide-fluorophore solution for 30 minutes. Finally, the fluorescence angular spectra $F(\theta)$ was measured and the resulting increase in fluorescence signal intensity, $\Delta F_{Tyr-AF647}$ and $\Delta F_{Tyr-Cy5}$, compared to baseline is taken as the tyramide-fluorophore labelling of proteins by enzymatic reaction of bound HRP labelled detection antibody. Baseline fluorescence signal intensity for Tyr-AF647 was 4.47×10^4 cps compared to 6.46×10^5 cps for Tyr-Cy5, was more than ten-fold lower. Regardless of the high baseline $F_{0-Tyr-Cy5}$ for Tyr-Cy5, the $F_{Tyr-Cy5} = 2.52 \times 10^6$ (blue line- right) from specific labelling with enzymatic activity is at comparable level as that of Tyr-AF647, $F_{Tyr-AF647} = 2.34 \times 10^6$ (blue line- left) where baseline was considerably lower $F_{0-Tyr-AF647}$. This leads to the conclusion that positively charged fluorophore (Cy5 +1) is strongly attracted in mIgG immobilized hydrogel matrix, that would disrupt the sensitivity of detection assay by raising background signal intensity. For this reason, throughout the enzymatic amplification assay optimization experiments, the negatively charged fluorophore AF647 (-2) conjugated to tyramide was used.

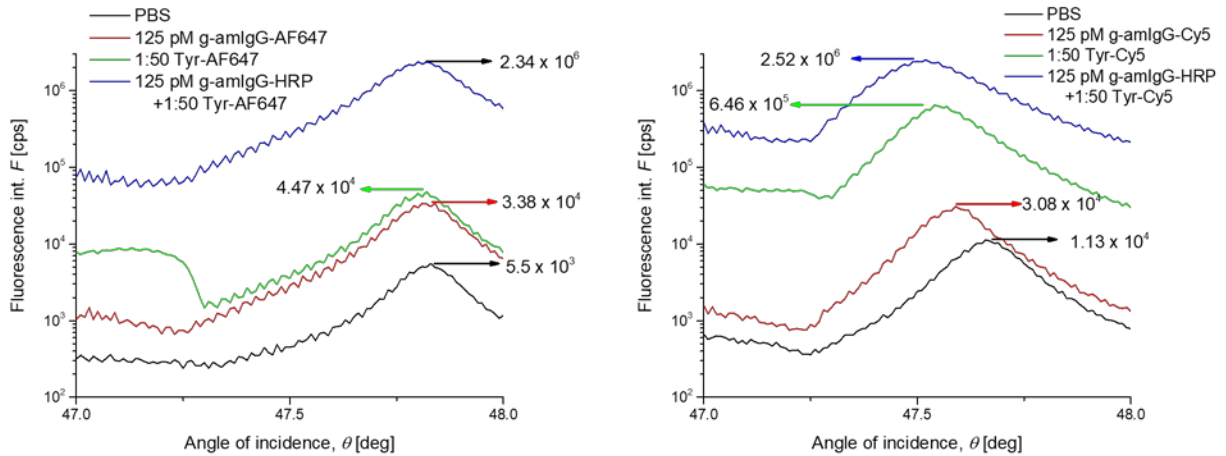


Figure 16. Evaluation of non-specific adsorption of differently charged fluorophore (Left. AF647 -2 and Right. Cy5 +1) tyramide conjugates in ligand immobilized hydrogel matrix. Non-specific adsorption of Tyr-AF647 (Right) to sensor surface is lower compared to and Cy5 (Left) as depicted by the green line.

Commonly used strategy to suppress non-specific adsorption of proteins with a sensor surface immunoassays is to introduce detergents like Tween 20 and blocking reagents like bovine serum albumin BSA. Therefore, 0.05 % Tween 20 and 1 mg/mL BSA was added to PBS buffer used on later experiments. The effect of these components on the reduction of background signal was tested by stabilizing mIgG immobilized hydrogel in PBS or PBST buffer and later exposing to Tyr-AF647 diluted 1:50 in TSA reaction buffer. Sensor surface was first washed and allowed to stabilize in the respective wash buffers (PBS or PBST) for 1 hour, followed by fluorophore exposure for 30 minutes and finally washed for 5 minutes with wash buffer. By comparing the change in signal intensity between fluorescence angular spectra $F(\theta)$ measurements (Figure 17) taken before and after fluorophore exposure, the extent of baseline and background F reduction was evaluated. Tyr-AF647 in PBS and PBST buffers resulted in fluorescence signal intensity increase of $\Delta F_{\text{PBS}} = 4.2 \times 10^4$ cps and $\Delta F_{\text{PBST}} = 2.6 \times 10^4$ cps, respectively. The 1.6-fold decrease in fluorescence signal intensity for PBST in comparison to PBS buffer washing is owed to blocking of the sensor surface. The fluorescence observed at $\theta \approx 47.0$ - 47.3 or critical angle is considered background fluorescence and as it is significantly reduced in PBST (blue line) than PBS (red line), indicating likewise efficient blocking of sensor surrounding surfaces such as flow-cell walls. These results were taken into consideration and henceforth PBST buffer was used as assay buffer for further immunoassay performances.

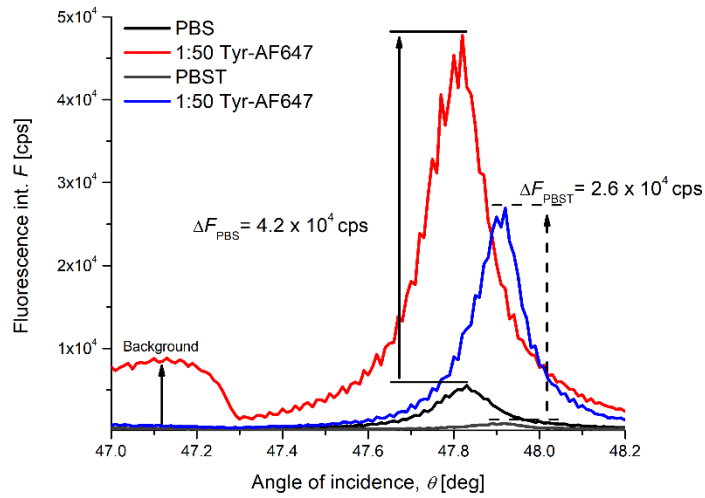


Figure 17. Comparison of buffers PBS and PBST on reducing non-specific adsorption of Tyr-AF647. Fluorescence signal intensity at waveguide mode ($\theta \approx 47.8$ - 47.9) and critical angle ($\theta \approx 47.0$ - 47.3) lower for PBST (difference of grey and blue lines) compared to PBS (difference of black and red lines) buffer suggests less non-specific adsorption. Low F at critical angle indicates low adsorption of fluorophores to flow-cell walls rather than on the sensor surface.

The nature of Tyr-AF647 interaction with sensor surface was studied by exposing it to unmodified or mIgG immobilized hydrogel matrix. Both types of sensor surfaces were stabilized, blocked and washed with assay buffer and Tyr-AF647 diluted 1:50 in TSA reagent buffer was flowed for 30 minutes and washed again with assay buffer. As shown in Figure 18, the unmodified hydrogel matrix showed significantly lower fluorescence signal intensity increase $\Delta F_{\text{unmod}} = 2.4 \times 10^3$ cps compared to 10-fold higher increase for ligand modified hydrogel, $\Delta F_{\text{mIgG}} = 2.6 \times 10^4$ cps. The unmodified, negatively charged hydrogel in buffers with $\text{pH} \approx 7.4$ repels negatively charged AF647 fluorophores (-2) quite effectively, whereas replacing these negatively charged -COOH moieties with mIgG proteins introduces changes in pI that leads to adsorption of the dyes.

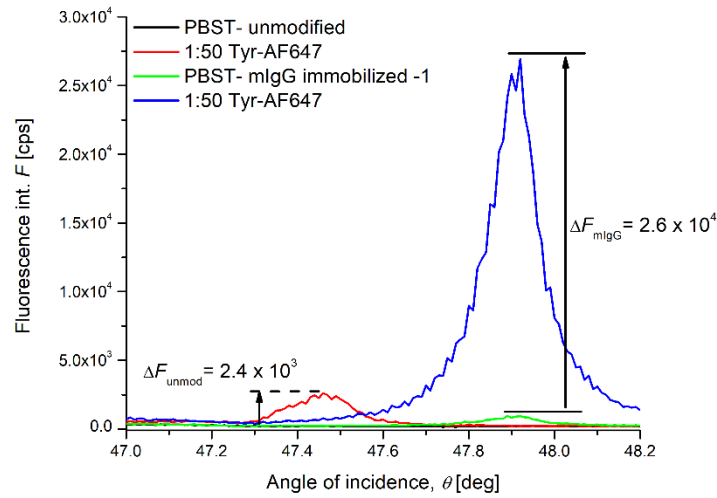


Figure 18. Role of ligand mIgG on Tyr-AF647 adsorption evaluated by comparing unmodified (black and red lines) and mIgG immobilized (green and blue lines) hydrogel matrices.

Next, the duration required for enzymatic reaction to occur was considered for further assay optimization. Two durations of sample exposure were studied, $t_1=15$ and $t_2=30$ minutes, applying to both HRP labelled detection antibody and 1:50 diluted Tyr-AF647. The increase in fluorescence signal intensity resulting from tyramide-AF647 labelling by the 125 pM HRP detection antibody ($C_{g-\alpha\text{mIgG-HRP}}$), is higher in the case of t_2 , $\Delta F_{t_2}= 2.3 \times 10^6$, than t_1 , $\Delta F_{t_1}= 1.8 \times 10^6$ (Figure 19. **Left**). To ensure that this higher fluorescence signal generation is not solely from more detection antibody binding from extended exposure, but also from saturation of enzymatic activity, the Tyr-AF647 fluorophore flowed for a second time for 30 minutes without adding more enzymes. Here, no significant increase in signal intensity can be observed (Figure 19. **Right**), suggesting that 30 minutes is sufficient for Tyr-AF647 labelling.

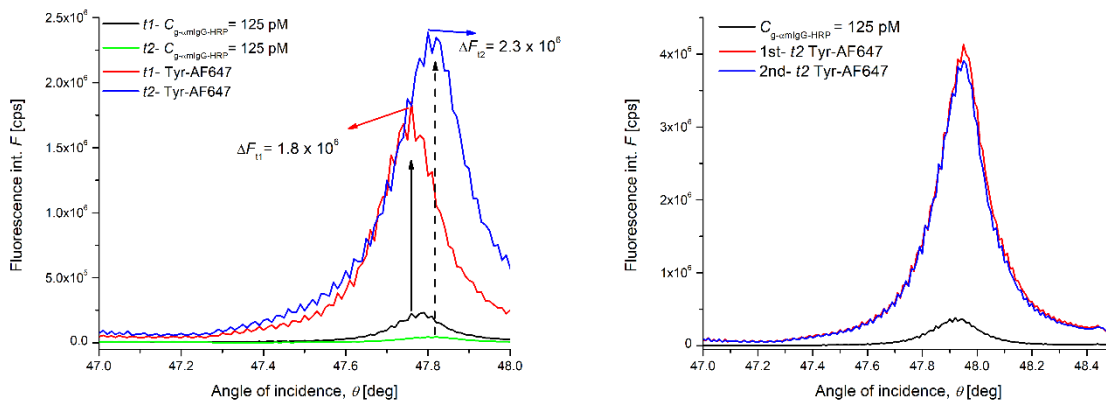


Figure 19. HRP enzyme activity saturation observed by increasing reaction duration (Left) as well as repeated exposure to Tyr-AF647 (Right). $t_1= 15$ minutes, $t_2= 30$ minutes, $C_{g-\alpha m I g G-H R P}= 125$ pM.

With the above-mentioned observations, a protocol was devised to perform the immunoassay involving both directly fluorophore-labelled detection antibody and HRP-amplified Tyr-AF647 post-labelling schemes. All detection antibody binding reaction and washing was performed with PBST buffer and for 30 minutes and 5 minutes, respectively. Enzymatic reaction was allowed to take place for 30 minutes. From a series of detection antibody dilutions, the fluorescence signal intensity increase (ΔF) was recorded and a calibration curve was established. Tyr-AF647 was diluted either 1:50 or 1:500 to observe whether background intensity can be reduced while simultaneously retaining efficiency of labelling. From the established calibration curves (Figure 20. **Left**) for all three detection schemes, directly labelled (black squares), 1:50 (red squares) and 1:500 (blue squares) diluted Tyr-AF647 fluorophores, we can realize upto more than 250-fold enhanced fluorescence signal intensity. The enzymatic amplification efficiency is highest when fluorophore is diluted 1:50. Amplification efficiency is taken as $\Delta F_{1:50 \text{ Tyr-AF647}} / \Delta F_{\text{AF647}}$ or $\Delta F_{1:500 \text{ Tyr-AF647}} / \Delta F_{\text{AF647}}$, comparing to directly fluorophore labelled detection antibody (5 dye/protein). For each calibration curve, the LOD was determined as the concentration at which the calibration curve intersects with the value of the background signal F_0 (dashed lines with colors corresponding to the assay schemes in Figure 20. **Right**). Enzymatic signal amplification assays with $C_{\text{Tyr-AF647}}$ 1:50 or 1:500 both had around 100-180 fM LOD whereas assay performed with AF647 direct labelled detection antibody had 0.5 nM. This translates to around 2.7-5-fold improvement in LOD.

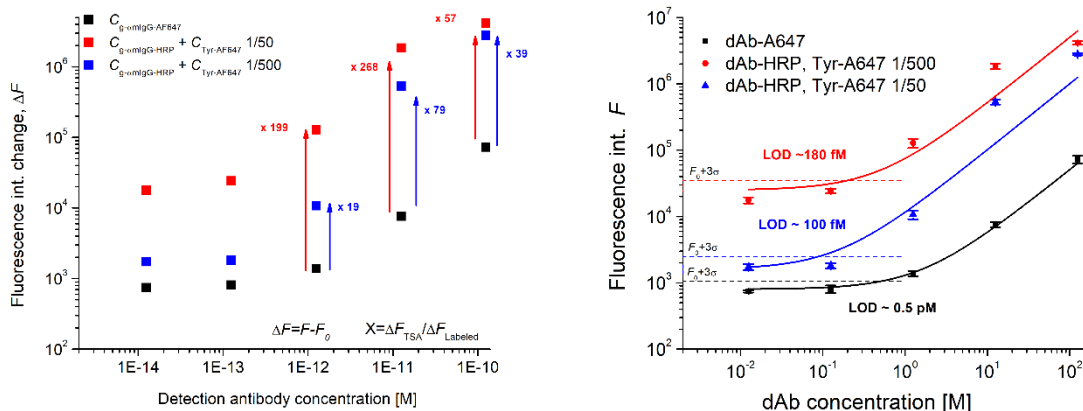


Figure 20. Left. Calibration curve of ΔF from AF647-labeled detection antibody and HRP-antibody generated Tyr-AF647 labelling, and the ratio of the values expressed as signal amplification. Right. Determined LOD of the different assay schemes.

Conclusions

The use of HRP-labelled antibodies in conjunction with catalyzed reaction of tyramide-Alexa Fluor 647 fluorophore conjugates enabled for the enhancement of fluorescence signal and assay LOD by a factor of about 10 with respect to that utilizing antibodies directly labelled with Alexa Fluor 647. This type of chemistry was utilized for immunoassay in a 3D hydrogel binding matrix. In such a surface architecture, IgG ligand with surface mass density of ~ 50 ng/mm² was immobilized which is more than ten times higher value than that for IgG in a 2D monolayer. By using the enzyme amplification, one can estimate that the affinity binding of a target analyte is associated with about 50 fluorophores attached to the surface compared to about 5 for directly labelled detection antibody. The optimization of the amplification protocol to reduce (parasitic) background signal and maximize the (specific) signal associated to the affinity capture of target analyte is presented. The increased background signal clearly relates to the immobilization of ligands rather than to the interaction of fluorophore conjugates with the synthetic hydrogel matrix itself. The charge of used fluorophores plays a major role in the background signal and Alexa Fluor 647 possessing negative charge are preferred compared to Cy5 with positive charge. The enzymatically catalyzed reaction reached saturation in about 15 min for the concentration of Alexa Fluor 647-conjugate of 125 pM and buffer composition PBST (PBS, 0.05% Tween20 and 1 mg/mL BSA). The blocking of the fluidic chamber is essential to minimize parasitic fluorescence signal from unspecifically adsorbed fluorophores to tubing and transparent flow chamber lid.

8. Summary and outlook

Within the scope of this thesis, novel concepts for reversible fluorescence-based biosensors, advanced hydrogel-based biointerfaces and means for amplification of fluorescence signal in sandwich immunoassays were pursued. New aptamer-based surface plasmon-enhanced fluorescence biosensors that reversibly bind low molecular target analyte were developed with a hairpin (Chapter 4) and split aptamer configurations (Chapter 5). The use of responsive hydrogel layers in the form of attached (Chapter 7) or free-standing membranes (Chapter 6) were carried out and the interaction of such structures with biomolecules was performed by the use of optical waveguide spectroscopy and fluorescence correlation spectroscopy. These structures were implemented for sensitive affinity biosensing that took advantage of enzymatically amplified fluorescence spectroscopy readout (chapter 7).

This work successfully demonstrates key functionalities that would need to be combined in a flow through biosensor for the analysis of medically relevant compounds such as drugs with narrow therapeutic range. Therefore, it may provide solid grounds for future development of such type of monitoring systems and e.g. new aptamer ligands for desired analytes identified by the use of SELEX process. Aptamers are suited for low molecular weight compounds and identifying signature structures of aptamers applicable for implementation in SPR-based biosensors is imperative. This thesis described two types of aptamer-based assays (Chapters 4 and 5) in combination with fluorescence readout, however, other schemes of detection assays for medically relevant compounds would need to be explored along with the optical signal enhancement concepts. The aptamer-based low-affinity instigated reversible sensing was seen to compromise the sensitivity of the biosensor slightly, therefore finding the appropriate level of affinity to obtain highest possible sensitivity while still achieving reversible sensing would need to be studied.

Of high importance for the potential future developments of *in vivo* aptamer-based therapeutic drug monitoring optical systems is the protection of the sensing components from the sample matrix, as it should be in contact with blood for an extended time. Considering that, the latter section (Chapters 6 and 7) of the thesis describes the exploitation of hydrogels in different contexts. Specifically, a strategy to introduce a free-standing membrane on an SPR sensor chip was described in chapter 6, that demonstrated the controllable diffusion of molecules of various sizes and very low fouling upon exposure to complex

biological fluid like serum. In chapter 7, the surface attached hydrogel films served to increase the binding capacity in enhanced fluorescence immunoassays. The investigated hydrogel materials can find their applications in advanced microfluidic devices for e.g. cell-on-chip in the emerging field of precision or personalized medicine. This can be greatly complemented by the many new functional properties of hydrogels and improved fabrication techniques for various nano and micro scale structures. The pieces of the carried out work may be used as building blocks for other types of sensor devices that are wearable [220], ingestible [1] or even implantable [221].

Combining the different concepts demonstrated within this thesis opens possibilities for exciting new sensor device constructions. For instance, the aptamer hairpin-based fluorescence assay can be deployed in a hydrogel structure that can be brought in contact with biological fluids such as blood serum [222] and its readout performed through skin [8] in the near infrared spectral window.

References

1. Kalantar-zadeh, K., et al., *Ingestible Sensors*. ACS Sensors, 2017. **2**(4): p. 468-483.
2. *Parkinson's Disease is Ready for Precision Medicine*. Personalized Medicine, 2016. **13**(5): p. 405-407.
3. Rodbard, D., *Continuous Glucose Monitoring: A Review of Successes, Challenges, and Opportunities*. Diabetes Technology & Therapeutics, 2016. **18**(Suppl 2): p. S2-3-S2-13.
4. K., D., *Monitoring Technologies – Continuous Glucose Monitoring, Mobile Technology, Biomarkers of Glycemic Control*. , C.G. De Groot LJ, Dungan K, et al., Editor. 2014 Apr 30, South Dartmouth (MA): MDText.com, Inc.;; Endotext [Internet].
5. Arroyo-Currás, N., et al., *Real-Time Measurement of Small Molecules Directly in Awake, Ambulatory Animals*. Proceedings of the National Academy of Sciences, 2017. **114**(4): p. 645-650.
6. Estevez, M.C., et al., *Trends and Challenges of Refractometric Nanoplasmonic Biosensors: A Review*. Analytica Chimica Acta, 2014. **806**: p. 55-73.
7. Choi, M., et al., *Step-Index Optical Fiber Made of Biocompatible Hydrogels*. Advanced Materials, 2015. **27**(27): p. 4081-4086.
8. Henderson, T.A. and L.D. Morries, *Near-Infrared Photonic Energy Penetration: Can Infrared Phototherapy Effectively Reach the Human Brain?* Neuropsychiatric Disease and Treatment, 2015. **11**: p. 2191-2208.
9. Thevenot, D.R., et al., *Electrochemical Biosensors: Recommended Definitions and Classification*, in *Pure and Applied Chemistry*. 1999. p. 2333.
10. Evtugyn, G., *Biosensors: Essentials*. Lecture Notes In Chemistry. 2014: Springer.
11. Clark, L.C. and C. Lyons, *Electrode Systems for Continuous Monitoring in Cardiovascular Surgery*. Annals of the New York Academy of Sciences, 1962. **102**(1): p. 29-45.
12. Janata, J., *Immuno-electrode*. Journal of the American Chemical Society, 1975. **97**(10): p. 2914-2916.
13. Drummond, T.G., M.G. Hill, and J.K. Barton, *Electrochemical DNA sensors*. Nat Biotech, 2003. **21**(10): p. 1192-1199.
14. James P. Chambers, B.P.A., Leann L. Matta, Alex Weis and James J. Valdes, *Biosensor Recognition Elements*. Curr. Issues Mol. Biol., 2008. **10**: p. 1-12.
15. Grieshaber, D., et al., *Electrochemical Biosensors - Sensor Principles and Architectures*. Sensors (Basel, Switzerland), 2008. **8**(3): p. 1400-1458.
16. Sethi, R.S., *Transducer Aspects of Biosensors*. Biosensors and Bioelectronics, 1994. **9**(3): p. 243-264.
17. Damborský, P., J. Švitel, and J. Katrlík, *Optical Biosensors*. Essays in Biochemistry, 2016. **60**(1): p. 91-100.
18. Borisov, S.M. and O.S. Wolfbeis, *Optical Biosensors*. Chemical Reviews, 2008. **108**(2): p. 423-461.
19. Hammond, Jules L., et al., *Electrochemical Biosensors and Nanobiosensors*. Essays in Biochemistry, 2016. **60**(1): p. 69-80.
20. Ronkainen, N.J., H.B. Halsall, and W.R. Heineman, *Electrochemical Biosensors*. Chemical Society Reviews, 2010. **39**(5): p. 1747-1763.
21. Turner, A.P.F., *Biosensors: Sense and Sensibility*. Chemical Society Reviews, 2013. **42**(8): p. 3184-3196.
22. Bagramyan, K., et al., *Attomolar Detection of Botulinum Toxin Type A in Complex Biological Matrices*. PLOS ONE, 2008. **3**(4): p. e2041.

23. Sreekanth, K.V., et al., *Extreme Sensitivity Biosensing Platform Based on Hyperbolic Metamaterials*. *Nat Mater*, 2016. **15**(6): p. 621-627.
24. Reimhult, E. and F. Höök, *Design of Surface Modifications for Nanoscale Sensor Applications*. *Sensors*, 2015. **15**(1): p. 1635.
25. Aube, A., et al., *Ultra-Low Fouling Methylimidazolium Modified Surfaces for the Detection of HER2 in Breast Cancer Cell Lysates*. *Analyst*, 2017.
26. Masson, J.-F., *Surface Plasmon Resonance Clinical Biosensors for Medical Diagnostics*. *ACS Sensors*, 2017. **2**(1): p. 16-30.
27. Yildirim, N., et al., *Aptamer-Based Optical Biosensor For Rapid and Sensitive Detection of 17 β -Estradiol In Water Samples*. *Environmental Science & Technology*, 2012. **46**(6): p. 3288-3294.
28. Vaisocherová-Lísalová, H., et al., *Low-Fouling Surface Plasmon Resonance Biosensor for Multi-Step Detection of Foodborne Bacterial Pathogens in Complex Food Samples*. *Biosensors and Bioelectronics*, 2016. **80**: p. 84-90.
29. Arulraj, A.D., et al., *Highly Selective and Sensitive Fluorescent Chemosensor for Femtomolar Detection of Silver Ion in Aqueous Medium*. *Sensing and Bio-Sensing Research*, 2015. **6**: p. 19-24.
30. Yu, F., et al., *Attomolar Sensitivity in Bioassays Based on Surface Plasmon Fluorescence Spectroscopy*. *Journal of the American Chemical Society*, 2004. **126**(29): p. 8902-8903.
31. Vance, S.A. and M.G. Sandros, *Zeptomole Detection of C-Reactive Protein in Serum by a Nanoparticle Amplified Surface Plasmon Resonance Imaging Aptasensor*. *Scientific Reports*, 2014. **4**: p. 5129.
32. Lee, K.-L., et al., *Highly Sensitive Aluminum-Based Biosensors using Tailorable Fano Resonances in Capped Nanostructures*. *Scientific Reports*, 2017. **7**: p. 44104.
33. Chang, H., et al., *PSA Detection with Femtomolar Sensitivity and a Broad Dynamic Range Using SERS Nanoprobes and an Area-Scanning Method*. *ACS Sensors*, 2016. **1**(6): p. 645-649.
34. VROMAN, L. and A. LUKOSEVICIUS, *Ellipsometer Recordings of Changes in Optical Thickness of Adsorbed Films associated with Surface Activation of Blood Clotting*. *Nature*, 1964. **204**(4959): p. 701-703.
35. Mahadevan-Jansen, A. and R.R. Richards-Kortum, *Raman Spectroscopy for the Detection of Cancers and Precancers*. *Journal of Biomedical Optics*, 1996. **1**(1): p. 31-70.
36. Kronick, M.N. and W.A. Little, *A New Immunoassay Based on Fluorescence Excitation by Internal Reflection Spectroscopy*. *Journal of Immunological Methods*, 1975. **8**(3): p. 235-240.
37. Knoll, W., *Interfaces and Thin Films as Seen by Bound Electromagnetic Waves*. *Annual Review of Physical Chemistry*, 1998. **49**(1): p. 569-638.
38. Heideman, R.G., R.P.H. Kooyman, and J. Greve, *Performance of a Highly Sensitive Optical Waveguide Mach-Zehnder Interferometer Immunosensor*. *Sensors and Actuators B: Chemical*, 1993. **10**(3): p. 209-217.
39. Vaisocherová, H. and J. Homola, *SPR Biosensors for Medical Diagnostics*, in *Surface Plasmon Resonance Based Sensors*, J. Homola, Editor. 2006, Springer Berlin Heidelberg: Berlin, Heidelberg. p. 229-247.
40. Rich, R.L. and D.G. Myszka, *Advances in Surface Plasmon Resonance Biosensor Analysis*. *Current Opinion in Biotechnology*, 2000. **11**(1): p. 54-61.
41. Liu, Y., et al., *Surface Plasmon Resonance Biosensor Based on Smart Phone Platforms*. *Scientific Reports*, 2015. **5**: p. 12864.
42. Bionavis. Available from: <http://www.bionavis.com/>.
43. Instrument, B.; Available from: <http://biosensingusa.com/>.
44. Scientific, H.
45. Sciences, B.L.

46. Singh, P., *SPR Biosensors: Historical Perspectives and Current Challenges*. Sensors and Actuators B: Chemical, 2016. **229**: p. 110-130.
47. Liedberg, B., C. Nylander, and I. Lunström, *Surface Plasmon Resonance for Gas Detection and Biosensing*. Sensors and Actuators, 1983. **4**: p. 299-304.
48. Zenneck, J., *Über die Fortpflanzung ebener elektromagnetischer Wellen längs einer ebenen Leiterfläche und ihre Beziehung zur drahtlosen Telegraphie*. Annalen der Physik, 1907. **328**(10): p. 846-866.
49. Wood, R.W., *On a Remarkable Case of Uneven Distribution of Light in a Diffraction Grating Spectrum*. Proceedings of the Physical Society of London, 1902. **18**(1): p. 269.
50. Ritchie, R.H., *Plasma Losses by Fast Electrons in Thin Films*. Physical Review, 1957. **106**(5): p. 874-881.
51. Raether, H., *Surface Plasmons on Smooth and Rough Surfaces and on Gratings*. 1988: Springer.
52. Boardman, A.D., *Electromagnetic Surface Modes*. 1982: Wiley.
53. Kretschmann, E. and H. Raether, *Notizen: Radiative Decay of Non Radiative Surface Plasmons Excited by Light*, in *Zeitschrift für Naturforschung A*. 1968. p. 2135.
54. Otto, A., *Excitation of Nonradiative Surface Plasma Waves in Silver by the Method of Frustrated Total Reflection*. Zeitschrift für Physik A Hadrons and nuclei, 1968. **216**(4): p. 398-410.
55. Homola, J. and M. Piliarik, *Surface Plasmon Resonance (SPR) Sensors*, in *Surface Plasmon Resonance Based Sensors*, J. Homola, Editor. 2006, Springer Berlin Heidelberg: Berlin, Heidelberg. p. 45-67.
56. Bog, U., et al., *Design of Plasmonic Grating Structures Towards Optimum Signal Discrimination for Biosensing Applications*. Optics Express, 2012. **20**(10): p. 11357-11369.
57. Lakowicz, J.R., *Introduction to Fluorescence*, in *Principles of Fluorescence Spectroscopy*, J.R. Lakowicz, Editor. 2006, Springer US: Boston, MA. p. 1-26.
58. Dostálek, J. and W. Knoll, *Biosensors Based on Surface Plasmon-Enhanced Fluorescence Spectroscopy (Review)*. Biointerphases, 2008. **3**(3): p. FD12-FD22.
59. Stokes, G.G., *On the Change of Refrangibility of Light*. Philosophical Transactions of the Royal Society of London, 1852. **142**: p. 463-562.
60. Weber, W.H. and C.F. Eagen, *Energy Transfer from an Excited Dye Molecule to the Surface Plasmons of an Adjacent Metal*. Optics Letters, 1979. **4**(8): p. 236-238.
61. Benner, R.E., R. Dornhaus, and R.K. Chang, *Angular Emission Profiles of Dye Molecules Excited by Surface Plasmon Waves at a Metal Surface*. Optics Communications, 1979. **30**(2): p. 145-149.
62. Johnson, P.B. and R.W. Christy, *Optical Constants of the Noble Metals*. Physical Review B, 1972. **6**(12): p. 4370-4379.
63. Bauch, M., *New Enhancement Strategies for Plasmon-Enhanced Fluorescence Biosensors*. 2015, Johannes Gutenberg-Universität: Mainz.
64. Kitson, S.C., et al., *Excitation of Molecular Fluorescence via Surface Plasmon Polaritons*. Journal of Modern Optics, 1996. **43**(3): p. 573-582.
65. Amos, R.M. and W.L. Barnes, *Modification of the Spontaneous Emission Rate of Ions Close to a Thin Metal Mirror*. Physical Review B, 1997. **55**(11): p. 7249-7254.
66. Calander, N., *Theory and Simulation of Surface Plasmon-Coupled Directional Emission from Fluorophores at Planar Structures*. Analytical Chemistry, 2004. **76**(8): p. 2168-2173.
67. Attridge, J.W., et al., *Sensitivity Enhancement of Optical Immunosensors by the Use of a Surface Plasmon Resonance Fluoroimmunoassay*. Biosensors and Bioelectronics, 1991. **6**(3): p. 201-214.
68. Liebermann, T. and W. Knoll, *Surface-Plasmon Field-Enhanced Fluorescence Spectroscopy*. Colloids and Surfaces A: Physicochemical and Engineering Aspects, 2000. **171**(1): p. 115-130.
69. Vasilev, K., et al., *Reduced Photobleaching of Chromophores Close to a Metal Surface*. The Journal of Chemical Physics, 2004. **120**(14): p. 6701-6704.

70. *Energy Transfer*, in *Principles of Fluorescence Spectroscopy*, J.R. Lakowicz, Editor. 2006, Springer US: Boston, MA. p. 443-475.
71. Kooyman, R.P.H., *Chapter 2 Physics of Surface Plasmon Resonance*, in *Handbook of Surface Plasmon Resonance*. 2008, The Royal Society of Chemistry. p. 15-34.
72. Parikh, A.N. and D.L. Allara, *Self-Assembled Monolayers: A Versatile Tool for Biofunctionalization of Surfaces*, in *Handbook of Biofunctional Surfaces*. 2013. p. 1-29.
73. Nelson, K.E., et al., *Surface Characterization of Mixed Self-Assembled Monolayers Designed for Streptavidin Immobilization*. *Langmuir*, 2001. **17**(9): p. 2807-2816.
74. Gedig, E.T., *Chapter 6 Surface Chemistry in SPR Technology*, in *Handbook of Surface Plasmon Resonance*. 2008, The Royal Society of Chemistry. p. 173-220.
75. Jonas, U., et al., *Surface-Attached Polymeric Hydrogel Films*, in *Handbook of Biofunctional Surfaces*. 2013, Pan Stanford Publishing. p. 277-359.
76. Lin, C.-C. and A.T. Metters, *Hydrogels in Controlled Release Formulations: Network Design and Mathematical Modeling*. *Advanced Drug Delivery Reviews*, 2006. **58**(12): p. 1379-1408.
77. Huang, C.J., J. Dostalek, and W. Knoll, *Long Range Surface Plasmon and Hydrogel Optical Waveguide Field-Enhanced Fluorescence Biosensor with 3D Hydrogel Binding Matrix: on the Role of Diffusion Mass Transfer*. *Biosensors & bioelectronics*, 2010. **26**(4): p. 1425-1431.
78. Kuckling, D., M.E. Harmon, and C.W. Frank, *Photo-Cross-Linkable PNIPAAm Copolymers. 1. Synthesis and Characterization of Constrained Temperature-Responsive Hydrogel Layers*. *Macromolecules*, 2002. **35**(16): p. 6377-6383.
79. Vagias, A., et al., *Diffusion and Permeation of Labeled IgG in Grafted Hydrogels*. *Macromolecules*, 2017.
80. Wang, W. and S.A. Sande, *A Dynamic Light Scattering Study of Hydrogels with the Addition of Surfactant: A Discussion of Mesh Size and Correlation Length*. *Polym J*, 2015. **47**(4): p. 302-310.
81. Weber, J. and L. Bergström, *Mesoporous Hydrogels: Revealing Reversible Porosity by Cryoporometry, X-ray Scattering, and Gas Adsorption*. *Langmuir*, 2010. **26**(12): p. 10158-10164.
82. Lee, J.S., et al., *Multifunctional Hydrogel Nano-Probes for Atomic Force Microscopy*. 2016. **7**: p. 11566.
83. Schmaljohann, D., et al., *In Situ Study of the Thermo-responsive Behavior of Micropatterned Hydrogel Films by Imaging Ellipsometry*. *Langmuir*, 2005. **21**(6): p. 2317-2322.
84. Aulasevich, A., et al., *Optical Waveguide Spectroscopy for the Investigation of Protein-Functionalized Hydrogel Films*. *Macromolecular Rapid Communications*, 2009. **30**(9-10): p. 872-877.
85. Beines, P.W., et al., *Responsive Thin Hydrogel Layers from Photo-Cross-Linkable Poly(N-isopropylacrylamide) Terpolymers*. *Langmuir*, 2007. **23**(4): p. 2231-2238.
86. Lieleg, O. and K. Ribbeck, *Biological Hydrogels as Selective Diffusion Barriers*. *Trends in cell biology*, 2011. **21**(9): p. 543-551.
87. Ahmed, A.E.-S.I., *Hydrogels for Water Filters: Characterization and Regeneration*. *Journal of Applied Polymer Science*, 2012. **123**(3): p. 1889-1895.
88. Jung, S.M., et al., *A Facile Methodology for the Production of In Situ Inorganic Nanowire Hydrogels/Aerogels*. *Nano Letters*, 2014. **14**(4): p. 1810-1817.
89. Satarkar, N.S., D. Biswal, and J.Z. Hilt, *Hydrogel Nanocomposites: A Review of Applications as Remote Controlled Biomaterials*. *Soft Matter*, 2010. **6**(11): p. 2364-2371.
90. Thoniyot, P., et al., *Nanoparticle-Hydrogel Composites: Concept, Design, and Applications of These Promising, Multi-Functional Materials*. *Advanced Science*, 2015. **2**(1-2): p. 1400010-n/a.
91. van den Brom, C.R., et al., *The Swelling Behaviour of Thermo-responsive Hydrogel/Silica Nanoparticle Composites*. *Journal of Materials Chemistry*, 2010. **20**(23): p. 4827-4839.

92. Chambers, J.P., et al., *Biosensor Recognition Elements*. *Curr Issues Mol Biol*, 2008. **10**(1-2): p. 1-12.
93. OpenStax, *Anatomy & Physiology*. Jul 30, 2014 OpenStax CNX.
94. Sharma, S., H. Byrne, and Richard J. O'Kennedy, *Antibodies and Antibody-Derived Analytical Biosensors*. *Essays in Biochemistry*, 2016. **60**(1): p. 9-18.
95. Choulier, L. and K. Enander, *Environmentally Sensitive Fluorescent Sensors Based on Synthetic Peptides*. *Sensors*, 2010. **10**(4): p. 3126.
96. Tadepalli, S., et al., *Peptide Functionalized Gold Nanorods for the Sensitive Detection of a Cardiac Biomarker Using Plasmonic Paper Devices*. 2015. **5**: p. 16206.
97. Del Carlo, M., et al., *In Silico Design of Short Peptides as Sensing Elements for Phenolic Compounds*. *ACS Sensors*, 2016. **1**(3): p. 279-286.
98. Haupt, K. and A.-S. Belmont, *Molecularly Imprinted Polymers as Recognition Elements in Sensors*, in *Handbook of Biosensors and Biochips*. 2008, John Wiley & Sons, Ltd.
99. Uzun, L. and A.P.F. Turner, *Molecularly-Imprinted Polymer Sensors: Realising Their Potential*. *Biosensors and Bioelectronics*, 2016. **76**: p. 131-144.
100. Gilbert, W., *Origin Of Life: The RNA World*. *Nature*, 1986. **319**(6055): p. 618-618.
101. Been, M. and T. Cech, *RNA as an RNA Polymerase: Net Elongation of an RNA Primer Catalyzed by the Tetrahymena Ribozyme*. *Science*, 1988. **239**(4846): p. 1412-1416.
102. Ellington, A.D. and J.W. Szostak, *In Vitro Selection of RNA Molecules that Bind Specific Ligands*. *Nature*, 1990. **346**(6287): p. 818-822.
103. Tuerk, C. and L. Gold, *Systematic Evolution of Ligands by Exponential Enrichment: RNA Ligands to Bacteriophage T4 DNA Polymerase*. *Science*, 1990. **249**(4968): p. 505-510.
104. Sassanfar, M. and J.W. Szostak, *An RNA Motif That Binds ATP*. *Nature*, 1993. **364**(6437): p. 550-553.
105. Hermann, T. and D.J. Patel, *Adaptive Recognition by Nucleic Acid Aptamers*. *Science*, 2000. **287**(5454): p. 820-825.
106. Lilley, D.M.J., *The Origins of RNA Catalysis in Ribozymes*. *Trends in Biochemical Sciences*, 2003. **28**(9): p. 495-501.
107. Zinnen, S.P., et al., *Selection, Design, and Characterization of a New Potentially Therapeutic Ribozyme*. *RNA*, 2002. **8**(2): p. 214-228.
108. Bartel, D. and J. Szostak, *Isolation of New Ribozymes from a Large Pool of Random Sequences*. *Science*, 1993. **261**(5127): p. 1411-1418.
109. Reader, J.S. and G.F. Joyce, *A Ribozyme Composed of Only Two Different Nucleotides*. *Nature*, 2002. **420**(6917): p. 841-844.
110. Lin, C.H. and D.J. Patei, *Structural Basis of DNA Folding and Recognition in an AMP-DNA Aptamer Complex: Distinct Architectures but Common Recognition Motifs for DNA and RNA Aptamers Complexed to AMP*. *Chemistry & Biology*, 1997. **4**(11): p. 817-832.
111. Carothers, J.M., et al., *Informational Complexity and Functional Activity of RNA Structures*. *Journal of the American Chemical Society*, 2004. **126**(16): p. 5130-5137.
112. Carothers, J.M., S.C. Oestreich, and J.W. Szostak, *Aptamers Selected for Higher-Affinity Binding are not More Specific for the Target Ligand*. *Journal of the American Chemical Society*, 2006. **128**(24): p. 7929-7937.
113. and, D.S.W. and J.W. Szostak, *In Vitro Selection of Functional Nucleic Acids*. *Annual Review of Biochemistry*, 1999. **68**(1): p. 611-647.
114. Jenison, R., et al., *High-Resolution Molecular Discrimination by RNA*. *Science*, 1994. **263**(5152): p. 1425-1429.

115. Dobbelstein, M. and T. Shenk, *In Vitro Selection of RNA Ligands for the Ribosomal L22 Protein Associated with Epstein-Barr Virus-Expressed RNA by using Randomized and cDNA-Derived RNA Libraries*. *Journal of Virology*, 1995. **69**(12): p. 8027-8034.
116. Stoltenburg, R., C. Reinemann, and B. Strehlitz, *SELEX—A (r)evolutionary Method to Generate High-Affinity Nucleic Acid Ligands*. *Biomolecular Engineering*, 2007. **24**(4): p. 381-403.
117. Nguyen, V.-T., et al., *Multiple GO-SELEX for Efficient Screening of Flexible Aptamers*. *Chemical Communications*, 2014. **50**(72): p. 10513-10516.
118. Reid, D.C., et al., *Next-Generation SELEX Identifies Sequence and Structural Determinants of Splicing Factor Binding in Human Pre-mRNA Sequence*. *RNA*, 2009. **15**(12): p. 2385-2397.
119. Schütze, T., et al., *Probing the SELEX Process with Next-Generation Sequencing*. *PLOS ONE*, 2011. **6**(12): p. e29604.
120. Tyagi, S. and F.R. Kramer, *Molecular Beacons: Probes that Fluoresce upon Hybridization*. *Nat Biotech*, 1996. **14**(3): p. 303-308.
121. Zhang, H., et al., *Universal Fluorescence Biosensor Platform Based on Graphene Quantum Dots and Pyrene-Functionalized Molecular Beacons for Detection of MicroRNAs*. *ACS Applied Materials & Interfaces*, 2015. **7**(30): p. 16152-16156.
122. Jeddi, I. and L. Saiz, *Three-Dimensional Modeling of Single Stranded DNA Hairpins for Aptamer-Based Biosensors*. *Scientific Reports*, 2017. **7**(1): p. 1178.
123. Zhou, W., et al., *Aptamer-Based Biosensors for Biomedical Diagnostics*. *Analyst*, 2014. **139**(11): p. 2627-2640.
124. Nguyen, V.-T., Y.S. Kwon, and M.B. Gu, *Aptamer-Based Environmental Biosensors for Small Molecule Contaminants*. *Current Opinion in Biotechnology*, 2017. **45**: p. 15-23.
125. Keefe, A.D., S. Pai, and A. Ellington, *Aptamers as Therapeutics*. *Nat Rev Drug Discov*, 2010. **9**(7): p. 537-550.
126. Aliakbarinodehi, N., et al., *Aptamer-based Field-Effect Biosensor for Tenofovir Detection*. 2017. **7**: p. 44409.
127. Ferguson, B.S., et al., *Real-Time, Aptamer-Based Tracking of Circulating Therapeutic Agents in Living Animals*. *Science translational medicine*, 2013. **5**(213): p. 213ra165-213ra165.
128. Shin, S.R., et al., *Aptamer-Based Microfluidic Electrochemical Biosensor for Monitoring Cell-Secreted Trace Cardiac Biomarkers*. *Analytical Chemistry*, 2016. **88**(20): p. 10019-10027.
129. Lee, S.E., et al., *Reversible Aptamer-Au Plasmon Rulers for Secreted Single Molecules*. *Nano Letters*, 2015. **15**(7): p. 4564-4570.
130. Kausaite-Minkstiniene, A., A. Ramanaviciene, and A. Ramanavicius, *Surface Plasmon Resonance Biosensor for Direct Detection of Antibodies against Human Growth Hormone*. *Analyst*, 2009. **134**(10): p. 2051-2057.
131. Matveeva, E.G., et al., *Directional Surface Plasmon-Coupled Emission: Application for an Immunoassay in Whole Blood*. *Analytical Biochemistry*, 2005. **344**(2): p. 161-167.
132. Sharma, N., et al., *Molecularly Imprinted Polymer Waveguides for Direct Optical Detection of Low-Molecular-Weight Analytes*. *Macromolecular Chemistry and Physics*, 2014. **215**(23): p. 2295-2304.
133. Gomes, P. and D. Andreu, *Direct Kinetic Assay of Interactions Between Small Peptides and Immobilized Antibodies using a Surface Plasmon Resonance Biosensor*. *Journal of Immunological Methods*, 2002. **259**(1): p. 217-230.
134. Sun, L., L. Wu, and Q. Zhao, *Aptamer Based Surface Plasmon Resonance Sensor for Aflatoxin B1*. *Microchimica Acta*, 2017: p. 1-6.
135. Zeng, S., et al., *Nanomaterials Enhanced Surface Plasmon Resonance for Biological and Chemical Sensing Applications*. *Chemical Society Reviews*, 2014. **43**(10): p. 3426-3452.

136. Wang, S., et al., *An Improved Label-Free Indirect Competitive SPR Immunosensor and Its Comparison with Conventional ELISA for Ractopamine Detection in Swine Urine*. *Sensors*, 2017. **17**(3): p. 604.
137. Wang, J., A. Munir, and H.S. Zhou, *Au NPs-Aptamer Conjugates as a Powerful Competitive Reagent for Ultrasensitive Detection of Small Molecules by Surface Plasmon Resonance Spectroscopy*. *Talanta*, 2009. **79**(1): p. 72-76.
138. Carrasco, S., et al., *Fiber-Optic Array using Molecularly Imprinted Microspheres for Antibiotic Analysis*. *Chemical Science*, 2015. **6**(5): p. 3139-3147.
139. Wang, J., et al., *Aptamer–Au NPs Conjugates-Enhanced SPR Sensing for the Ultrasensitive Sandwich Immunoassay*. *Biosensors and Bioelectronics*, 2009. **25**(1): p. 124-129.
140. Guo, L. and D.-H. Kim, *LSPR Biomolecular Assay with High Sensitivity Induced by Aptamer–Antigen–Antibody Sandwich Complex*. *Biosensors and Bioelectronics*, 2012. **31**(1): p. 567-570.
141. Chen, H., et al., *Detection of Vascular Endothelial Growth Factor based on Rolling Circle Amplification as a Means of Signal Enhancement in Surface Plasmon Resonance*. *Biosensors and Bioelectronics*, 2014. **61**: p. 83-87.
142. Nguyen, V.-T., et al., *Highly Sensitive Sandwich-Type SPR Based Detection of Whole H5N Viruses using a Pair of Aptamers*. *Biosensors and Bioelectronics*, 2016. **86**: p. 293-300.
143. Zeidan, E., et al., *Nano-SPRi Aptasensor for the Detection of Progesterone in Buffer*. 2016. **6**: p. 26714.
144. Melaine, F., Y. Roupioz, and A. Buhot, *Gold Nanoparticles Surface Plasmon Resonance Enhanced Signal for the Detection of Small Molecules on Split-Aptamer Microarrays (Small Molecules Detection from Split-Aptamers)*. *Microarrays*, 2015. **4**(1): p. 41.
145. Aslan, K., et al., *Metal-Enhanced Fluorescence: An Emerging Tool in Biotechnology*. *Current Opinion in Biotechnology*, 2005. **16**(1): p. 55-62.
146. Gryczynski, I., et al., *Surface Plasmon-Coupled Emission with Gold Films*. *The Journal of Physical Chemistry B*, 2004. **108**(33): p. 12568-12574.
147. Bauch, M., et al., *Plasmon-Enhanced Fluorescence Biosensors: a Review*. *Plasmonics*, 2014. **9**(4): p. 781-799.
148. Huang, C.-J., et al., *Long-Range Surface Plasmon-Enhanced Fluorescence Spectroscopy Biosensor for Ultrasensitive Detection of E. coli O157:H7*. *Analytical Chemistry*, 2011. **83**(3): p. 674-677.
149. Wang, Y., J. Dostálek, and W. Knoll, *Long Range Surface Plasmon-Enhanced Fluorescence Spectroscopy for the Detection of Aflatoxin M1 in Milk*. *Biosensors and Bioelectronics*, 2009. **24**(7): p. 2264-2267.
150. Wang, Y., et al., *Prostate Specific Antigen Biosensor Based on Long Range Surface Plasmon-Enhanced Fluorescence Spectroscopy and Dextran Hydrogel Binding Matrix*. *Analytical Chemistry*, 2009. **81**(23): p. 9625-9632.
151. Black, M.H., et al., *Serum Total and Free Prostate-specific Antigen for Breast Cancer Diagnosis in Women*. *Clinical Cancer Research*, 2000. **6**(2): p. 467-473.
152. Barry, M.J., *Prostate-Specific–Antigen Testing for Early Diagnosis of Prostate Cancer*. *New England Journal of Medicine*, 2001. **344**(18): p. 1373-1377.
153. Healy, D.A., et al., *Biosensor Developments: Application to Prostate-Specific Antigen Detection*. *Trends in Biotechnology*. **25**(3): p. 125-131.
154. Chang, Y.-F., et al., *Discrimination of Breast Cancer by Measuring Prostate-Specific Antigen Levels in Women's Serum*. *Analytical Chemistry*, 2011. **83**(13): p. 5324-5328.
155. Kaya, T., et al., *High-Sensitivity Immunoassay with Surface Plasmon Field-Enhanced Fluorescence Spectroscopy Using a Plastic Sensor Chip: Application to Quantitative Analysis of Total Prostate-Specific Antigen and GalNAc β 1–4GlcNAc-Linked Prostate-Specific Antigen for Prostate Cancer Diagnosis*. *Analytical Chemistry*, 2015. **87**(3): p. 1797-1803.

156. Chabot, V., et al., *Identification of the Molecular Mechanisms in Cellular Processes that Elicit a Surface Plasmon Resonance (SPR) Response using Simultaneous Surface Plasmon-Enhanced Fluorescence (SPEF) Microscopy*. Biosensors and Bioelectronics, 2013. **50**: p. 125-131.
157. Bauch, M., S. Hageneder, and J. Dostalek, *Plasmonic Amplification for Bioassays with Epi-Fluorescence Readout*. Optics Express, 2014. **22**(26): p. 32026-32038.
158. Toma, M. and K. Tawa, *Polydopamine Thin Films as Protein Linker Layer for Sensitive Detection of Interleukin-6 by Surface Plasmon Enhanced Fluorescence Spectroscopy*. ACS Applied Materials & Interfaces, 2016. **8**(34): p. 22032-22038.
159. Toma, K., et al., *Compact Surface Plasmon-Enhanced Fluorescence Biochip*. Optics Express, 2013. **21**(8): p. 10121-10132.
160. Zhang, Q., et al., *Surface Plasmon-Enhanced Fluorescence on Au Nanohole Array for Prostate-Specific Antigen Detection*. International Journal of Nanomedicine, 2017. **12**: p. 2307-2314.
161. Yuan, B., et al., *Plasmon-Enhanced Fluorescence Imaging with Silicon-Based Silver Chips for Protein and Nucleic Acid Assay*. Analytica Chimica Acta, 2017. **955**: p. 98-107.
162. Ashiba, H., et al., *Detection of Norovirus Virus-like Particles Using a Surface Plasmon Resonance-assisted Fluoroimmunosensor Optimized for Quantum Dot Fluorescent Labels*. Biosensors and Bioelectronics, 2017. **93**: p. 260-266.
163. Chen, L. and S. Neethirajan, *A Homogenous Fluorescence Quenching Based Assay for Specific and Sensitive Detection of Influenza Virus A Hemagglutinin Antigen*. Sensors, 2015. **15**(4): p. 8852.
164. Lee, J., et al., *A Plasmon-Assisted Fluoro-Immunoassay using Gold Nanoparticle-Decorated Carbon Nanotubes for Monitoring the Influenza Virus*. Biosensors and Bioelectronics, 2015. **64**: p. 311-317.
165. Liu, J.-M., J.-T. Chen, and X.-P. Yan, *Near Infrared Fluorescent Trypsin Stabilized Gold Nanoclusters as Surface Plasmon Enhanced Energy Transfer Biosensor and in Vivo Cancer Imaging Bioprobe*. Analytical Chemistry, 2013. **85**(6): p. 3238-3245.
166. Wang, L., et al., *Plasmon-Enhanced Fluorescence-Based Core-Shell Gold Nanorods as a Near-IR Fluorescent Turn-On Sensor for the Highly Sensitive Detection of Pyrophosphate in Aqueous Solution*. Advanced Functional Materials, 2015. **25**(45): p. 7017-7027.
167. Niu, C., et al., *Near-Infrared-Fluorescent Probes for Bioapplications Based on Silica-Coated Gold Nanobipyramids with Distance-Dependent Plasmon-Enhanced Fluorescence*. Analytical Chemistry, 2016. **88**(22): p. 11062-11069.
168. Appiah-Ntiamoah, R., A. Chinnappan, and H. Kim, *A Facile Method to Effectively Combine Plasmon Enhanced Fluorescence (PEF) and Fluoride-Lewis Acid Based Reactions to Detect Low Concentrations of Fluoride in Solution*. RSC Advances, 2016. **6**(82): p. 78918-78929.
169. Sun, B., et al., *Metal-Enhanced Fluorescence-Based Multilayer Core-Shell Ag-Nanocube@SiO₂@PMOs Nanocomposite Sensor for Cu²⁺ Detection*. RSC Advances, 2016. **6**(66): p. 61109-61118.
170. Obliosca, J.M., P.-C. Wang, and F.-G. Tseng, *Probing Quenched Dye Fluorescence of Cy3-DNA-Au-Nanoparticle Hybrid Conjugates using Solution and Array Platforms*. Journal of Colloid and Interface Science, 2012. **371**(1): p. 34-41.
171. Shen, J., C. Sun, and X. Wu, *Silver Nanoprisms-Based Tb(III) Fluorescence Sensor for Highly Selective Detection of Dopamine*. Talanta, 2017. **165**: p. 369-376.
172. Lu, L., X. An, and W. Huang, *Quantitative Determination of Calcium Ions by Means of Enhanced Fluorescence of Silver Nanocluster Complex*. Analytical Methods, 2017. **9**(1): p. 23-27.
173. Asselin, J., et al., *A Ratiometric Nanoarchitecture for the Simultaneous Detection of pH and Halide Ions using UV Plasmon-enhanced Fluorescence*. Chemical Communications, 2017. **53**(4): p. 755-758.

174. Nöll, G., et al., *A Reusable Sensor for the Label-Free Detection of Specific Oligonucleotides by Surface Plasmon Fluorescence Spectroscopy*. *Advanced Healthcare Materials*, 2014. **3**(1): p. 42-46.
175. Su, Q. and G. Noll, *A Sandwich-Like Strategy for the Label-Free Detection of Oligonucleotides by Surface Plasmon Fluorescence Spectroscopy (SPFS)*. *Analyst*, 2016. **141**(20): p. 5784-5791.
176. Mei, Z. and L. Tang, *Surface-Plasmon-Coupled Fluorescence Enhancement Based on Ordered Gold Nanorod Array Biochip for Ultrasensitive DNA Analysis*. *Analytical Chemistry*, 2017. **89**(1): p. 633-639.
177. Darvill, D., A. Centeno, and F. Xie, *Plasmonic Fluorescence Enhancement by Metal Nanostructures: Shaping the Future of Bionanotechnology*. *Physical Chemistry Chemical Physics*, 2013. **15**(38): p. 15709-15726.
178. Lin, R., et al., *Metal-Enhanced Fluorescence in Biosensing Applications*, in *Surface Plasmon Enhanced, Coupled and Controlled Fluorescence*. 2017, John Wiley & Sons, Inc. p. 121-136.
179. Ohlson, S., et al., *Continuous Weak-Affinity Immunosensing*. *Trends in Biotechnology*, 2000. **18**(2): p. 49-52.
180. O'Sullivan, C.K., *Aptasensors – The Future of Biosensing?* *Analytical and Bioanalytical Chemistry*, 2002. **372**(1): p. 44-48.
181. Wang, R.E., et al., *Aptamer-Based Fluorescent Biosensors*. *Current medicinal chemistry*, 2011. **18**(27): p. 4175-4184.
182. Zhang, H., et al., *Fluorescent Biosensors Enabled by Graphene and Graphene Oxide*. *Biosensors and Bioelectronics*, 2017. **89**, Part 1: p. 96-106.
183. Lu, D., et al., *Aptamer-Assembled Nanomaterials for Fluorescent Sensing and Imaging*, in *Nanophotonics*. 2017. p. 109.
184. Turcheniuk, K., R. Boukherroub, and S. Szunerits, *Gold-Graphene Nanocomposites for Sensing and Biomedical Applications*. *Journal of Materials Chemistry B*, 2015. **3**(21): p. 4301-4324.
185. Justino, C.I.L., et al., *Graphene Based Sensors and Biosensors*. *TrAC Trends in Analytical Chemistry*, 2017. **91**: p. 53-66.
186. Shi, J., et al., *A Fluorescence Turn-on Biosensor Based on Graphene Quantum Dots (GQDs) and Molybdenum Disulfide (MoS₂) Nanosheets for Epithelial Cell Adhesion Molecule (EpCAM) Detection*. *Biosensors and Bioelectronics*, 2017. **93**: p. 182-188.
187. Joo, M., et al., *Development of Aflatoxin B1 Aptasensor Based on Wide-Range Fluorescence Detection using Graphene Oxide Quencher*. *Colloids and Surfaces B: Biointerfaces*, 2017. **154**: p. 27-32.
188. Ning, Y., et al., *Fluorometric Aptamer Based Determination of Adenosine Triphosphate Based on Deoxyribonuclease I-Aided Target Recycling and Signal Amplification using Graphene Oxide as a Quencher*. *Microchimica Acta*, 2017. **184**(6): p. 1847-1854.
189. Hu, L.-Y., et al., *Magnetic Separate "Turn-On" Fluorescent Biosensor for Bisphenol A Based on Magnetic Oxidation Graphene*. *Talanta*, 2017. **168**: p. 196-202.
190. Liu, Z., et al., *Intracellular Detection of ATP Using an Aptamer Beacon Covalently Linked to Graphene Oxide Resisting Nonspecific Probe Displacement*. *Analytical Chemistry*, 2014. **86**(24): p. 12229-12235.
191. Gao, L., et al., *Graphene Oxide–DNA Based Sensors*. *Biosensors and Bioelectronics*, 2014. **60**: p. 22-29.
192. Tan, D., et al., *Aptamer Functionalized Gold Nanoparticles Based Fluorescent Probe for the Detection of Mercury (II) Ion in Aqueous Solution*. *Talanta*, 2013. **113**: p. 26-30.
193. Lu, L., et al., *Metal-Enhanced Fluorescence-Based Core–Shell Ag@SiO₂ Nanoflares for Affinity Biosensing via Target-Induced Structure Switching of Aptamer*. *ACS Applied Materials & Interfaces*, 2014. **6**(3): p. 1944-1950.

194. Chen, Z., et al., *Bivalent Aptasensor Based on Silver-Enhanced Fluorescence Polarization for Rapid Detection of Lactoferrin in Milk*. *Analytical Chemistry*, 2017. **89**(11): p. 5900-5908.
195. Song, H.Y., et al., *Nanoimprinted Thrombin Aptasensor with Picomolar Sensitivity Based on Plasmon Excited Quantum Dots*. *Sensors and Actuators B: Chemical*, 2015. **221**: p. 207-216.
196. Chen, X., et al., *Fluorescent Aptasensor for Adenosine based on the use of Quaternary CuInZnS Quantum Dots and Gold Nanoparticles*. *Microchimica Acta*, 2017. **184**(5): p. 1361-1367.
197. Guler, E., et al., *An Aptamer Folding-Based Sensory Platform Decorated with Nanoparticles for Simple Cocaine Testing*. *Drug Testing and Analysis*, 2017. **9**(4): p. 578-587.
198. Xie, T.-T., et al., *Surface Plasmon-Coupled Directional Emission Based on a Conformational-Switching Signaling Aptamer*. *Chemical Communications*, 2009(22): p. 3190-3192.
199. Cao, S.-H., et al., *Label-Free Aptasensor Based on Ultrathin-Linker-Mediated Hot-Spot Assembly To Induce Strong Directional Fluorescence*. *Journal of the American Chemical Society*, 2014. **136**(19): p. 6802-6805.
200. Sergelen, K., et al., *Plasmon Field-Enhanced Fluorescence Energy Transfer for Hairpin Aptamer Assay Readout*. *ACS Sensors*, 2017.
201. Dasgupta, A., *Chapter 1 - Introduction to Therapeutic Drug Monitoring: Frequently and Less Frequently Monitored Drugs*, in *Therapeutic Drug Monitoring*. 2012, Academic Press: Boston. p. 1-29.
202. Milone, M.C., *Chapter 3 - Analytical Techniques used in Therapeutic Drug Monitoring A2 - Dasgupta, Amitava*, in *Therapeutic Drug Monitoring*. 2012, Academic Press: Boston. p. 49-73.
203. Bush, V., *Chapter 2 - Effects of Pre-analytical Variables in Therapeutic Drug Monitoring A2 - Dasgupta, Amitava*, in *Therapeutic Drug Monitoring*. 2012, Academic Press: Boston. p. 31-48.
204. McKeating, K.S., A. Aube, and J.-F. Masson, *Biosensors and Nanobiosensors for Therapeutic Drug and Response Monitoring*. *Analyst*, 2016. **141**(2): p. 429-449.
205. Jean-Francois Masson, J.N.P., *Will Nanobiosensors Change Therapeutic Drug Monitoring? The Case of Methotrexate*. *Nanomedicine*, 2015. **10**(4): p. 521-524.
206. Vieira, P.A., et al., *Real-Time, Continuous Electrochemical Monitoring of Therapeutic Drugs In Vivo*. *The FASEB Journal*, 2016. **30**(1 Supplement): p. 938.8.
207. Yockell-Lelievre, H., et al., *Naked-Eye Nanobiosensor for Therapeutic Drug Monitoring of Methotrexate*. *Analyst*, 2016. **141**(2): p. 697-703.
208. Breault-Turcot, J. and J.-F. Masson, *Microdialysis SPR: Diffusion-Gated Sensing in Blood*. *Chemical Science*, 2015. **6**(7): p. 4247-4254.
209. Dostalek, J., Y. Wang, and C. Huang, *Evanescent Wave Biosensors with a Hydrogel Binding Matrix*, in *Handbook of Biofunctional Surfaces*. 2013, Pan Stanford Publishing. p. 361-406.
210. Roskamp, R.F., *Functional Hydrogels*. 2009, Johannes Gutenberg-Universitaet Mainz.
211. Aulasevich, A., et al., *Macromol. Rapid Commun. 9-10/2009*. *Macromolecular Rapid Communications*, 2009. **30**(9-10): p. n/a-n/a.
212. Chan, H.-N., et al., *Ultra-Sensitive Detection of Protein Biomarkers for Diagnosis of Alzheimer's Disease*. *Chemical Science*, 2017. **8**(5): p. 4012-4018.
213. Schubert, S.M., et al., *Ultra-Sensitive Protein Detection via Single Molecule Arrays Towards Early Stage Cancer Monitoring*. 2015. **5**: p. 11034.
214. Zeidan, E., et al., *Single-Multiplex Detection of Organ Injury Biomarkers using SPRi based Nano-Immunosensor*. 2016. **6**: p. 36348.
215. Panchuk-Voloshina, N., et al., *Alexa Dyes, a Series of New Fluorescent Dyes that Yield Exceptionally Bright, Photostable Conjugates*. *Journal of Histochemistry & Cytochemistry*, 1999. **47**(9): p. 1179-1188.
216. Zhang, W., et al., *Fully Automated 5-plex fluorescent Immunohistochemistry with Tyramide Signal Amplification and Same Species Antibodies*. *Lab Invest*, 2017. **97**(7): p. 873-885.

217. Riou, V., M. Périot, and I.C. Biegala, *Specificity Re-evaluation of Oligonucleotide Probes for the Detection of Marine Picoplankton by Tyramide Signal Amplification-Fluorescent In Situ Hybridization*. *Frontiers in Microbiology*, 2017. **8**(854).
218. Buchegger, P. and C. Preininger, *Four Assay Designs and On-Chip Calibration: Gadgets for a Sepsis Protein Array*. *Analytical Chemistry*, 2014. **86**(6): p. 3174-3180.
219. Gee, K.R., E.A. Archer, and H.C. Kang, *4-Sulfotetrafluorophenyl (STP) Esters: New Water-Soluble Amine-Reactive Reagents for Labeling Biomolecules*. *Tetrahedron Letters*, 1999. **40**(8): p. 1471-1474.
220. Kim, J., et al., *Noninvasive Alcohol Monitoring Using a Wearable Tattoo-Based Iontophoretic-Biosensing System*. *ACS Sensors*, 2016. **1**(8): p. 1011-1019.
221. Kotanen, C.N., et al., *Implantable Enzyme Amperometric Biosensors*. *Biosensors and Bioelectronics*, 2012. **35**(1): p. 14-26.
222. Faxälv, L., et al., *Blood Compatibility of Photografted Hydrogel Coatings*. *Acta Biomaterialia*, 2010. **6**(7): p. 2599-2608.

List of tables

Table 1. List of commonly applied BRE immobilization principles. Summarized from [74]	11
Table 2. Summary of calculated refractive indices (n_h and n_{h-dry}) and thicknesses (d_h , d_{h-dry} and d_{mIG}) of prepared hydrogel films, in dry, swollen and ligand immobilized states, for representative samples. Immobilized ligand concentration, Γ_{ligand} , determined from surface mass densities.	95

List of figures

Figure 1. Schematic depiction of biosensor components.....	2
Figure 2. Left. Dispersion relation of SPP in the Kretschmann configuration. Center. The Kretschmann and Right. Otto configurations of prism coupling to SPP. Figure adapted from [55].....	4
Figure 3. Angular reflectivity spectra and resulting shift in the SPR angle due to refractive index n_d increase at the surface.....	5
Figure 4. Top. Jablonski diagram that depicts the fluorophore electronic and excitation states. Bottom. Alexa Fluor 647 excitation and emission spectra. Image adapted from [57] and [58].....	6
Figure 5. Distance dependent electric field intensity distribution on thin gold film (50 nm) in the direction normal to the surface into a water dielectric at critical angle ($\theta = 48$ deg) and resonant angle ($\theta = 57$ deg). Calculated for Kretschmann configuration at $\lambda = 633$ nm with optical constants taken from literature [62]. Image adapted from [63]	7
Figure 6. An angular reflectivity and fluorescence spectrum of SPFS measurement showing the reflectivity and fluorescence intensity changes around the critical angle (bulk) and resonance angle (surface).	8
Figure 7. Angular field intensity enhancement spectra for different thicknesses of gold thin layer. The dielectric is water ($n = 1.33$) and incident light has $\lambda = 700$ nm. Image from [71].....	9
Figure 8. Idealized depiction of a mixed self-assembled monolayer (SAM) formed at a gold surface with functional coupling group for BRE immobilization and inert spacers for surface passivation.	10
Figure 9. Depiction of 3D swelling of bulk hydrogels and 1D swelling of surface attached hydrogel films. A. 3D hydrogel, B. microgel, C. polymer brushes and D. surface attached hydrogel film. Image from [75]	12
Figure 10. A. Graphical representation of the structural units and B. crystal structure of IgG molecule. Image from [93].	14
Figure 11. General scheme of a SELEX process. Image from [119].....	16
Figure 12. Left. A. Schematic depiction of the surface attached hydrogel sensor architecture for hydrogel optical waveguide spectroscopy and B. the corresponding angular reflectivity spectrum showing the TM modes.	28
Figure 13. Schematic representation of the optical instrumentation setup applied for SPR, HOWS and fluorescence measurements performed throughout the thesis.	29
Figure 14. Direct immobilization of thiolated aptamer sequences onto gold sensor chips and thiolated PEG molecules for surface passivation.	30
Figure 15: The principle of fluorescence assay that utilizes horseradish peroxidase label and fluorophore-tyramide conjugates for the label-mediated fluorophore attachment on proteins within hydrogel binding matrix in contrast to pre-labeled detection antibody.	91
Figure 16. Evaluation of non-specific adsorption of differently charged fluorophore (Left. AF647 -2 and Right. Cy5 +1) tyramide conjugates in ligand immobilized hydrogel matrix. Non-specific adsorption of Tyr-AF647 (Right) to sensor surface is lower compared to and Cy5 (Left) as depicted by the green line. 97	
Figure 17. Comparison of buffers PBS and PBST on reducing non-specific adsorption of Tyr-AF647. Fluorescence signal intensity at waveguide mode ($\theta \approx 47.8$ - 47.9) and critical angle ($\theta \approx 47.0$ - 47.3) lower for PBST (difference of grey and blue lines) compared to PBS (difference of black and red lines) buffer	

suggests less non-specific adsorption. Low F at critical angle indicates low adsorption of fluorophores to flow-cell walls rather than on the sensor surface..... 98

Figure 18. Role of ligand mIgG on Tyr-AF647 adsorption evaluated by comparing unmodified (black and red lines) and mIgG immobilized (green and blue lines) hydrogel matrices. 99

Figure 19. HRP enzyme activity saturation observed by increasing reaction duration (Left) as well as repeated exposure to Tyr-AF647 (Right). $t_1= 15$ minutes, $t_2= 30$ minutes, $C_{g-\alpha mIgG-HRP}= 125$ pM..... 100

Figure 20. Left. Calibration curve of ΔF from AF647-labeled detection antibody and HRP-antibody generated Tyr-AF647 labelling, and the ratio of the values expressed as signal amplification. Right. Determined LOD of the different assay schemes. 101

Abbreviations

AF647	alexa fluor 647
AFB ₁	aflatoxin B ₁
AFM	atomic forcemicroscopy
AgNP	silver nanoparticle
ATP	adenosine triphosphate
ATR	attenuated total internal reflection
AuCNT	gold carbon nanotube
AuNBP	gold nanobiopyramid
AuNP	gold nanoparticle
AuNR	gold nanorod
BP	benzophenone
BRE	biological recognition element
BSA	bovine serum albumin
CNT	carbon nanotube
cps	counts per second
DLS	dynamic light scattering
DMSO	dimethylsulfoxide
DNA	deoxynucleic acid
DNase	deoxyribonuclease
EDC	1-ethyl-3-(3-dimethylaminopropyl)carbodiimide
FCS	fluorescence correlation spectroscopy
FISH	fluorescence in-situ hybridization
FR	folate receptor
FRET	fluorescence resonance energy transfer (also RET)
GO	graphene oxide
GQD	graphene quantum dot
HA	haemagglutinin
HEPES	4-(2-Hydroxyethyl)piperazine-1-ethanesulfonic acid
HOW-FS	hydrogel optical waveguide fluorescence spectroscopy
HOWS	hydrogel optical waveguide spectroscopy
HRP	horse-radish peroxidase
IgG	immunoglobulin G
IHC	immunohistochemistry
IL-6	interleukin 6
IR	infrared
LOD	limit of detection
LRSP	long-range surface plasmon
LSP	localized surface plasmon
MB	molecular beacon
MEF	metal-enhanced fluorescence
MGO	magnetic oxidation graphene
NIR	near-infrared
NTA	nitritotriacetic acid
OSTE	off-stoichiometry thiol-enes
PBS/PBST	phosphate buffer saline/ tween

PDMS	polydimethylsiloxane
PEF	surface plasmon field-enhanced fluorescence or plasmon enhanced fluorescence
PEG	polyethylene glycol
pNIPAAm	poly-N-isopropylacrylamide
PPi	pyrophosphate
PS	polystyrene
PSA	prostate specific antigen
QD	quantum dot
RCA	rolling circle amplification
RET	resonance energy transfer (also FRET)
RI	refractive index
RNA	ribonucleic acid
SAM	self-assembled monolayer
SELEX	systematic evolution of ligands by exponential enrichment
SP	surface plasmon
SPCE	surface plasmon coupled emission
SPFS	surface plasmon field-enhanced fluorescence spectroscopy
SPP	surface plasmon polariton or propagating surface plasmon
SPR	surface plasmon resonance
TCEP	tris(2-carboxyethyl)phosphine hydrochloride
TCP	meso-tetra(4-carboxyphenyl)porphyrin
TDM	therapeutic drug monitoring
TE	transverse electric
TFPS	sodium para-tetrafluorophenolsulfonate
TM	transverse magnetic
TSA	tyramide signal amplification

CURRICULUM VITAE

Surname Sergelen
Given Name Khulan
Date of Birth: July 27, 1986
Nationality: Mongolian
Email: khulan.sergelen.fl@ait.ac.at
hulanser@gmail.com



Education

October 2012-now (August 2017)

PhD, IGS Nanobiotechnology, Department of Nanobiotechnology, University of Applied Life Science (BOKU), Vienna, Austria and

Centre for Biomimetic Sensor Science, Material Science and Engineering Department, Nanyang Technological University, Singapore, Singapore

Thesis: Reversible plasmonic biosensors based on aptamers and hydrogels

October 2009- July 2012

MSc, Molecular Medicine, Master of Science in Molecular Biology, University of Vienna, Vienna, Austria

Thesis: "Evaluation of protein microarray technology for tumor autoantibody screening in colon cancer"

September 1, 2003 - June 8, 2007

BSc in Genetics and Molecular Biology, National University of Mongolia, Mongolia

Thesis: "Preparing and studying the activity of FMDV 3ABC antigen and its positive serum"

September 2005- July 2006: Exchange year at Department of Biochemical Science and Technology, National Taiwan University, Taipei, Taiwan

Research and professional experience

October 2013-October 2014: Visiting PhD student, "Colloidal gold nanoparticles for small molecule detection", Centre for Biomimetic Sensor Science, Material Science and Engineering Department, Nanyang Technological University, Singapore, Singapore

October 2012-now: PhD student, "Reversible plasmonic biosensors based on aptamers and hydrogels"

BioSensor Technologies, Austrian Institute of Technology, Vienna, Austria

May 2011-July 2012 : Master's student "Protein-chip-technology for improving Colon and Prostate Cancer diagnostic testing", Health and Environment Department, Austrian Institute of Technology, Vienna, Austria

March-December 2010: Research student "Molecular analysis of mba gene ON/OFF switch in Ureaplasma parvum", IBMH, University of Veterinary Medicine, Vienna, Austria

July 2007-April 2009: Clinical molecular biology and microbiology laboratory analyst, "Gyals" Medical Center, Ulaanbaatar, Mongolia

Certificates and trainings

Dec 2008: Molecular Biology diagnostic methods, Bioneer, South Korea

Sep 2008: Lecturer, "Current Advances in Laboratory Diagnostics Workshop", Ulaanbaatar, Mongolia

Nov-Dec 2007: Bacteriology Samples to result, Automated methods for ID and AST testing, BioMerieux, France

Language Proficiency

Mongolian (Native), English (Native-level), German (Intermediate- B1).

Publications

- **K.Sergelen**, C.Petri, U.Jonas, W.Knoll, J.Dostálek, J.Dostálek. free-standing hydrogel membrane with dynamically controlled permeability for lab-on-chip applications, *Biointerphases*, submitted.
- **K.Sergelen**, B.Liedberg, W.Knoll, J.Dostálek. Surface plasmon field-enhanced fluorescence reversible split aptamer biosensor, *Analyst*, 2017, in press
- **K.Sergelen**, S.Fossati, A.Turupcu, C.Oostenbrink, B.Liedberg, W.Knoll, and J.Dostálek, Plasmon field-enhanced fluorescence energy transfer for hairpin aptamer assay readout, *ACS Sensors*, 2017, 2 (7), pp 916–923.
- A.Vagias, **K. Sergelen**, K.Koynov, P.Košovan, J. Dostálek, U.Jonas, W.Knoll, G.Fytas. Diffusion and permeation of labeled IgG in grafted hydrogels, *Macromolecules*, 2017, 50 (12), pp 4770–4779.
- J.A.Luna-Coronell, **K.Sergelen**, I.Gyurján, A.Weinhäusel. The immunome of colon cancer: Functional In silico analysis of proteins deduced from IgG microarray profiling, *Genomics, Proteomics & Bioinformatics*, submitted
- Q. Zhang, Y. Wang, A., Mateescu, **K. Sergelen**, A. Kibrom, U. Jonas, T. Wei, J. Dostálek. Biosensor Based on Hydrogel Optical Waveguide Spectroscopy for the Detection of 17 β -Estradiol, *Talanta*, (2013), 104, 149-154
- P.Syed, J.A.Luna-Coronell, **K.Sergelen**, I.Gyurján, A.Weinhäusel. The current status of cancer biomarker research using tumour-associated antigens for minimal invasive and early cancer diagnostics. *Journal of Proteomics*. 07/2012; 76
- P.Syed, K.Vierlinger, A.Kriegner, **K.Sergelen**, J.Luna-Coronell, C.Rappaport-Fürhauser, C.Nöhammer, C.F.Singer, A.Weinhäusel. Evaluation of auto-antibody serum biomarkers for breast cancer screening and in silico analysis of sero-reactive proteins. *Journal of Molecular Biochemistry*. 2012: 1(2).